2016

Fabrication of Electrospun TiO2/Polymer Composite Nanofibers For Photocatalysis and Degradation of Toxins

Danielle L. Mccarthy
Binghamton University--SUNY, dmccart5@binghamton.edu

Recommended Citation

Mccarthy, Danielle L., "Fabrication of Electrospun TiO2/Polymer Composite Nanofibers For Photocatalysis and Degradation of Toxins" (2016). *Graduate Dissertations and Theses*. 15.
https://orb.binghamton.edu/dissertation_and_theses/15

FABRICATION OF ELECTROSPUN TiO_2/POLYMER COMPOSITE NANOFIBERS FOR PHOTOCATALYSIS AND DEGRADATION OF TOXINS

BY

DANIELLE L. MCCARTHY

BS, State University of New York at Cortland, 2011

DISSERTATION

Submitted in partial fulfillment of the requirements for
the Degree of Doctor of Philosophy in Chemistry
in the Graduate School of
Binghamton University
State University of New York
2016

Accepted in partial fulfillment of the requirements for
the Degree of Doctor of Philosophy in Chemistry
in the Graduate School of
Binghamton University
State University of New York
2016

April 13, 2016

Professor Alistair J. Lees
Chair, Department of Chemistry, Binghamton University

Professor Wayne E. Jones, Jr.
Faculty Advisor, Department of Chemistry, Binghamton University

Professor Chuan-Jian Zhong
Member, Department of Chemistry, Binghamton University

Professor Gerard S. McGrady
Member, Department of Chemistry, Binghamton University

Professor Bruce White
Outside Examiner, Department of Physics, Binghamton University

Accepted in partial fulfillment of the requirements for
the Degree of Doctor of Philosophy in Chemistry
in the Graduate School of
Binghamton University
State University of New York
2016

April 13, 2016

Professor Alistair J. Lees____
Chair, Department of Chemistry, Binghamton University

Professor Wayne E. Jones, Jr. ____
Faculty Advisor, Department of Chemistry, Binghamton University

Professor Chuan-Jian Zhong____
Member, Department of Chemistry, Binghamton University

Professor Gerard S. McGrady____
Member, Department of Chemistry, Binghamton University

Professor Bruce White____
Outside Examiner, Department of Physics, Binghamton University

Abstract

Our society has made significant advancements in technology as it continues to grow in size which in turn has led to an accumulating amount of toxic threats. Some types of harmful pollution our society is currently facing include industrial waste such as organic dyes, pharmaceutical pollution and chemical warfare agents (CWAs). To date the nerve agent, *O*-ethyl *S*-[2-(diisopropylamino)ethyl] methylphosphonothioate), also known as VX, is the world's most lethal chemical substance. Some of these deadly nerve agents have been employed in various conflict and terrorist attacks. Currently available CWA degradation techniques include incineration and water hydrolysis followed by biotreatment with enzymes. Drawbacks to these techniques include the selectivity of the analyte, degradation of the enzyme over extended treatment time, and lack of robustness for practical applications. A more effective approach may be achieved by heterogeneous catalysis employing nanostructured materials. Solid catalysts including titania have demonstrated a means to effectively destroy CWAs.

TiO_2 is regarded as an efficient photocatalyst for degradation of organic toxins due to its strong oxidative power, high stability, low cost, and environmental friendliness. TiO_2 nanofibers represent an alternative materials approach to conventional nanoparticle composites for use in photocatalytic degradation. Nanofibers were fabricated using a sol gel synthesis and electrospinning; a non-mechanical, electrostatic process using electrically driven jets producing fiberous matt that is followed by a thermal treatment resulting in TiO_2. Further modification of TiO_2 with metal nanoparticles introduces the

area of study known as plasmonics. Materials possess unique optical characteristics that can further enhance the destruction of toxic threats.

The synthesized fibers were used directly in photocatalytic degradations of 2-chloro ethyl ethylsulfide (CEES) and dimethyl methylphosphonate (DMMP) and were found to exhibit enhanced rates of degradation. It was seen that saturation of the TiO_2 nanofibers with water prior to exposure with CEES showed an overall increased the degradation under UV irradiation. Photocatalytic degradations of DMMP were designed to demonstrate the role of surface area in the degradation process. The comparison of nanofibers vs. nanoparticles supports a conclusion that surface area is not a critical factor in the degradation of target species.

Electrospun nanofibers of polymethyl methacrylate (PMMA) and titanium triisopropoxide (TTiP) were found to possess catalytic properties when introduced to methyl paraoxon, a simulated chemical warfare agent (SCWA). In addition to the photocatalytic advantages of these fibers, increased flexibility and durability were observed compared to electrospun TiO_2 nanofibers. The resulting fibers would also be better compatible with low temperature processing of multifunctional materials including metal-organic frameworks (MOFs) and sensors. It is shown that the presence of TTiP within the polymer/MOF composite increased percent conversion and lowered the half-life of the reaction. Results acquired are the best to date according to literature. It has been hypothesized there are multiple competing degradation mechanisms that are dependent on the source of irradiation used to drive the degradation reaction.

Plasmonics have inspired a significant amount of interest in various research communities for applications in nanophotonics, optics, catalysis, and energy conversion.

Materials possessing surface plasmon resonances (SPR), such as silver nanoparticles, have been studied and are known to exhibit appealing optical characteristics. Ag nanoparticles were deposited on the surface of the TiO_2 fiber through a polyol synthesis with silver nitrate. The hypothesis is the emission lifetime of Ag-TiO_2 will have a smaller intensity then that of TiO_2, this in turn would mean the recombination rate of electron hole pair in Ag-TiO_2 is slower than that of TiO_2. Degradations of methyl paraoxon with TiO_2 and Ag-TiO_2 did show that the metal deposited TiO_2 had an enhancement in the percent conversion to the nitrophenoxide product of methyl paraoxon.

In this work, it is shown there are many factors involved in optimizing the photocatalytic performance of TiO_2/ polymer composite nanofibers. The combination of novel nanotechnology with advancements in photocatalysis will provide new benefits and improvements with filtration, and self-decontaminating textiles and paints. The diversity of applications these materials can be incorporated in has the ability to be life changing for civilians and warfighters who are in constant threat of toxic agents. As research in this field continues to progress, degradation rates will only continue to increase in attempts to achieve airborne decontamination on a time-scale of milliseconds and liquid decontamination in seconds.

To my mother and father

Acknowledgments

I would first like to start by thanking my advisor, Professor Wayne E. Jones, Jr. for his endless amount of support, encouragement and, guidance throughout my graduate career. Dr. Jones saw my potential as a research student and believed in me from day one. He knew the successful and confident person I would grow to become before I did. I am forever thankful to Dr. Jones for helping guide me in becoming the person I always dreamt of being. As a Jones group member I was given many wonderful opportunities including attending the American Chemical Society National Conference five times and becoming the primary graduate student on a DoD grant that led to my decision to follow a career path in government research. Dr. Jones has been more than an just an advisor he has been a father figure, never sugar coating things I needed to hear as well as endless amounts of support and encouragement through this tough journey. He has been an incredible mentor and it has been such a privilege to be a part of the Jones research group. I truly aspire to be just like him.

I would also like to thank Dr. William E. Bernier for his guidance and endless amount of support. I truly appreciated the daily pep talks we had. Dr. Bernier brought a background of industry and business to our research group, providing knowledge we would not have known. He has always been there for me, as someone else to celebrate in my successes when I had a good day in the lab, to my sounding board when I would come up with ten crazy different ideas, to a voice of reason for those hard days. I am very grateful to have had him right there the last 5 years and am exceptionally grateful for all his help with my dissertation. Additionally, I would like to thank Dr. Brendan Flynn who was also an incredible help during the writing process and a source of guidance and encouragement throughout my graduate career.

I would like to thank my committee members: Dr. Alistair Lees, Dr. Chuan-Jian Zhong, Dr. Gerard S. McGrady and, Dr. Bruce White for aiding in corrections to my dissertation, support and encouragement through graduate school.

I would like to thank the entire Jones research group but especially my research partner and one of my dearest friends Dr. Jian Liu. We started this journey together five years ago and it is incredible that it has finally come to an end. I am forever grateful for his endless support and encouragement. I wish Dr. Liu only the best in his future endeavors. I would also like to thank Dr. Megan Fegley for being an incredible mentor and friend. I owe a lot of my success to her as she set the perfect example of a hard working graduate student as well as a successful professional, an amazing wife and now a soon-to-be mom. She continues to be a person I aspire to be every day as I move forward into my professional career and begin a family. I would also like to thank Steven Boyer for all his help. I am forever grateful for his help in acquiring last minute data for my thesis, helping with the review process and being my sounding board when I just needed to talk without a second thought. I am looking forward to hearing about the great things ahead for him. I would like to thank Dr. Kenneth Skorenko who has been an incredible friend and colleague the last five years. I am appreciative of all the advice, talks and guidance he has provided. I would also like to thank Lynn Schmitt who is one of the best friends I could ever ask for. From our deep discussions about chemistry to wine and game night you have been an incredible friend and such an amazing person. I furthermore would like to thank all of the Jones group members past and present whom I have had the privilege of working with. I hope to continue to work with everyone again in the future and wish everyone the best of luck.

I would like to thank my undergraduate students whom I have had the pleasure of working with throughout my career as a graduate student. Amelia Greene was my very first undergraduate student; little did I know she would become such an amazing friend. She exudes self-confidence and determination and I am so proud of the woman she has become. Julia Tollin was my second undergraduate student who helped me acquire the majority of my data for my chapter 2 as well as aided in the methodology development for the degradation experiments with simulated chemical warfare agents. I was able to work with Julia for two years and watch her not only grow as a chemist but as a person as well. I am so incredibly proud of her as she is now a medical student at Upstate Medical in Syracuse. Finally I would like to thank Jennifer Troiano whom without her I would be lost. She is such an incredibly bright and driven student whose opportunities are endless. I cannot thank her enough for all her help acquiring data, being a sounding board and most importantly being a good friend. Without my undergraduate students this thesis would have not been possible. Thank you all so much, I appreciate it more then you will ever know.

I would like to thank all the organizations responsible for my funding during my graduate study, including the Binghamton University Chemistry Department, the Binghamton University Graduate School, the Clifford D. Clark Diversity Fellowship, the Research Foundation and, the Army Research Office. Without their funding my Ph.D would not have been possible. I would further like to extend my gratitude to the hardworking people within these organizations who played a pivotal role in my life including, Pat Gorman, Lynn Hickey, Connie Dowling, Renee Sersen, Dr. Jared DeCoste and Greg Peterson.

It was in elementary school when I knew I was going to become a scientist someday. I have to thank Mrs. Deluca my 2nd grade teacher at Harry L. Elementary School in Johnson City New York for being by far the most influential person in my life. Her love of science was infectious and had an everlasting impact on me at seven years old. Her passion lied in astronomy and there is not a night that doesn't go by that I don't look up at the stars and smile. She is truly an incredible scientist and person and I hope one day I can have as positive of an impact on someone, as she did on me. I am forever grateful!

I would like to thank my family for their endless love and support throughout my entire life. My parents were always there for me through all of the difficult and stressful times I dealt with as a graduate student. My parents are incredibly hard workers who made many sacrifices to make sure my sister and I had the best childhood possible. I cannot put into words how grateful and appreciative I am to have the most amazing mother and father in the world.

Finally, I would like to thank my soon-to-be husband Tyler Kuhn. He is truly everything I could ask for and more as a partner. Thank you for the endless amount of support, being my rock, my cheerleader and the voice of reason. Tyler spent endless nights in the lab as well just so I wouldn't have to sit here alone. I am so grateful to have been blessed with the most amazing person to spend my life with. I love you forever and always.

Table of Contents

List of Tables

List of Figures

Chapter 1

Chapter 2

Chapter 3

Chapter 4

List of Commonly Used Symbols and Abbreviations

TiO_2	Titanium Dioxide
XRD	X-ray Diffraction
Ɵ	X-ray Diffraction Angle
λ	Wavelength
MLCT	Metal-to-ligand Charge Transfer
PMMA	Poly(methyl methacrylate)
TTiP	Titanium Isopropoxide
DMF	N, N – dimethylformamide
MOF	Metal-Organic Framework
SEM	Scanning Electron Microscopy
EDX	Energy Dispersive X-ray Spectroscopy
EG	Ethylene Glycol
PL	Photoluminescence
wt%	Weight Fraction
BET	Brunauer-Emmett-Teller
TEM	Transmission Electron Microscopy
cm	Centimeter
cm^{-1}	Wavenumber
nm	Nanometer

LUMO	Lowest Unoccupied Molecular Orbital
FTIR	Fourier Transform Infrared Spectroscopy
T	Temperature
t	Time
k	Rate Constant
NF	Nanofiber
NP	Nanoparticle
μL	Mircoliter
mL	Milliliter
ATR	Attenuated Total Reflectance
CEES	2-Chloroethyl ethyl sulfide
DMMP	Dimethyl methylphosphonate
HD	Sulfur Mustard
GD	Soman
GB	Sarin
GA	Tabun
VX	O-ethyl S-[2(diisopropylamino)ethyl] methyl Phosphonothioate
·	Radical
eV	Electron Volts
CB	Conduction Band
VB	Valence Band
ζ	Photonic Efficiency

fs	Femtosecond
SPR	Surface Plasmon Resonance
Ag	Silver
P25	Titanium Dioxide Nanoparticles
°	Degree
UV	Ultra Violet
Vis	Visible
UV-Vis	Ultra-Violet Visible Spectroscopy
NMR	Nuclear Magnetic Resonance
CWA	Chemical Warfare Agent
SCWA	Simulated Chemical Warfare Agent
NH_2	Amine
h	Hour

CHAPTER 1: Introduction to Heterogeneous Photocatalysis

1.1 Toxic Threats and Photocatalysis

Remediation of toxic threats continues to be the focus of research with new advancements in science that improve on the degradation of organic pollutants. Some types of harmful pollution our society is currently facing include but are not limited to industrial waste such as organic dyes, pharmaceutical pollution and chemical warfare agents. The challenge is to degrade these harmful compounds in a way that produces nontoxic products that pose no threat to humans or the environment. The goal of our work has been to achieve this by complete hydrolysis into non-hazardous compounds using heterogeneous catalysts including photocatalysts.

1.1.1 Environmental Pollution

Pollution continues to be a topic of interest in the research community as our society grows in size and advances in technology. There are numerous products of non-renewable energy sources and industrial processes causing a vast amount of pollution. Industrial waste and pharmaceutical waste have been known to accumulate in waste and ground water, resulting in chronic and aesthetic pollution to the surrounding environment.[1] Pharmaceutical waste is not solely acquired from biomedical companies but research laboratories, health clinics, hospitals and home use. In a Chemical & Engineering News (vol 93, iss 31) article covering pharmaceutical pollution it was stated that approximately 25% of the world's rivers and lakes are contaminated with pharmaceuticals at varying concentrations ranging from nanograms to micrograms per liter.

Pesticides are a toxic threat worldwide and continue to jeopardize our environmental sustainability. In a U.S Geological survey it was determined that 99% of all major urban streams in the United States were contaminated with at least one pesticide and of those, 70% were affected by 5 or more pesticides.[2] There are six major classes of pesticides that include, metallic and organo-metallic pesticides, organochlorines, organophosphates, carbamates, and pyrethroids.[3] Organophosphates have been used since 1937 but grew in usage when organochlorine compounds were banned in the 1970's and 1980's.[4] There are many incidents on record of organophosphate poisoning causing many neurological and immunotoxcity related symptoms. The fate of organophosphates in the environment is affected by transport as well as chemical and biological processes.[5] Literature has mainly focused on the persistence and rate or sorption in contaminated soils and degradation by using sediments. [6] Current research needs to move toward degradation of the organophosphates in both solid and liquid media into less toxic and non-harmful byproducts.

1.1.2 Chemical Warfare Agents: Background

The use of chemical warfare agents (CWA's) are designed toxins that can persist and represent another significant challenge to the modern world. CWA's are not new to human kind but began centuries ago in early Greek and Roman times. The first documented use of chemical warfare was during World War I in Ypres, Belgium where chlorine gas was used by the Germans.[7] This led Germany's industrialization and major production of blistering agents also known as vesicants, in particular sulfur mustard (HD). It was not until the 1930s that highly toxic organophosphates were discovered by the Germans while studying pesticides. The G-Agents are nerve agents that are non-persistent and include, Tabun (GA), Sarin (GB) and Soman (GD).

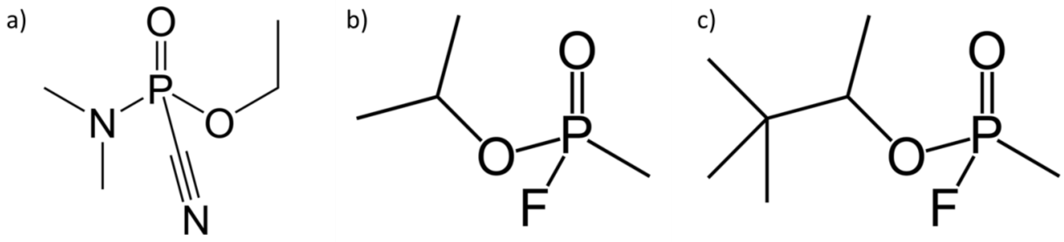

Figure 1-6 Molecular structures of a) Tabun, GA b) Sarin , GB and c) Soman, GD

Nerve agents are found to interrupt the breakdown of acetlychlolinesterease by binding with acetylcholine enzymes, resulting in asphyxiation and death.[8] It was not until after WWI that G-series nerve agents were mass produced. In the early 1950 V-type nerve agents were discovered in the United Kingdom. To date, *O*-ethyl *S*-[2-(diisopropylamino)ethyl] methylphosphonothioate) also known as VX is the world's most lethal chemical substance. Unfortunately it is known that some of these deadly nerve agents have been employed in various conflict and terrorist attacks. Some of these events include Iraq and Iran in the 1980s, the use of Sarin in 1995 in Tokyo and, more recently, the United Nations believes Sarin was used in an attack against Syrian civilians in 2015.[9]

Destruction of these chemical warfare agents (CWAs) is imperative as stockpiles of these chemicals have grown to a large amount as well as environmental intervention post attack. Currently available CWA degradation techniques include incineration, water hydrolysis followed by biotreatment and water hydrolysis followed by supercritical water oxidation.[10,11] Drawbacks to these techniques include the selectivity of the analyte, degradation of the enzyme over extended treatment time and lack of robustness for practical applications.

1.2 Introduction to TiO_2 as a Photocatalyst

1.2.1 General Introduction

TiO_2 represents a relatively new approach to toxin degradation and removal. It has become widely utilized in commercial items used on a daily basis, including sunscreen, toothpaste, and even candy. In the early 1960s people began studying photo-induced phenomena in semiconductor solids. In 1972 titania (TiO_2) was found to possess photocatalytic properties, which has been referred to as the “Honda-Fujishima effect”.[12] It was not until the work of Frank and Brad in 1977 that TiO_2 was found to be useful for the photocatalytic oxidation of cyanide and sulfite in aqueous solution.[13] The interest and expansion of research into TiO_2 as a photocatalyst for the degradation and removal of organic toxins has grown markedly.

TiO_2 possesses three crystal structures: anatase, rutile and brookite. They are built through the connection of TiO_6 octahedra, as shown in **Figure 1-2** below. The brookite phase exhibits both corner- and edge- sharing configuration resulting in an orthorhomobic structure. Rutile also shares in the corner- and edge configurations, whereas anatase consists of solely edge sharing; however both result in a tetragonal structure.[14]

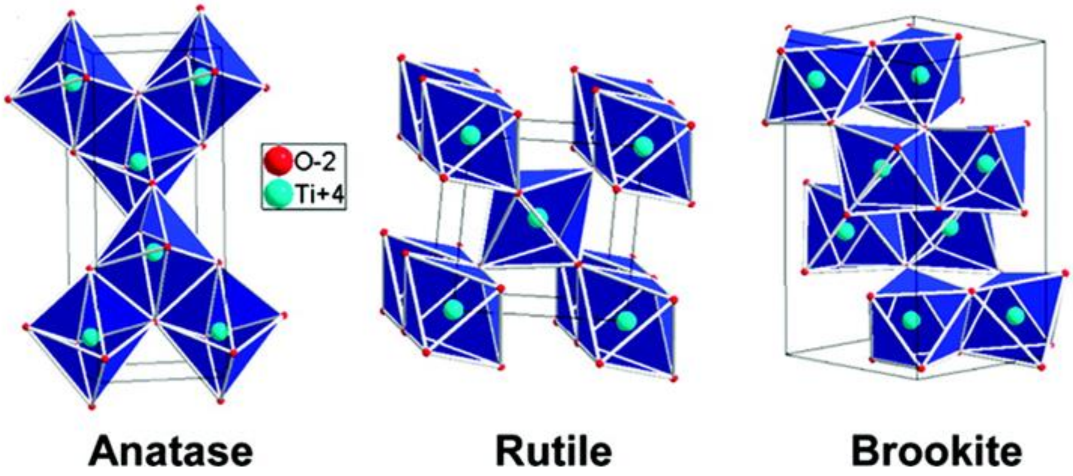

Figure 1-7 Crystalline structures of TiO_2 (Adapted from Dambournet, et. al. Chem. Mater. 2010, 22, 1173–1179 1173)

The anatase and rutile crystal phases of TiO_2 can easily be formed in an aqueous medium.[15] Brookite is much more challenging and there is little literature regarding the successful synthesis of pure brookite TiO_2. Two methods that have been useful in the formation of brookite include a thermolysis reaction[16] of $TiCl_4$ and the oxidation[17] of $TiCl_3$ with urea. Rutile is the most thermally stable of the three crystal structures as a macrostructure, but as the size of the particle decreases the anatase phase then becomes the most thermally stable.[18] The transition from anatase to rutile does not occur kinetically at room temperature. Physically, the conversion temperature and rate of transformation is dependent on how fast the primary particles in the anatase phase sinter together to reach a critical size. Both the anatase and rutile phases will grow in size as the temperature is increased until a critical size is reached for anatase, and will then remained unchanged whereas rutile particles will continue to grow as the temperature increases.

Determination of the crystal structure and the different phases requires the use of analytical instrumentation for accurate characterization. X-ray diffraction (XRD) is a technique widely used to analyze the crystal diffraction pattern. The grain size and rutile fraction can be calculated by the Scherrer equation.[19] By knowing the intensities of the characteristic peaks of the crystal phase the peak intensity can be substituted into the following equation.

$$Rutile\ wt\% = \frac{I_R \times 100}{I_R + (0.8) I_A} \text{………………………..………} (1)$$

I_R and I_A represent the linear intensities of the main peaks in anatase and rutile.[20,21] Anatase has representative peaks at $\Theta = 12.65°$, 18.9° and 24.1°, while the rutile phase has peaks at $\Theta = 13.75°$, 18.1° and 27.2° and the brookite peaks are at $\Theta = 12.65°$, 12.85°, 15.4°, 18.1°, where Θ represents the XRD angle.

There are a considerable number of structural forms and morphologies of titania that can be synthetically fabricated. The use of nanoparticles in photocatalytic degradation has been the conventional approach seen in the literature. It has been shown that nanoparticles with a small percentage of rutile phase crystal fraction show enhanced photocatalytic activity due to the efficient electron and hole separation between the rutile and anatase crystal phases. [22,23] TiO_2 nanofibers represent an alternative approach to conventional nanoparticle composites for use in photocatalytic degradation. The one-dimensional morphology of TiO_2 nanofibers is desired compared to spherical TiO_2 nanoparticles owing to excellent mobility of charge carriers, high surface area ensuring high dispersion, and the existence of pores.[24, 25] TiO_2 is very versatile, allowing for surface functionalization as well as enhancing the accessibility of electrodes to the hole-transporting materials, and hence enhanced charge collection and transport.[26]

1.2.2 Dark vs. Light Irradiation

Upon irradiation with the appropriate energy an electron is excited from the conduction band in TiO_2 an electron-hole pair is formed. This pair is created near the surface of the semiconductor due to the small UV penetration depth of ~160 nm.[27] Generally, the resulting holes can be trapped by a bridging O_2^- on the surface, or there is the possibly for the hole to migrate and bind with surface bound OH^- anions; this would result in radical species such as $\cdot O^-$ or $\cdot OH$. In the conduction band the excited electrons are forced to move from the surface into the bulk due to the band bending phenomenon, where the electron can be delocalized over different Ti ions. Subsequent studies have been performed showing that the photogenerated electron can also exist at the surface participation in formation of radical species.

In any bulk semiconductor the interface between the surface and a molecule will encounter many restrictions stemming from the charge transfer process; this phenomenon is better known as band bending.[28] Band bending is the difference in energy between the Fermi level of a semiconductor and the flat band potential occurring at the Schottky interface. TiO_2 is often found to have a large number of surface defects, resulting in oxygen vacancies. Diebold determined that these vacancies found in TiO_2 would act like donor states, resulting in an accumulation of electrons at the surface causing a downward band bend.[29]

All processes that occur at the surface of semiconductors are driven to achieve equilibrium between the potential of the Fermi level and the chemical potential of the adsorbates. [30] This work subsequently lead to the discovery made by Martinez *et. al* that depending upon the oxidation state at the surface and the redox potential of the adsorbate electrons can easily flow from one to another, producing negatively or positively charged species at the surface.[31]

1.2.3 Fabrication Methods

Different synthetic approaches can be taken to prepare materials with various shapes, crystal phases and porous structures such as fibers, particles, aerogels and rods. These methods include, but are not limited to, sol-gel synthesis as a means to form fibers, films and particles, direct oxidation in which the source of Ti comes from the oxidation of a metal plate, and other methods such as microwave or aerogels which combine the sol gel process with supercritical drying. Here we describe several preparation methods which are suitable for the production of TiO_2 and allow for tuneability in both chemical and physical properties.

1.2.3.1 Sol-Gel Method

The sol-gel method is commonly used as a synthetic technique to fabricate TiO_2. It is prepared through the formation of a colloidal suspension or a sol from the hydrolysis and polymerization reactions of the precursors.[32] In the case of titania, an inorganic metal salt or metal organic compounds is used in the synthetic process. The titanium precursor generally undergoes hydrolysis; acid catalyzed hydrolysis of titanium (IV) alkoxide followed by condensation is frequently seen in the literature.[33] The formation of the Ti-O-Ti bonds via hydrolysis is highly dependent on the amount of water exposure. In low water conditions close packing of three-dimensional polymeric skeletons will occur. However in higher water condition the formation of $Ti(OH)_4$ occurs. There are several other parameters that greatly affect the formation of TiO_2. It was found the morphology of the titania is highly dependent upon the pH, and even the most subtle pH changes can have a drastic effect on the morphology and shape of the nanoparticle.[34] Thermal treatments of the titania post hydrolysis have been found to affect the crystalline phase and size. Depending on the temperature and duration to which the titania is exposed one could obtain a mix of rutile and anatase phases as well as varying diameters.[35,36,24] Sols can be used in range of TiO_2 formations including, but limited to, thin film deposition, nanoparticles, nanorod and nanotube arrays as well as nanofiborous mats.

1.2.3.2 Direct Oxidation Method

Titania-based materials can be fabricated through the oxidation of titanium metal using oxidant or under anodization.[32] Crystalline TiO_2 nanorods have been synthesized by direct oxidation of a titanium metal plate using hydrogen peroxide.[37] The source of oxygen does play a pivotal role in this process, as there is a competition between the oxygen and the titanium. The rate of diffusion largely controls many physical and chemical properties including the surface morphology of the titania. It was found that at high temperatures acetone is a good source of oxygen in the preparation of TiO_2 nanorods during the oxidation of a Ti plate.[38]

1.2.3.3 Other Methods

There are many different synthetic approaches to fabricating TiO_2 in all different shapes, sizes and, morphologies. Two innovative ways to manufacture TiO_2 are in the form of aerogels and by microwaves. TiO_2 aerogels combine the sol-gel process with supercritical drying. This method has the advantages of acquiring desirable morphologies and chemical properties that are otherwise difficult to obtain by other more standard synthetic approaches. Campbell *et. al* were able to prepare TiO_2 by a sol gel synthesis using the Ti precursor titanium *n*-butoxide in methanol followed by a solvent removal using supercritical carbon dioxide.[39]

High-frequency electromagnetic waves are another method of producing dielectric materials, and have been documented to prepare a variety of TiO_2 materials. The frequencies that are commonly used in microwave heating are between 900 and 2450 MHz. At low frequencies the energy from the microwave field can transfer to the material due the movement within the ionic components. At higher frequencies the energy is primarily absorbed by the molecules that possess a permanent dipole. Under the electric field of the microwave these dipoles will tend to re-orientate. Titania colloidal nanoparticles have been prepared through this method on the timescale of 5 min to 1 h, compared to a more standard forced hydrolysis which on average can take up to 32 h.[40] Microwave fabrication of titania is very appealing not only because of faster preparation but it is also attractive to industrial processing.

1.3 TiO_2 Working Mechanism

Photocatalytic degradation can include a variety of reactions including organic synthesis, photoreduction, hydrogen transfer, water detoxification and gaseous pollutant removal.[41] For TiO_2 to be a working photocatalyst, energy from incident light is required. It is well know that electon-hole pairs are generated when TiO_2 is irradiated by UV photons with an energy that is greater than or equal to the band gap energy. The band gap energies of anatase, rutile and brookite vary from 3.20 through 3.03, to 3.10 eV, respectively.[42]

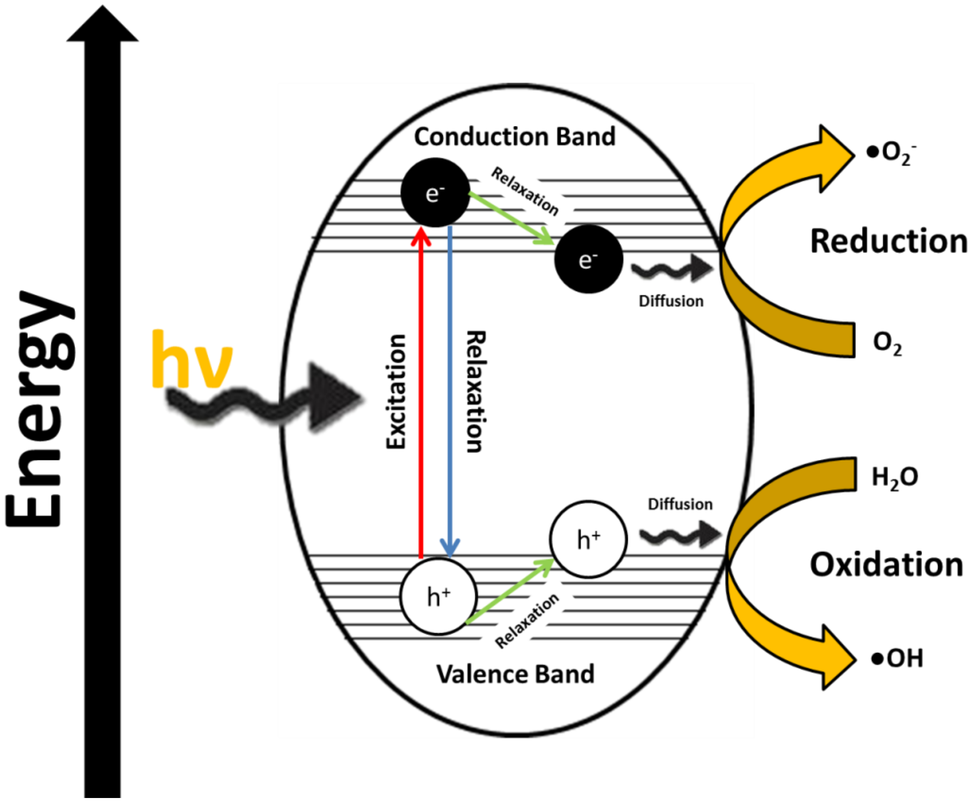

Figure 1-8 Charge transfer mechanism of TiO_2 when exposed to UV irradiation.

The electrons are excited from the valence band to the conduction band leaving behind a positive hole. These photoinduced charge carriers can then react with surface adsorbed species to form oxidizing and reducing species, as well as hydroxyl and super oxide radicals. Once formed, these photochemical products can degrade chemicals that are adsorbed on the surface of the TiO_2 or diffuse to the surface during the lifetime of the reactive intermediate. Only molecules that are in direct contact with the catalytic surface will undergo photocatalytic degradation.[43] Once in contact with the surface both oxidation and reduction will occur simultaneously. Recombination will occur unless there is a scavenger available to produce subsequent radicals that will successively degrade the targeted pollutant at the surface. This mechanism can be seen in **Figure 1-3**.

The majority of reports in the literature agree on the model of TiO_2 describing the mode of activation and the general degradation pathway. What is still being debated is whether the detailed mechanism includes the adsorption and desorption kinetics at the surface of the catalyst, as well as the diffusion to the surface of the catalyst. The quantum yield of the photocatalysis process was found to be difficult to calculate correctly due to the observation that TiO_2 is incapable of absorbing all of the incident irradiation due to refraction.[44,45] The efficiency of the photocatalytic process was found to be better calculated by evaluation the photonic efficiency, ζ, which is the rate of formation of the reaction product divided by the incident photon flow. Hoffman et. al. discovered that approximately 90% of photo-generated electron-hole pairs recombine rapidly after excitation, resulting in a ζ equal to 10%.[46] **Figure 1-4** provides an overview of the potential photo-induced processes both inside and on the surface of TiO_2.[28]

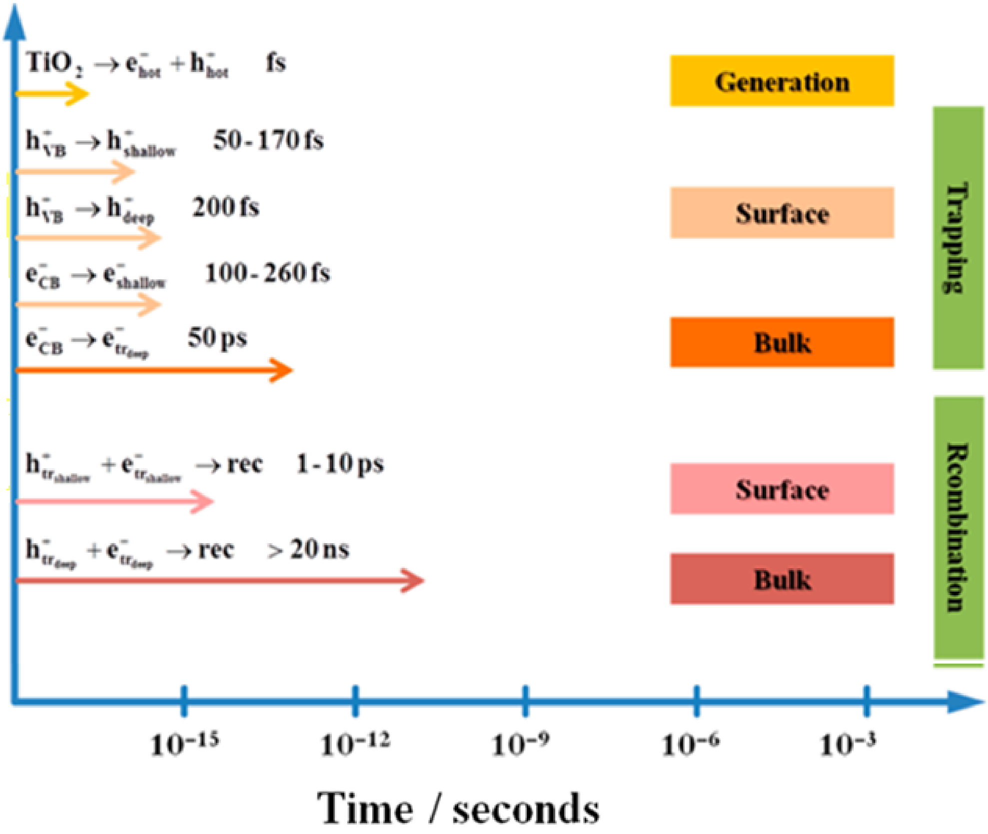

Figure 1-9. The sequence of photo-induced reactions in TiO_2 photocatalysis and the corresponding time scales are shown. (Adapted from Schneider *et. al.* Chem. Rev. 2014, 114, 9919-9986)

Time resolved absorption spectroscopy is a technique widely used to the study the formation, relaxation, recombination and transfer processes in charge carriers such as titanium dioxide. This technique acquires measurements on the femtoseconds (fs) scale allowing for a better interpretation of the kinetics at the surface or in the bulk of TiO_2. Work done by Skinner *et. al.* showed electron trapping occurred at 180±10 fs using ultrafast transient absorption data.[47] Subsequent work done by Serpone *et. al*. determined approximately 90% of photo-generated holes recombine within 10 ns which is consistent with the work done by Hoffmann.[48] The fast rates of recombination are due to shallow trapped charge carriers that arise from defects that occur on the surface of TiO_2. To reduce these defects a more efficient charge transfer process is necessary to allow for longer separation of the photo-generated electron-hole pairs.

1.4 Surface Modification of TiO_2

1.4.1 General Introduction

TiO_2 has been shown to be an acceptable catalyst for the degradation of organic pollutants via photocatalysis. However, limitations arise when looking to improve the overall efficiency. TiO_2 is limited to only use 5% of the total irradiation from natural sunlight to cause effective photosensitization. The limitations are due to the fact that thebwide band gap for bulk TiO_2 lies within the ultraviolet region of the solar spectrum, with band gap energies ranging from 3.0 eV for rutile and 3.2 eV for anatase as depicted in **Figure 1-5**.[49]

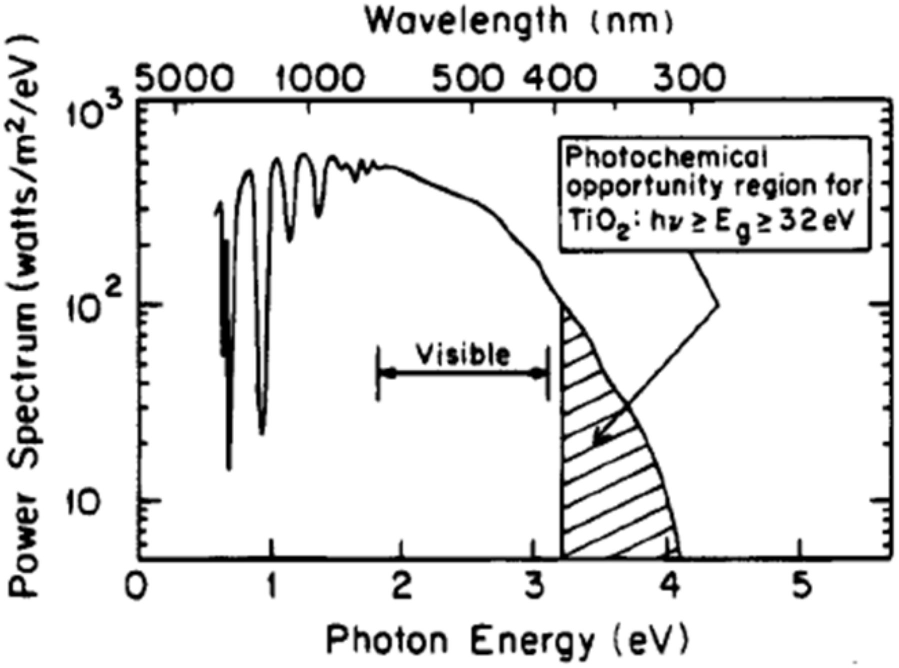

Figure 1-10. Solar spectrum at the surface of the Earth (Adapted from Linsebiger, A. L.; Lu, G.; Yates, J. T. Chem. Rev. 1995, 95, 735.)

Surface modification can be used to overcome many of the limiting factors identified for photocatalyts. This is possible through introduction of transition metals including but not limited to, Pt, Pd, Au and, Ag. Heterogeneous composites such as CdS, SiO_2 and Al_2O_3 also are used to create a change in the band gap energy level due to their smaller inherent band gaps which in turn play a significant role in the charge transfer process. Dye anchoring is another way to mediate these limiting factors by sensitizing the photocatalyst to improve on its optical properties, bringing the energy required for excitation into the visible region of the electromagnetic spectrum. The optical response of TiO_2 is also largely dependent on its electronic structure; by deliberately introducing non-metal dopants such as nitrogen such that the electronic structure will change while maintaining the crystal structure.

Figure 1-6. Potential routes to overcome the band gap and electron-hole pair limitations of TiO_2 for use as a visible light induced photocatalyst.

Surface adsorbates and hybrids with nanomaterials such as phosphates and metal-organic frameworks have been investigated as a means to mediate the limitations of TiO_2. Hybrid composites with nanomaterials can include carbon materials, such as graphene, graphite or fullerenes, which can be applied to enhance photocatalysis due to their unique advantages. Carbon possesses chemical inertness, and thermal stability as well as high electron conductivity. **Figure 1-6** covers some potential routes to resolve these limitations; some of these will be explored in the subsequent chapters.

1.4.2 Metal Organic Frameworks

Another approach to heterogeneous catalysis which could potentially be relevant to the removal and degradation of toxins is metal-organic frameworks (MOFs). The earliest reported demonstration by Hoskins and Robson in 1990 with their synthetic design of a new class of scaffolding like material $[N(CH3)_4][CuIZnII(CN)_4]$ and CuI[4,4',4'',4'''tetracyanotetraphenylmethane]$BF_4 \cdot XC_6H_5NO_2$,which is comprised of infinite polymeric chains.[50] Metal-organic frameworks have been compared to zeolites, and although they may not approach the same stability they do encompass some of the catalytically relevant features. The research continues to be promising as new MOFs are being fabricated. The thermal and water stability of these compounds that was once a primary concern has now since been solved.[51,52]

New research has been devoted to exploring the possibility of employing MOFs as platforms for the integration of different molecular components such as semiconductors, with the intention of achieving visible light induced catalysis for the improvement of various photocatalytic reactions. [53,54] There are numerous advantages, one example being the infinite amount of molecular combinations between the metal-oxo clusters and the bridging organic linkers. These allow for increasing selectivity and sensitivity towards targeted pollutants as well as tuning the capabilities for photocatalysis. [28] Recent work has included incorporating a Ti atom into MOFs and to functionalize the organic linker with amine groups as a way to drive visible light photocatalysis.[55,56]

1.4.3 Metal and Nonmetal Deposition

Doping an element into a semiconductor photocatalyst with a large band gap energy may allow for creation of an acceptor level in the forbidden band gap for visible induced photocatalysis.[57] TiO_2 is highly dependent on its electronic structure to perform photocatalytic reactions. By the introduction of a metal or non-metal ion to the chemical structure, the electronic configuration may be modified while the crystal structure of the semiconductor is maintained. Depending on careful selection of the modifier introduced, the band gap may be adjusted causing a shift in absorbance from the UV region of the electromagnetic spectrum into the visible, **Figure 1-7**.

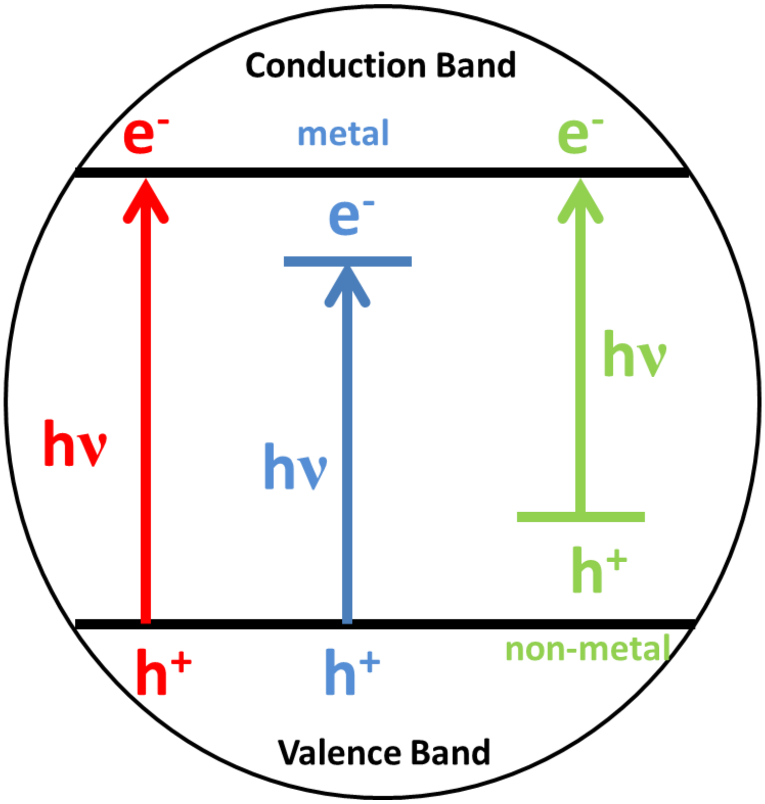

Figure 1-7. Mechanism for photo-generated electron-holes pairs; TiO_2(red) metal-doped TiO_2 (blue) and non-metal doped TiO_2 (green)

Metal- loaded TiO_2 can enhance the photo-generation of electron-hole pairs necessary for catalysis. This is done by describing the surface plasmon resonance (SPR) of the metal. The SPR will cause the local electromagnetic field to be increased upon irradiation. SPR is the resonant oscillation of electrons at the interface between a negative and positive material stimulated by incident light. Within the SPR, electrons are excited from energies that will exceed the band bending potential; charge carriers are created near the surface and then can easily reach the reactive sites of the semiconductor. The result is a separation between the oxidation reaction from the semiconductor and the reduction reaction from the metal. The interface between the metal and the semiconductor is better known as the Schottky barrier. In any bulk semiconductor the interface between the surface and a metal will encounter many restrictions stemming from the charge transfer process; this phenomenon is better known as band bending.[28],[58] Band bending is the difference between the Fermi level of a semiconductor and the flat band potential which is the amount of band bending occurring at the Schottky interface. TiO_2 is often found to have a large number of surface defects resulting in oxygen vacancies. Diebold determined that these vacancies found in TiO_2 would act like donor states, resulting in an accumulation of electrons at the surface causing a downward band bend.[29]

Some potential drawbacks to metal deposition on TiO_2 are: the potential electron trapping by metal centers, creation of electron-hole recombination centers, and thermal instability. Research is currently ongoing into minimizing these drawbacks. Different transition metals have been doped onto TiO_2 nanomaterials, such as Au[59], Pt[26], Pd[25], Ru[60], Ag, and Fe. Rare earth metals have also been found to be deposited on TiO_2 such as

La, Ce, Er, Pr, Gd, Nb and, Sm, which resulted in higher absorption and a red shift preventing electron-hole pair recombination by decreasing the band gap energy and bringing the energy required for photoexcitation into the visible region.[61]

Non-metal doping of TiO_2 was documented in 1986 by Sato et. al. where nitrogen doped TiO_2 (N-TiO_2) was fabricated from commercial titanium hydroxide by thermal treatment in static air.[62] The use of nitrogen doping as an enhancement to visible light absorption and photocatalytic activity what shown by Yates *et. al.* Yates showed the successful treatments of TiO_2 with nitrogen by using NH_3 gas and thermal treatment. When introduced to Rhodamine B, an organic dye, an enhancement in visible photodegradation was seen.[49] Fluorine doping has also become of interest but has yet to show any enhancement to photoreactivity in the visible region.[63]

1.4.4 Dye Sensitization

The use of organic dyes has been found to improve on the optical properties of TiO_2.[64] By sensitization with a dye, a fast electron transfer from visible light excited chromophores of the dye to the conduction band of the semiconductor can occur. This phenomenon is also known as metal to ligand charge transfer (MLCT). Common dyes used in sensitization are transition metal complexes incorporating such metal species as (Ru^{2+}, Zn^{2+}, Mg^{2+}, Fe^{2+}, and Al^{3+}).

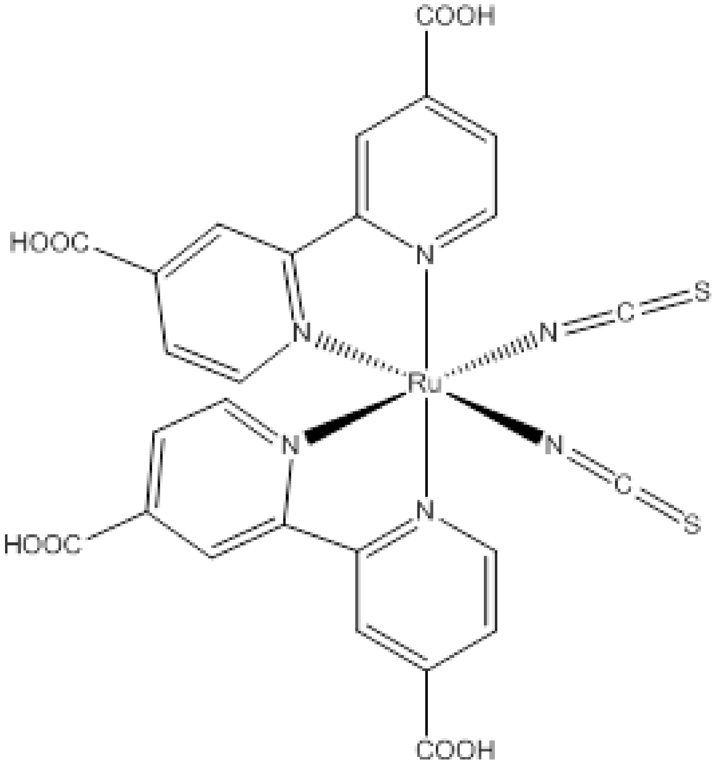

Figure 1-8. Molecular structure of N3: (cis-bis(iso-thiocyanato) bis(2,2-bipyridyl-4,4-dicarboxylato) ruthenium(II)

There are several different mechanisms through which the dye can be attached to the surface of the semiconductors. Some methods include covalent bonding, electrostatic interactions, hydrogen bonding and van der Waals forces. In the case of TiO_2 and the ruthenium-based dye shown in **Figure 1-8** the linkage occurs between the carboxyl group and the surface hydroxyls. The advantage to MLCT is the electron transfer process can persist and, therefore, electron hole recombination is not a concern as long as the dye possesses a lowest unoccupied molecular orbital (LUMO) excited state higher than the conduction band of the semiconductor. TiO_2 electrospun nanofibers that have been sensitized with N3 dye, also known as (cis-bis(iso-thiocyanato) bis(2,2-bipyridyl-4,4-dicarboxylato) ruthenium(II), and this has recently been documented in the visible light stimulated photodegradation of phenazopyridine, a biopharmaceutical.

1.5 Dissertation Overview

The Jones group has made considerable advances in the field of photocatalysis with its use of electrospun TiO_2 nanofibers. These fibers have been implemented in many different degradation reactions with a variety of target pollutants. Some of these pollutants include industrial organic dyes, biopharmaceuticals and most recently, simulated chemical warfare agents. This dissertation will expand on the research that has been performed by past group members, and work towards ways to functionalize and optimize the catalyst to further enhance the efficiency and rate of degradation.

Chapter 2 will demonstrate the fabrication of TiO_2 nanofibers from a sol-gel solution followed by electrospinning and finishing with a thermal treatment in atmospheric conditions. Synthesized fibers will be characterized and implemented in photocatalytic degradation experiments with CEES and DMMP, simulated chemical warfare agents. This chapter will cover the importance of a nucleophilic solvent to the hydrolysis of CEES as well as the influence of surface area to the efficiency of degradation by examining DMMP.

The third chapter reports the use of polymer composite nanofibers that have been further functionalized with metal-organic frameworks and their enhancement on the degradation of methyl paraoxon. The successful fabrication of polymer composite nanofibers containing 5 wt% UiO-66 and UiO-66 NH_2 is demonstrated. Synthesized fibers then undergo equivalent characterization as aforementioned. MOF/polymer composite fibers are then exposed to methyl paraoxon in both dark and UV conditions where the formation of degradation product is analyzed by using UV-Vis spectroscopy. This chapter will introduce the theory of multiple mechanistic pathways for the degradation of methyl paraoxon as well as demonstrate highest percent conversions and lowest half-lives to date.

The fourth chapter includes preliminary results on the use of Ag-TiO_2 nanofibers for enhancing degradation. Overall objectives include the use of surface plasmon resonant metals deposited on TiO_2 and coated with a J-aggregate dye to create a plasmon-exciton coupling nanocomposite that will enhance charge transfer to the surface of the semiconductor and enhance catalysis. This chapter will cover the fabrication of Ag-TiO_2 nanofibers via a polyol synthesis with silver nitrate, the characterization of these fibers and, preliminary degradation results when exposed to methyl paraoxon. Coating the surface of the metal deposited fibers with a J-aggregate dye and further experiments are discussed in the fifth chapter.

1.6 Current and Pending Publications

1.6.1 Patent Disclosure

1) Jones, W. E.; Bernier, W. E.; Liu, J.; McCarthy, D. L.; Obuya, E. A.; DeCoste, J. B.; Tollin, J. B. Metal oxide nanofibrous materials for photodegradation of environmental toxins. U.S. Patent Disclosure. Mar. 2015.

2) Jones, W. E.; Bernier, W. E.; McCarthy, D. L.; Troiano, J. E.; DeCoste J.B. Inorganic-organic hybrid polymer composite nanofiberous materials for degradation of toxins. U.S. Patent Disclosure. 2016

1.6.2 Publications

1) Jian Liu, Danielle L. McCarthy, Michael J. Cowan, Emilly A. Obuya, Jared B. Decoste, William E. Bernier, Wayne E. Jones, Jr., "Mechanism and Optimization of the Photocatalytic Activity for TiO2 Nanofibers with Variable Rutile Fraction", Applied Catalysis B: Environmental. 2016, vol 187, p. 154–162

2) Danielle L. McCarthy, Jian Liu, Julia B. Tollin, Jared B. DeCoste, William E. Bernier, Wayne E. Jones, Jr.," Nanofibrous TiO_2 for the Photocatalytic Degradation of Simulated CWA's: The Role of Surface Area.". *In Preparation.*

3) Danielle L. McCarthy, Jian Liu, Jennifer Troiano, Steven M. Boyer, Jared B. DeCoste, William E. Bernier,Wayne E. Jones, Jr., "Polymer composite nanofibers containing UiO-66 as a catalyst for the degradation of the chemical warfare agent simulant methyl paraoxon.". *In Preparation.*

4) Steven M. Boyer, Jian Liu, Sandy Zhang, Matthew I. Ehrlich, Danielle L. McCarthy, Linyue Tong, William E. Bernier, Wayne E. Jones, Jr., "Role of Ruthenium

Photosensitizers in the Degradation of Phenazopyridine with TiO_2 Electrospun Fibers". Journal of Photochemistry and Photobiology A: Chemistry. Submitted. 2016

5) Jian Liu , Danielle L. McCarthy , Linyue Tong , John M. Kinsley , Laura Sonnenberg, Kenneth H. Skorenko , Steven M. Boyer , Jared B. DeCoste , William E. Bernier , Wayne E. Jones, Jr., "Poly (3,4-ethylenedioxythiophene) Wrapped TiO2 Nanofibers for Enhanced Photocatalytic Degradation of Phenazopyridine". *In preparation.*

1.6.3 Preprints

1) Eliud K. Mushibe, Steven C. Murphy, Kate Raiti-Palazzolo, Danielle L Mccarthy, Emilly A. Obuya, Jasper Chiguma and Wayne E. Jones. Dielectric Nanowire Composites: One-Pot Synthesis of Gold Nanoparticles Encapsulated in Polyaniline Fibers. 2013. MRS Proceedings, 1453.

1.7 Selected Presentations

1) Role of TiO_2 nanocomposites of graphene and graphitic carbon for catalytic degradation of organic pollutants, 244th ACS National Meeting & Exposition, Philadelphia, PA, August 2012 *(Poster)*

2) Fabrication of TiO_2 nanofibers for photocatalytic degradation of environmental toxins, 247th American Chemical Society National Conference, Dallas, TX , March 2014 *(Oral)*

3) Fabrication of TiO_2/graphene electrospun nanofibers for photodegradation of biomedical and toxic pollutants, 247th American Chemical Society National Conference, Dallas, TX, March 2014 *(Poster)*

4) Electrospun composite nanofibers for enhanced photocatalytic degradation of environmental toxins. 250th American Chemical Society National Conference, Boston, Massachusetts, August 2015 *(Oral)*

1.8 References

1. Rushton, L., Health hazards and waste management. *British Medical Bulletin* **2003,** *68* (1), 183-197.

2. Gilliom, R. J., Pesticides in the hydrologic system- What do we know and what's next? *Hydrological Processes* **2001,** *15* (3197-3201).

3. Vala, R. K., Environmental fate and toxicology of organophosphate pesticides. *Journal of the Geological Society* **2000,** *157* (4), 859-876.

4. Dragun, J.; Kuffner, A. C.; Schneiter, R. W., Groundwater contamination. 1. Transport and transformation of organic-chemicals. *Chemical Engineering* **1984,** *91* (65-70).

5. Dowling, K. C.; Lemley, A. T., Organophosphate insecticide degradation by non-amended and cupric-ion-amended fentons reagent in acqueous solution. *Journal of Environmental Science and Health. Part B. Pesticides, Food Contamination and Agricultural Wastes* **1995,** *30*, 585-604.

6. Bondarenko, S.; Gan, J., Degradation and sorption of selected organophosphate and carbmate insecticides in urban stream sediments. *Environmental Toxicology and Chemistry* **2004,** *23* (8), 1809-1814.

7. Szinicz, L., History of chemical and biological warfare agents. *Toxicology* **2005,** *214* (3), 167-181.

8. Raushel, F. M., Chemical biology: Catalytic detoxification. *Nature* **2011,** *469* (7330), 310-311.

9. DeCoste, J. B.; Peterson, G. W., Metal–Organic Frameworks for Air Purification of Toxic Chemicals. *Chemical Reviews* **2014,** *114* (11), 5695-5727.

10. Rastogi, V. K.; Defrank, J. J.; Cheng, T.-c.; Wild, J. R., Enzymatic Hydrolysis of Russian-VX by Organophosphorus Hydrolase. *Biochemical and Biophysical Research Communications* **1997,** *241* (2), 294-296.

11. Kim, K.; Tsay, O. G.; Atwood, D. A.; Churchill, D. G., Destruction and Detection of Chemical Warfare Agents. *Chemical Reviews* **2011,** *111* (9), 5345-5403.

12. Fujishima, A.; Honda, K., Electrochemical Photolysis of Water at a Semiconductor Electrode. *Nature* **1972,** *238* (5358), 37-38.

13. Frank, S. N.; Bard, A. J., Heterogeneous photocatalytic oxidation of cyanide and sulfite in aqueous solutions at semiconductor powders. *The Journal of Physical Chemistry* **1977,** *81* (15), 1484-1488.

14. Dambournet, D.; Belharouak, I.; Amine, K., Tailored Preparation Methods of TiO2 Anatase, Rutile, Brookite: Mechanism of Formation and Electrochemical Properties. *Chemistry of Materials* **2010,** *22* (3), 1173-1179.

15. Cheng, H.; Ma, J.; Zhao, Z.; Qi, L., Hydrothermal Preparation of Uniform Nanosize Rutile and Anatase Particles. *Chemistry of Materials* **1995,** *7* (4), 663-671.

16. Pottier, A.; Chaneac, C.; Tronc, E.; Mazerolles, L.; Jolivet, J.-P., Synthesis of brookite TiO nanoparticles by thermolysis of TiCl in strongly acidic aqueous media. *Journal of Materials Chemistry* **2001,** *11* (4), 1116-1121.

17. Ji-Guang, L.; Chengchun, T.; Di, L.; Hajime, H.; Takamasa, I., Monodispersed Spherical Particles of Brookite-Type TiO2: Synthesis, Characterization, and Photocatalytic Property. *American Ceramics Society* **2004,** *87* (7), 1358-1361.

18. Zhang, H.; Banfield, J. F., Understanding Polymorphic Phase Transformation Behavior during Growth of Nanocrystalline Aggregates: Insights from TiO2. *The Journal of Physical Chemistry B* **2000,** *104* (15), 3481-3487.

19. Patterson, A. L., The Scherrer Formula for X-Ray Particle Size Determination. *Physical Review* **1939,** *56*, 978-982.

20. Su, R.; Bechstein, R.; Sø, L.; Vang, R. T.; Sillassen, M.; Esbjörnsson, B.; Palmqvist, A.; Besenbacher, F., How the Anatase-to-Rutile Ratio Influences the Photoreactivity of TiO2. *The Journal of Physical Chemistry C* **2011,** *115* (49), 24287-24292.

21. Zachariah, A.; Baiju, K. V.; Shukla, S.; Deepa, K. S.; James, J.; Warrier, K. G. K., Synergistic Effect in Photocatalysis As Observed for Mixed-Phase Nanocrystalline Titania Processed via Sol−Gel Solvent Mixing and Calcination. *The Journal of Physical Chemistry C* **2008,** *112* (30), 11345-11356.

22. Riegel, G.; Bolton, J. R., Photocatalytic Efficiency Variability in TiO2 Particles. *The Journal of Physical Chemistry* **1995,** *99* (12), 4215-4224.

23. Tian, G.; Fu, H.; Jing, L.; Xin, B.; Pan, K., Preparation and Characterization of Stable Biphase TiO2 Photocatalyst with High Crystallinity, Large Surface Area, and Enhanced Photoactivity. *The Journal of Physical Chemistry C* **2008,** *112* (8), 3083-3089.

24. Liu, J.; McCarthy, D. L.; Cowan, M. J.; Obuya, E. A.; DeCoste, J. B.; Skorenko, K. H.; Tong, L.; Boyer, S. M.; Bernier, W. E.; Jones Jr, W. E., Photocatalytic activity of TiO2 polycrystalline sub-micron fibers with variable rutile fraction. *Applied Catalysis B: Environmental* **2016,** *187*, 154-162.

25. Obuya, E. A.; Harrigan, W.; Andala, D. M.; Lippens, J.; Keane, T. C.; Jones Jr, W. E., Photodeposited Pd nanoparticle catalysts supported on photoactivated TiO2 nanofibers. *Journal of Molecular Catalysis A: Chemical* **2011,** *340* (1–2), 89-98.

26. Obuya, E. A.; Joshi, P. C.; Gray, T. A.; Keane, T. C.; Jones, W. E., Jr., Application of Pt.TiO2 nanofibers in photosensitized degradation of rhodamine B. *International Journal of Chemistry* **2014,** *6* (1), 1-16.

27. Eagles, D. M., Polar modes of lattice vibration and polaron coupling constants in rutile (TiO2). *Journal of Physics and Chemistry of Solids* **1964,** *25* (11), 1243-1251.

28. Schneider, J.; Matsuoka, M.; Takeuchi, M.; Zhang, J.; Horiuchi, Y.; Anpo, M.; Bahnemann, D. W., Understanding TiO2 Photocatalysis: Mechanisms and Materials. *Chemical Reviews* **2014,** *114* (19), 9919-9986.

29. Diebold, U., The surface science of titanium dioxide. *Surface Science Reports* **2003,** *48* (5–8), 53-229.

30. Deskins, N. A.; Rousseau, R.; Dupuis, M., Defining the Role of Excess Electrons in the Surface Chemistry of TiO2. *The Journal of Physical Chemistry C* **2010,** *114* (13), 5891-5897.

31. Martinez, U.; Hammer, B., Adsorption properties versus oxidation states of rutile TiO2 (110). *Journal of Chemical Physics* **2011,** *134*, 194703.

32. Chen, X.; Mao, S. S., Titanium Dioxide Nanomaterials: Synthesis, Properties, Modifications, and Applications. *Chemical Reviews* **2007,** *107* (7), 2891-2959.

33. Sugimoto, T., Preparation of monodispersed colloidal particles. *Advances in Colloid and Interface Science* **1987,** *28*, 65-108.

34. Sugimoto, T.; Zhou, X.; Muramatsu, A., Synthesis of uniform anatase TiO2 nanoparticles by gel–sol method: 4. Shape control. *Journal of Colloid and Interface Science* **2003,** *259* (1), 53-61.

35. Li, Y.; White, T. J.; Lim, S. H., Low-temperature synthesis and microstructural control of titania nano-particles. *Journal of Solid State Chemistry* **2004,** *177* (4–5), 1372-1381.

36. Zhang, H.; F. Banfield, J., Thermodynamic analysis of phase stability of nanocrystalline titania. *Journal of Materials Chemistry* **1998,** *8* (9), 2073-2076.

37. Wu, J.-M.; Zhang, T.-W.; Zeng, Y.-W.; Hayakawa, S.; Tsuru, K.; Osaka, A., Large-Scale Preparation of Ordered Titania Nanorods with Enhanced Photocatalytic Activity. *Langmuir* **2005,** *21* (15), 6995-7002.

38. Peng, X.; Chen, A., Aligned TiO2 nanorod arrays synthesized by oxidizing titanium with acetone. *Journal of Materials Chemistry* **2004,** *14* (16), 2542-2548.

39. Campbell, L. K.; Na, B. K.; Ko, E. I., Synthesis and characterization of titania aerogels. *Chemistry of Materials* **1992,** *4* (6), 1329-1333.

40. Corradi, A. B.; Bondioli, F.; Focher, B.; Ferrari, A. M.; Grippo, C.; Mariani, E.; Villa, C., Conventional and Microwave-Hydrothermal Synthesis of TiO2 Nanopowders. *Journal of the American Ceramic Society* **2005,** *88* (9), 2639-2641.

41. Gaya, U. I.; Abdullah, A. H., Heterogeneous photocatalytic degradation of organic contaminants over titanium dioxide: A review of fundamentals, progress and problems. *Journal of Photochemistry and Photobiology C: Photochemistry Reviews* **2008,** *9* (1), 1-12.

42. Tachikawa, T.; Fujitsuka, M.; Majima, T., Mechanistic Insight into the TiO2 Photocatalytic Reactions: Design of New Photocatalysts. *The Journal of Physical Chemistry C* **2007,** *111* (14), 5259-5275.

43. Vinodgopal, K.; Kamat, P. V., Photochemistry on surfaces: photodegradation of 1,3-diphenylisobenzofuran over metal oxide particles. *The Journal of Physical Chemistry* **1992,** *96* (12), 5053-5059.

44. Serpone, N.; Sauvé, G.; Koch, R.; Tahiri, H.; Pichat, P.; Piccinini, P.; Pelizzetti, E.; Hidaka, H., Standardization protocol of process efficiencies and activation parameters in heterogeneous photocatalysis: relative photonic efficiencies ζr. *Journal of Photochemistry and Photobiology A: Chemistry* **1996,** *94* (2–3), 191-203.

45. Yang, L.; Liu, Z., Study on light intensity in the process of photocatalytic degradation of indoor gaseous formaldehyde for saving energy. *Energy Conversion and Management* **2007,** *48* (3), 882-889.

46. Hoffmann, M. R.; Martin, S. T.; Choi, W.; Bahnemann, D. W., Environmental Applications of Semiconductor Photocatalysis. *Chemical Reviews* **1995,** *95* (1), 69-96.

47. Skinner, D. E.; Colombo, D. P.; Cavaleri, J. J.; Bowman, R. M., Femtosecond Investigation of Electron Trapping in Semiconductor Nanoclusters. *The Journal of Physical Chemistry* **1995,** *99* (20), 7853-7856.

48. Serpone, N.; Lawless, D.; Khairutdinov, R.; Pelizzetti, E., Subnanosecond Relaxation Dynamics in TiO2 Colloidal Sols (Particle Sizes Rp = 1.0-13.4 nm). Relevance to Heterogeneous Photocatalysis. *The Journal of Physical Chemistry* **1995,** *99* (45), 16655-16661.

49. Linsebigler, A. L.; Lu, G.; Yates, J. T., Photocatalysis on TiO2 Surfaces: Principles, Mechanisms, and Selected Results. *Chemical Reviews* **1995,** *95* (3), 735-758.

50. Hoskins, B. F.; Robson, R., Design and construction of a new class of scaffolding-like materials comprising infinite polymeric frameworks of 3D-linked molecular rods. A reappraisal of the zinc cyanide and cadmium cyanide structures and the synthesis and structure of the diamond-related frameworks [N(CH3)4][CuIZnII(CN)4] and CuI[4,4',4",4"'-tetracyanotetraphenylmethane]BF4.xC6H5NO2. *Journal of the American Chemical Society* **1990,** *112* (4), 1546-1554.

51. Farha, O. K.; Spokoyny, A. M.; Mulfort, K. L.; Hawthorne, M. F.; Mirkin, C. A.; Hupp, J. T., Synthesis and Hydrogen Sorption Properties of Carborane Based Metal−Organic Framework Materials. *Journal of the American Chemical Society* **2007,** *129* (42), 12680-12681.

52. Cavka, J. H.; Jakobsen, S.; Olsbye, U.; Guillou, N.; Lamberti, C.; Bordiga, S.; Lillerud, K. P., A New Zirconium Inorganic Building Brick Forming Metal Organic Frameworks with Exceptional Stability. *Journal of the American Chemical Society* **2008,** *130* (42), 13850-13851.

53. Kent, C. A.; Liu, D.; Meyer, T. J.; Lin, W., Amplified Luminescence Quenching of Phosphorescent Metal–Organic Frameworks. *Journal of the American Chemical Society* **2012,** *134* (9), 3991-3994.

54. Fateeva, A.; Chater, P. a.; Ireland, C. P.; Tahir, A. A.; Khimyak, Y. Z.; Wiper, P. V.; Darwent, J. R.; Rosseinsky, M. J., A Water-Stable Porphrin-Based Metal-Organic Framework Active for Visible-Light Photocatalysis. *Angewandte Chemie International Edition* **2012,** *51* (30), 7440-7444.

55. Fu, Y.; Sun, D.; Chen, Y.; Huang, R.; Ding, Z.; Fu, X.; Li, Z., An Amine-Functionalized Titanium Metal-Organic Framework Photocatalyst with Visible-Light-Induced Activity for CO2 Reduction. *Angewandte Chemie International Edition* **2012,** *51* (14), 3364-3367.

56. Horiuchi, Y.; Toyao, T.; Saito, M.; Mochizuki, K.; Iwata, M.; Higashimura, H.; Anpo, M.; Matsuoka, M., Visible-Light-Promoted Photocatalytic Hydrogen Production by Using an Amino-Functionalized Ti(IV) Metal–Organic Framework. *The Journal of Physical Chemistry C* **2012,** *116* (39), 20848-20853.

57. Kato, H.; Kudo, A., Visible-Light-Response and Photocatalytic Activities of TiO2 and SrTiO3 Photocatalysts Codoped with Antimony and Chromium. *The Journal of Physical Chemistry B* **2002,** *106* (19), 5029-5034.

58. Zhang, Z.; Yates, J. T., Band Bending in Semiconductors: Chemical and Physical Consequences at Surfaces and Interfaces. *Chemical Reviews* **2012,** *112* (10), 5520-5551.

59. Primo, A.; Corma, A.; Garcia, H., Titania supported gold nanoparticles as photocatalyst. *Physical Chemistry Chemical Physics* **2011,** *13* (3), 886-910.

60. Fuerte, A.; Hernandez-Alonso, M. D.; Maira, A. J.; Martinez-Arias, A.; Fernandez-Garcia, M.; Conesa, J. C.; Soria, J., Visible light-activated nanosized doped-TiO2 photocatalysts. *Chemical Communications* **2001,** (24), 2718-2719.

61. Xu, A.-W.; Gao, Y.; Liu, H.-Q., The Preparation, Characterization, and their Photocatalytic Activities of Rare-Earth-Doped TiO2 Nanoparticles. *Journal of Catalysis* **2002,** *207* (2), 151-157.

62. Sato, S., Photocatalytic activity of NOx-doped TiO2 in the visible light region. *Chemical Physics Letters* **1986,** *123* (1–2), 126-128.

63. Fattori, A.; Peter, L. M.; Wang, H.; Miura, H.; Marken, F., Fast Hole Surface Conduction Observed for Indoline Sensitizer Dyes Immobilized at Fluorine-Doped Tin Oxide−TiO2 Surfaces. *The Journal of Physical Chemistry C* **2010,** *114* (27), 11822-11828.

64. Zakeeruddin, S. M.; Nazeeruddin, M. K.; Humphry-Baker, R.; Péchy, P.; Quagliotto, P.; Barolo, C.; Viscardi, G.; Grätzel, M., Design, Synthesis, and Application of Amphiphilic Ruthenium Polypyridyl Photosensitizers in Solar Cells Based on Nanocrystalline TiO2 Films. *Langmuir* **2002,** *18* (3), 952-954.

CHAPTER 2: Electrospun TiO_2 Nanofibers vs. P25 Nanoparticles: The role of Surface Area in the Photocatalytic Degradation of Simulated Chemical Warfare Agents

2.1 Introduction

There is a broad array of needs for protection against chemical warfare agents (CWAs) and biological environmental toxins in the environment and around the world. Nanotechnology has provided novel systems for rapid decontamination and protection through a self-cleaning mechanism[1]. The potential applications are endless. One example currently being employed is self-cleaning glass in which TiO_2 switches from hydrophobic in the dark to both hydrophobic and hydrophilic during the day with UV irradiation, allowing adsorbed surface contaminants to be photomineralized and washed away by water.[2] TiO_2 is a suitable photocatalyst that meets the necessary requirements for mitigation of threatening toxins. The use of nanotubular titania against CWAs has been documented in the literature, with success in decontamination of agents such as HD, VX and GD.[3,4,5] Electrospun TiO_2 nanofibers will be explored as an alternative to other configurations of titania and will be compared to more commonly used P25 nanoparticles. The use of titania nanofibers could further enhance the hydrolysis and aid in the decontamination of toxic agents.

O-Pinacolyl methyl phosphonofluoridate, better known as GD or sarin is one of a number of deadly nerve agents of concern to warfighters on the modern battlefield. In the past sulfur mustard, bis-2-chloroethyl sulfide (HD) was a potent vesicant used on the battle field seen in WWI. Due to the toxicity of CWAs, simulants are used as an alternative to study. Dimethyl methylphosphonate is one SCWA for sarin and is commonly used in the laboratory to assess degradation.[6] 2-Chloroethyl ethyl sulfide (CEES) is a surrogate for the more toxic HD offering similar structural features allowing for the same reaction mechanism and similar physical properties.[7] Molecular structures of DMMP and CEES can be seen in **Figure 2-1**.

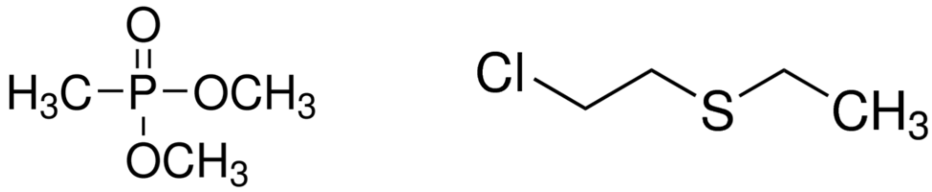

Dimethyl methylphosphonate

2-Chloroethyl ethyl sulfide

Figure 2-1. Molecular structures of simulants DMMP and CEES

The success of TiO_2 as a photocatalyst has been well documented in the literature.[8] Photocatalysts possess the ability to absorb incident irradiation in the UV or visible region of the spectrum to excite an electron from the valence band (leaving behind a positive hole) to the conduction band of a semiconductor. These photoinduced charge carriers can react with surface adsorbed species to form oxidizing and reducing species, as well as reactive radicals, such as hydroxyl and super oxide radicals. Once formed, these photochemical products can degrade chemicals that are adsorbed on the surface of the TiO_2 or diffuse to the surface during the lifetime of the reactive intermediate, **Figure 2-2.**

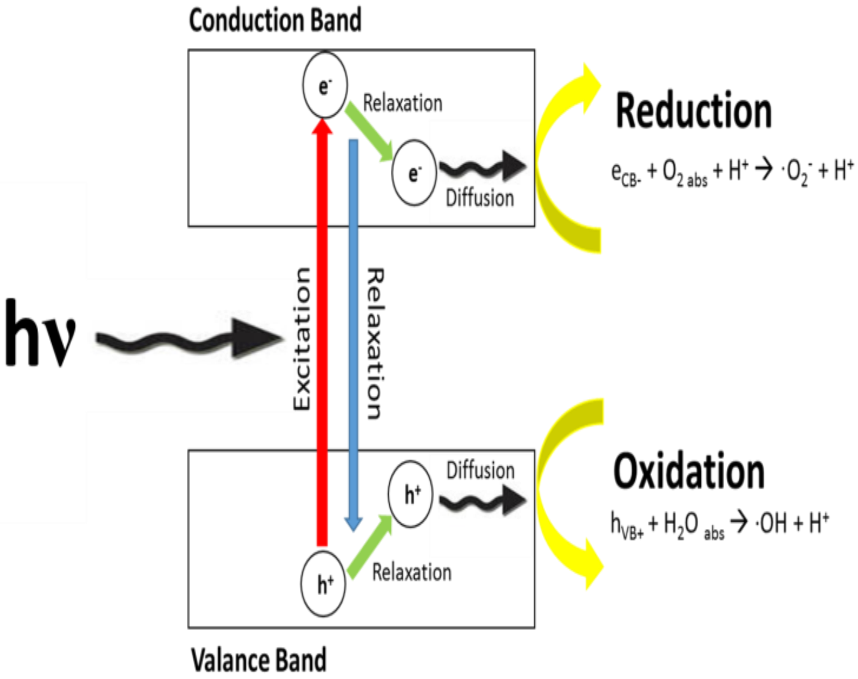

Figure 2-2. Mechanism of formation of the reactive species formed on the surface of TiO_2 due to photo excitation.

It has been documented that nanoparticles with a small percentage of rutile phase crystal fraction show enhanced photocatalytic activity, due to the efficient electron and hole separation between the rutile and anatase crystal phases.[9,10] TiO_2 nanofibers represent an alternative materials approach to conventional nanoparticle composites for use in photocatalytic degradation.[11,12,13] The one-dimensional morphology of TiO_2 nanofibers is preferred compared to spherical TiO_2 nanoparticles due to the excellent mobility of charge carriers, high surface area, the existence of pores enhancing the accessibility of electrodes to the hole transporting materials, and hence enhanced charge collection and transport.[14] Further, they provide a more environmentally friendly platform as their length makes them safer relative to pure nanoparticles.[15]

Electrospinning is a common technique used in the fabrication of nanofibers. It is safe, easy to operate and suitable for scaling-up compared to other methods of fabrication. TiO_2 nanofibers can be prepared by electrospinning a polymeric sol-gel solution followed by a thermal treatment. A variety of polymers could be used for this process, including but not limited to, polymethyl methacrylate (PMMA)[11], polyvinylpyrrolidone (PVP)[16], polyethylene (PEO),[17] and polyvinyl alcohol (PVA)[18]. Altering the polymer subsequently will change the formation of TiO_2. Electrospinning is a non-mechanical, electrostatic process that can produce fibers in the nanometer to micrometer range using electrically driven jets of polymer solution.[19,20] In this process, a highly charged electric field is created between the sol gel solution and an electrically grounded collector. A thin jet is formed from a polymer solution with a volatile organic solvent when the electrical field overcomes the surface tension allowing it to be drawn from the syringe and pulled to the grounded collector.[21,22]

In this chapter the focus will be the preparation of TiO_2 nanofibers to be used as a photocatalyst by electrospinning. The hydrolysis mechanisms of CEES and DMMP in the presence of these photocatalysts will be explored as well as the degradations of the SCWAs in non-nucleophilic solvents and solventless reactions. The degradation of DMMP will be analyzed and directly compared with commercially available nanoparticles structures demonstrating improved efficiency of degradation and the role of surface area.

2.2 Experimental

2.2.1 Materials

Polymethylmethacrylate (PMMA) (M_w960,000), titanium (IV) isopropoxide (TTiP), N,N-dimethylformamide (DMF), chloroform, Degussa P25 titania nanoparticles, dimethyl methylphosphonate (DMMP), 2-chloroethyl ethyl sulfide (CEES), acetone, acetonitrile, toluene, dimethylsulfoxide (DMSO), acetonitrile-d3, and acetone-d6 were purchased from Sigma Aldrich and used without further purification.

2.2.2 Synthesis of TiO_2 Nanofibers

TiO_2 nanofibers were fabricated using a sol gel synthesis and electrospinning followed by a thermal treatment. A sol gel solution in a 1:2 ratio of PMMA to TTiP was prepared in a 1:1 ratio of chloroform and N,N-dimethylformamide. 320 mg of PMMA was dissolved in 2 mL of chloroform and allowed to stir until polymer was dissolved. 0.67 mL of TTiP was added dropwise to the polymer solution and allowed to stir for an additional 30 min. At this point 2 mL of DMF was added to the solution to increase the dielectric constant and stirred for a further 2 h prior to electrospinning.

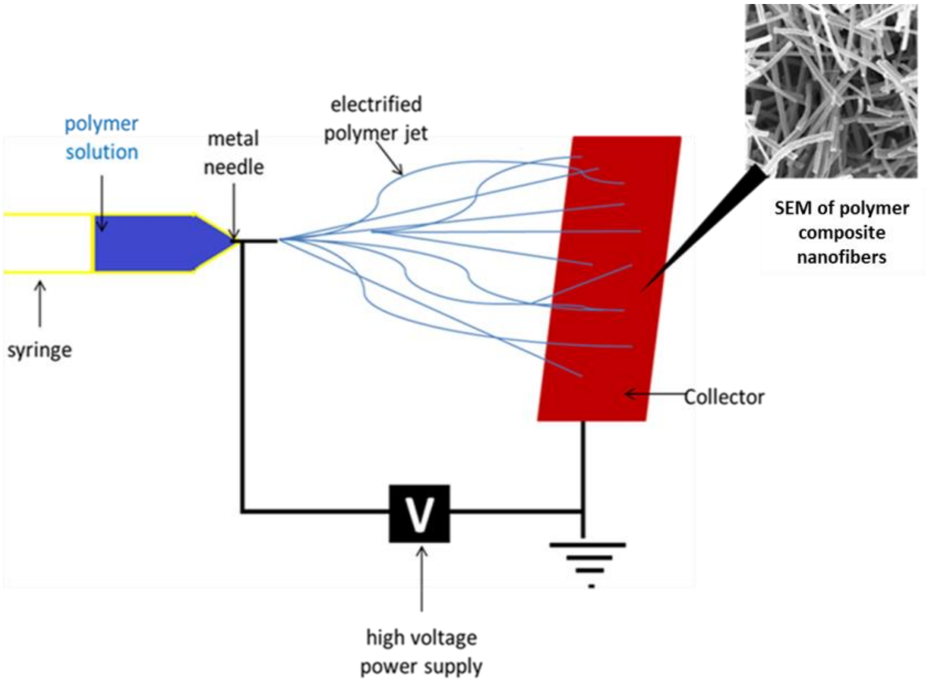

Figure 2-3. Schematic figure of electrospinning apparatus used to fabricate TiO_2 nanofibers.

A Spellman SL 30 generator is used to apply 25kV/cm across the sol gel polymer solution resulting in the deposition of nanofibers on the electrically charged collector. A schematic of the electrospinning apparatus can be seen in **Figure 2-3**. The resulting polymer composite nanofibers are given approximately 12 h to stand at room temperature under ambient conditions. This allows for complete the hydrolysis of TTiP to $Ti(OH)_4$ and then further condensation to amorphous TiO_2 prior to thermal treatment.[23] The fibers are then collected and calcined in a Thermo Scientific Lindberg Blue M Mini-Mite Tube Furnace, 16-Pt; 120V tube furnace at 400°C for 4 h under atmospheric conditions.

2.2.3 Photodegradation Procedure for 2-Chloroethyl ethyl sulfide

2.2.3.1 Degradation of 2-Chloroethyl ethyl sulfide without Catalyst

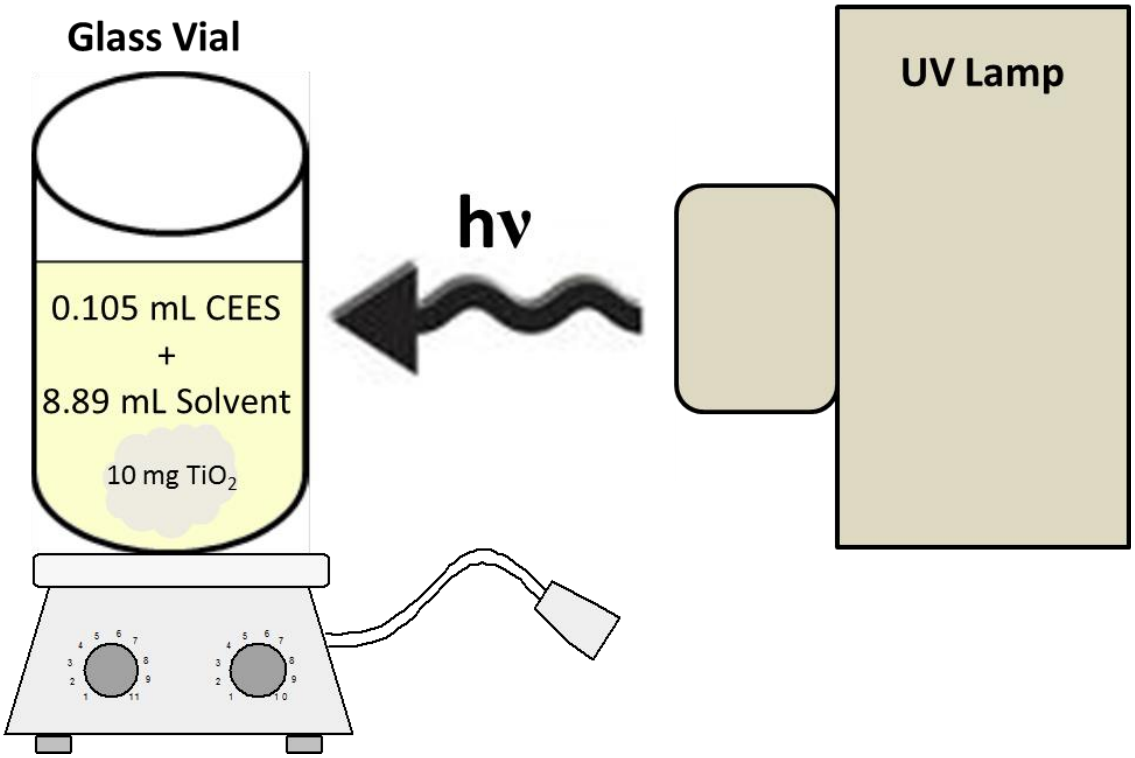

Figure 2-4. Reaction set-up for degradation of CEES with non-nucleophilic solvents.

A 0.1 M solution of CEES was prepared using several different non- nucleophilic solvents in attempt to prevent the hydrolysis of CEES both with and without the presence of TiO_2. 0.105 mL of CEES was added to 8.89 mL of solvent (acetone, acetonitrile, toluene, DMSO) in a 50 mL glass beaker. A 0.4 mL aliquot was extracted immediately and diluted with 0.1 mL of acetone-d6 and analyzed via Bruker Advance III 600 MHz NMR. The reaction set up can be seen in **Figure 2-4**. Upon extraction of the initial aliquot the solution was then irradiated with UV light for 2 h using an Oriel 66001 UV lamp with Oriel 68805 40-200 Watt universal Arc lamp power supply, which covers the 100- 400 nm range. The distance between the center of the solution container and the UV lamp was controlled at 9 cm. A 0.4 mL aliquot was extracted at t=1, 2 h of irradiation and diluted with 0.1 mL acetone- d6. ^{13}C and ^{1}H NMR spectra were collected for all aliquots extracted during the course of the experiment.

2.2.3.2 Solventless Degradation of 2-Chloroethyl ethyl sulfide with TiO_2 Nanofibers

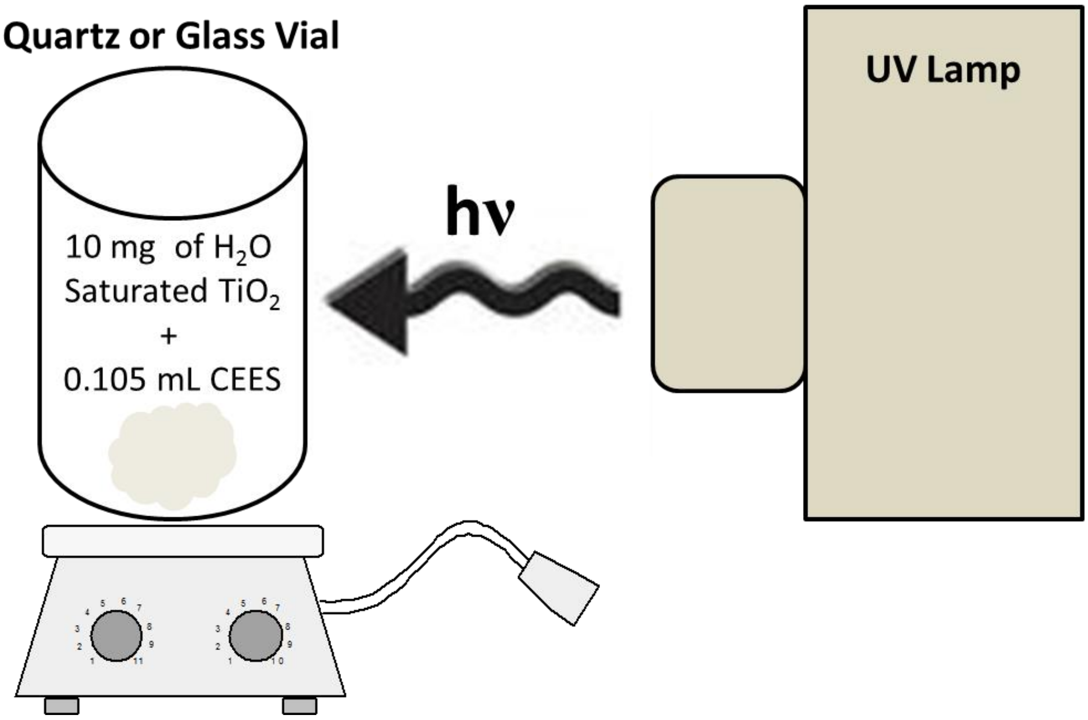

Figure 2-5. Reaction set-up for solventless degradation of CEES with TiO_2 nanofibers

Three quartz vials were prepared for the degradation of CEES with TiO_2 nanofibers. Each vial contained 10 mg of TiO_2 nanofibers that were exposed 0.5 mL of deionized water for 1 hour prior to addition of CEES. The reaction set up can be seen in **Figure 2-5**. This allowed for the saturation of catalyst since absorbed water is responsible for the formation of hydroxyl radicals. 0.1 M of CEES was added dropwise directly to the nanofibers in each of the vials at which time UV irradiation began. Samples were analyzed via Bruker Advance III 600 MHz NMR every 6 h for 14 h. Extraction was done using 1 mL of acetonitrile-d3. Sample was centrifuged and remaining solution was used for ^{13}C and ^{1}H NMR. Experiments were also performed in the dark as a comparison to determine the role of UV irradiation to the degradation of CEES.

2.2.4 Photodegradation Procedure for Dimethyl methylphosphonate

Photocatalytic degradation experiments were carried out under ambient conditions within a fume hood. A solid sample of TiO_2 nanofibers and P25 nanoparticles (50 mg) was added to 10 mL of a 100 μM solution of DMMP in a quartz reaction vial. The suspension was stirred vigorously over a 2 h period in the presence of UV irradiation using an Oriel 66001 UV lamp with Oriel 68805 40-200 Watt universal Arc lamp power supply, which covered the 100- 400 nm range. The distance between the center of the solution container and the UV lamp was controlled at 9 cm. A 1.0 mL aliquot of the solution was extracted at t= 0, 1, and 2 h for analysis via Bruker Advance III 600 MHz NMR. Aliquots were then centrifuged for 3 min to separate the catalyst and solution. 0.8 mL of the centrifuged solution was diluted with 0.2 mL of acetonitrile-d3. The prepared sample was characterized by ^{31}P NMR. Sample analyses for photodegradations were performed in deionized water unless otherwise noted.

2.2.5 Characterization Methods

A Spellman SL 30 HV generator was used to apply a high voltage across the copper wire to create a high electrical potential attaching to the collector. Thermal treatment was done using a Thermo Scientific Lindberg Blue M Mini-Mite Tube Furnace, 16-Pt; 120V tube furnace heated to 400°C for 4 h under atmospheric conditions. Photodegradations used an Oriel 66001 UV lamp with Oriel 68805 40-200 Watt universal

Arc lamp power supply, which covered the entire ultra-violet, 100- 400 nm range. The morphological and structural characteristics of the nanofibers and nanoparticles were measured by field emission scanning electron microscopy (FESEM, Supra 55 VP from Zeiss equipped with an EDAX energy dispersive X-ray spectroscopy detector), and X-ray diffraction (XRD, PANalytical's X'Pert PRO Materials Research Diffractometer with Cu Kα radiation (λ = 1.5418 Å)), respectively. Transmission electron microscopy (TEM) images were obtained from JEOL 2010 FETEM instrument. The TEM samples were dispersed in ethanol by sonication and the resulting solution were placed on a lacey carbon grid, which was left in air to evaporate the solvent. Nitrogen adsorption isotherms were measured for post-calcined TiO_2 nanofibers using a Micromeritics TriStar 3000 analyzer at 77 K. Prior to analysis, each material was off-gassed overnight at 250°C under a flow of dry nitrogen. Brunauer-Emmett-Teller (BET) modeling was performed to obtain the specific surface areas (m^2/g).

2.3 Results and Discussion

2.3.1 Characterization of TiO_2 Nanofibers

A sol gel solution in a 1:2 ratio of PMMA to TTiP was prepared in a 1:1 ratio of chloroform and N,N-dimethylformamide. A high voltage power supply was used to apply 25kV/cm across the sol gel polymer solution resulting in the deposition of nanofibers on the electrically charged collector. Approximately twelve hours is allowed for fibers to stand at room temperature and under atmospheric conditions to promote hydrolysis. The fibers were then collected and calcined at 400°C for 4 h under atmospheric conditions. The resulting TiO_2 nanofibers where characterized using SEM, TEM, XRD and BET to compare to the characteristics P25 nanoparticles prior the degradation experiments with CEES and DMMP.

2.3.1.1 Scanning Electron Microscopy and Transmission Electron Microscopy

Figure 2-6. SEM image of PMMA/TTiP pre-calcined fiber.

The electrospun pre-calcined polymer fibers were investigated by SEM as shown in **Figure 2-6**. The image shows the fibers possess a folded and wrinkled surface morphology, with diameters consistent throughout the sample of approximately 900 nm. The diameter of the fibers is inconsistent throughout, varying from a few hundred nanometers to a few microns. The fibers vary in length from a <2 μm to >5 μm. The variation in lengths of the fibers could be attributed to the electrospinning process where there is a break in the circuit of the continuous electrified jet being collected, resulting in different lengths of fibers or during the sample preparation for imaging which would lead one to conclude that the fibers are brittle in nature.

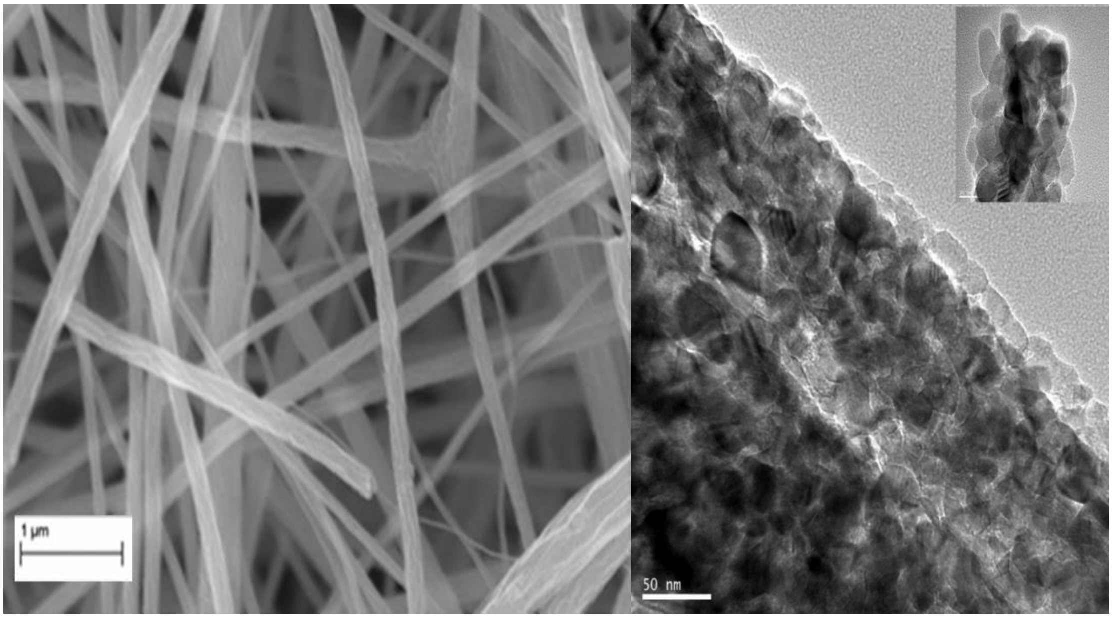

Figure 2-7. SEM (right) and TEM (left) imaging of TiO_2 nanofibers

After 400 °C thermal treatment, TiO_2 nanofibers exhibited diameters that varied slightly within the sample, but averaged approximately 300 ± 50 nm. It can also be seen that the calcined nanofibers retain the folded and wrinkled surface morphology seen in the pre-calcined fibers, **Figure 2-7**. The resulting nanofibers became even smaller in length after the thermal treatment and preparation for imaging. This confirmed suspicions on the fragile nature of the fibers that by simply placing them into a crucible for calcination and mounting to an aluminum SEM stub results in breaking. There is no indication the length of the nanofiber will play a critical role in degradation, however, it is hypothesized that this surface morphology of the nanofiber may increase the surface interface between the targeted toxins and the catalyst.

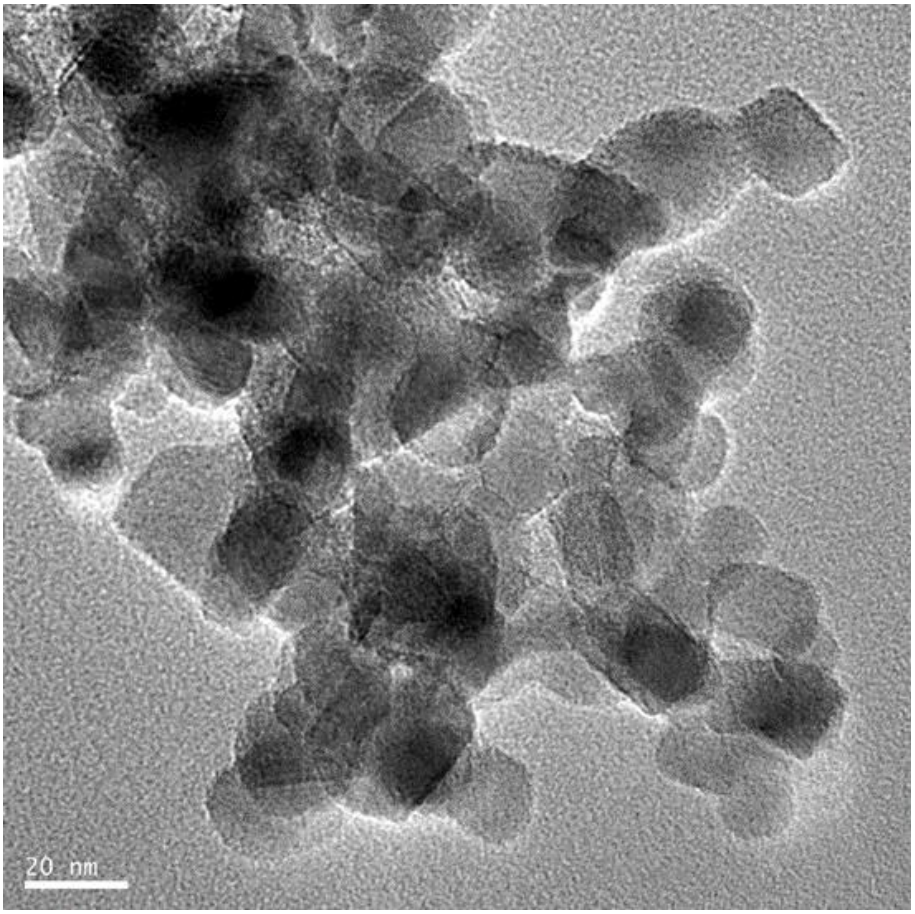

Figure 2-8. TEM image of P25 nanoparticles

Degussa P25 nanoparticles were commercially bought from Sigma Aldrich and used without any further treatment. TEM imaging was done to confirm the 21 nm diameter particles per description of the company, **Figure 2-8**. Imaging showed some variation in diameters of the particles with some being well below 21 nm and others being well above. Results concluded the average diameter of the nanoparticles was 27 nm ± 9 nm.

2.3.1.3 X-Ray Diffraction and Brunauer-Emmett-Teller Nitrogen Isotherm

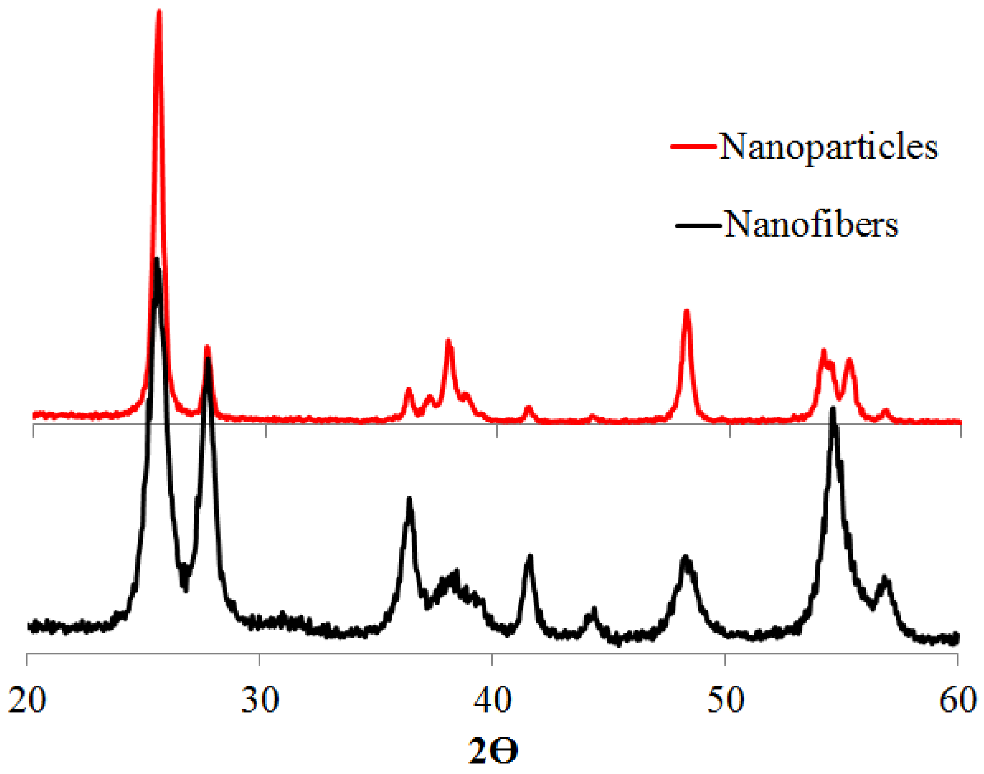

Figure 2-9. XRD Pattern of TiO_2 nanofibers and P25 nanoparticles

The XRD pattern of post-calcined TiO_2 nanofibers at 400°C under atmospheric conditions is shown in **Figure 2-9**. Well defined diffraction peaks show the presence of both anatase and rutile phases. This adds further evidence to the origin of the fluctuating diameter during the calcination process where grains are produced. For the anatase phase, the major peaks were obtained at 2θ values of 25.5, 37.9, and 48.2° representing the Miller indices of (101), (004), and (200) planes, respectively. For the rutile phase, peaks were observed at 2θ values of 27.6, 36.1, 41.2, and 54.3°, respectively, representing the Miller indices of (110), (101), (111), and (211) planes, respectively. The weight fraction of rutile phase is calculated to be 48 wt% from the equation of $W_R=1/[1+0.8(I_A/I_R)]$, where I_A is the X-ray integrated intensities of the (101) reflection of anatase at 2θ of 25.5° and I_R is that of the (110) reflection of rutile at 2θ of 27.6°. The rutile weight fraction was calculated under the same conditions and resulted in a 19% rutile fraction. This is consistent with the literature which states P25 possesses an anatase rutile fraction of 80/20.[24] Values can be seen in **Table 2-1.**

Sample	**% Anatase/ %Rutile**	**Surface Area (m^2/g)**
P25 Nanoparticles	81/19	52
TiO_2 Nanofibers	52/48	51

Table 2-1. Table of BET surface area measurements and respective percentages of antase and rutile

BET analysis shows that the electrospun anatase/rutile nanofibers with a 52/48 ratio are almost identical to the surface area of the P25 nanoparticles. This data can be seen directly in **Table 2-1.** Degussa P25 nanoparticles are well known throughout the literature to possess small diameters (21nm) and high surface areas (35-65m^2/g). The surface area and rutile fraction correlated with values provided by the supplier Sigma Aldrich. The folded and wrinkled surface morphology of the nanofiber seen in the SEM and TEM images contributed to the increase in surface area making it comparable to the surface area of P25 nanoparticles.

2.3.2 Photocatalytic Degradation of 2-Chloroethyl ethyl sulfide

2.3.2.1 Hydrolysis mechanism of 2-Chloroethyl ethyl sulfide

Mechanistic pathways of the hydrolysis degradation of CEES have been documented in the literature.[25] The formation of sulfonium salt as byproducts to the hydrolysis to CEES can result from multiple product pathways that are dependent on concentration. Higher concentrations will lead to different equilibrium rates and formations of multiple salts as seen in **Figure 2-10**.

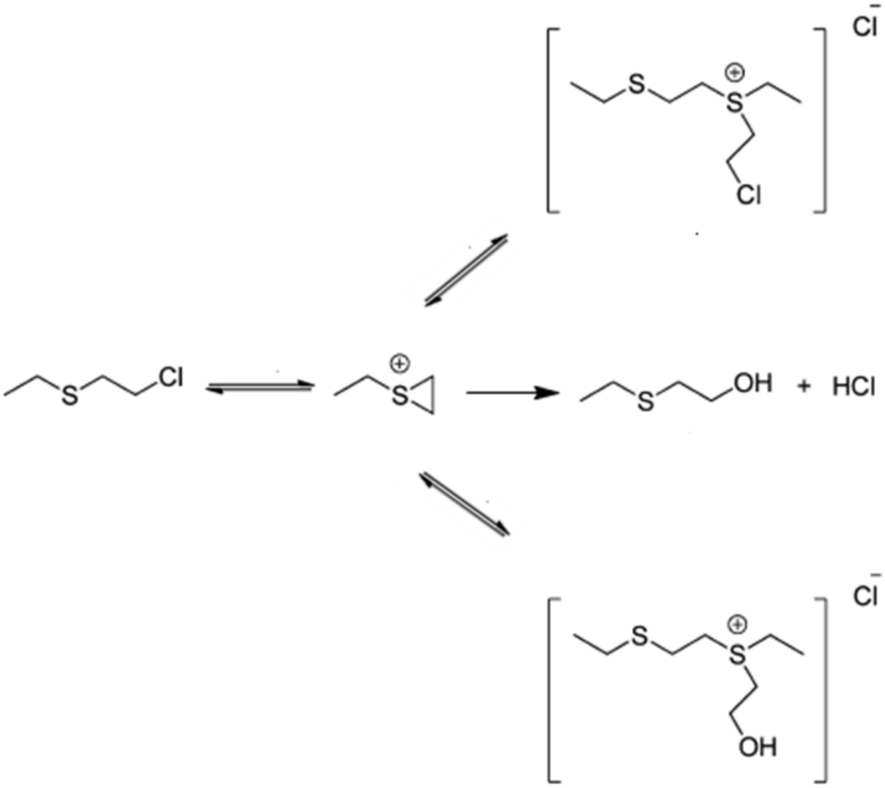

1

2

3

Figure 2-10. Proposed mechanistic pathways of the hydrolysis of CEES. Adapted from Bae, S.Y. and Winemiller, M.D. *J. Org. Chem*. 2013, 78, 6457-6470

To examine the aforementioned hydrolysis mechanism, a study was performed and verified using ^{13}C NMR. A 1.4 M aqueous solution of CEES was prepared for ^{13}C NMR analysis of the hydrolysis over 120 min. Over the course of the experiment the solution was stirred in the dark. The solubility of CEES is low and required vigorous stirring to allow CEES to go in to solution. An aliquot was extracted from the solution at t= 0 min for a baseline comparison. Aliquots were then extracted again at t= 60 min and t= 120 min and analyzed via ^{13}C NMR.

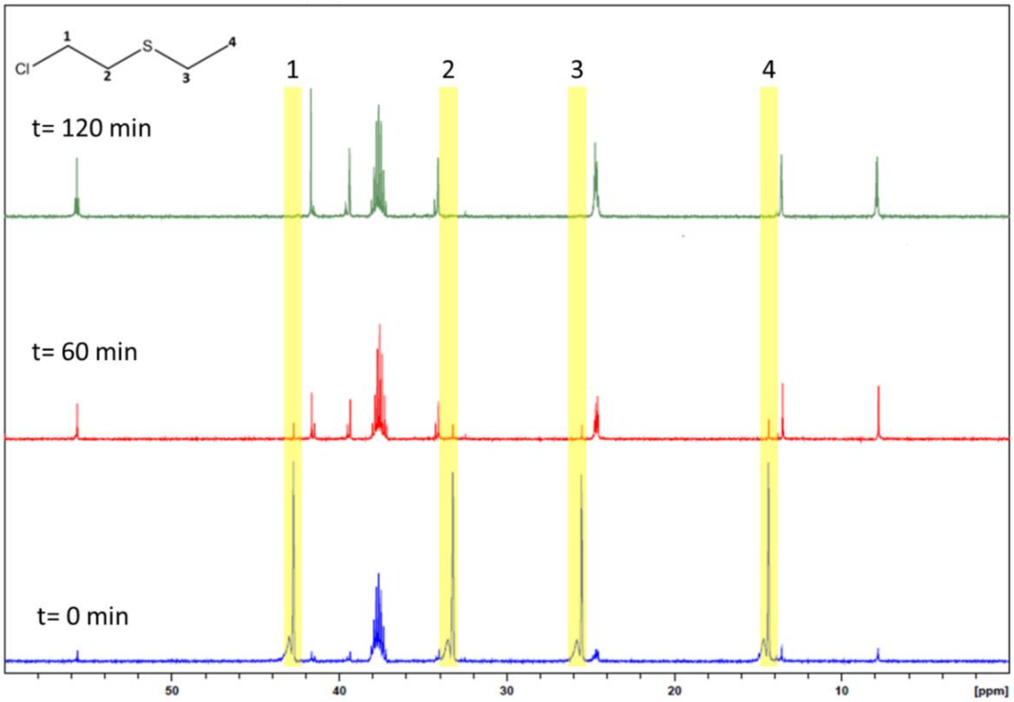

Figure 2-11. ^{13}C NMR of hydrolysis of CEES over 120 minutes.

The resulting ^{13}C NMR displayed in **Figure 2-11** shows that after 120 min exposure of the target pollutant to water, the four singlets corresponding to CEES had disappeared. The resulting formation of peaks in **Figure 2-11** green is indicative of the products shown in the aforementioned hydrolysis mechanism. Sulfonium salt **1** has a doublet at 41 ppm, sulfonium salt **2** has a singlet at 32 ppm which can faintly be seen after 120 min. Sulfonium salt **3** has a strong singlet at 56 ppm. The conclusion can be drawn that all three products are present in solution after the hydrolysis of CEES.

2.3.2.2 Non-nucleophilic Solvent Photodegradation of 2-Chloroethyl ethyl sulfide

After gaining a better understanding for the hydrolysis reaction of CEES, the effect of non-nucleophilic solvents on CEES was examined. With the addition of a catalyst to promote decontamination without relying on the presence of a nucleophilic solvent such as water. 0.105 mL of CEES was added to 8.89 mL of several different solvents. First was acetonitrile, the solution was stirred in the dark for 60 min, allowing CEES to go into solution at which time the solution was irradiated with UV light for the remaining 60 min. Aliquots were extracted periodically and analyzed via ^{13}C NMR. In the case of acetonitrile there was no decrease in intensity over the 120 min experiments. The experiment was again repeated under the same conditions with toluene, DMSO and acetone. The results can be seen in **Figures 2-12 to 2-15** respectively.

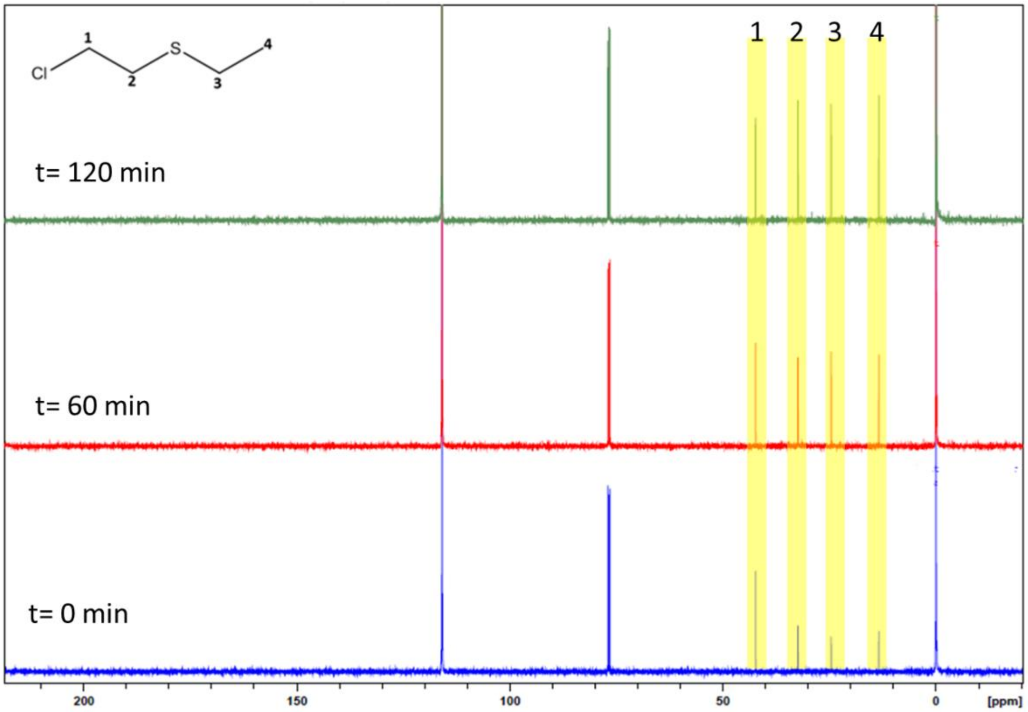

Figure 2-12. ^{13}C NMR- Degradation of CEES in acetonitrile with no catalyst. First 60 min in the dark, final 60 min the sample was exposed to UV irradiation.

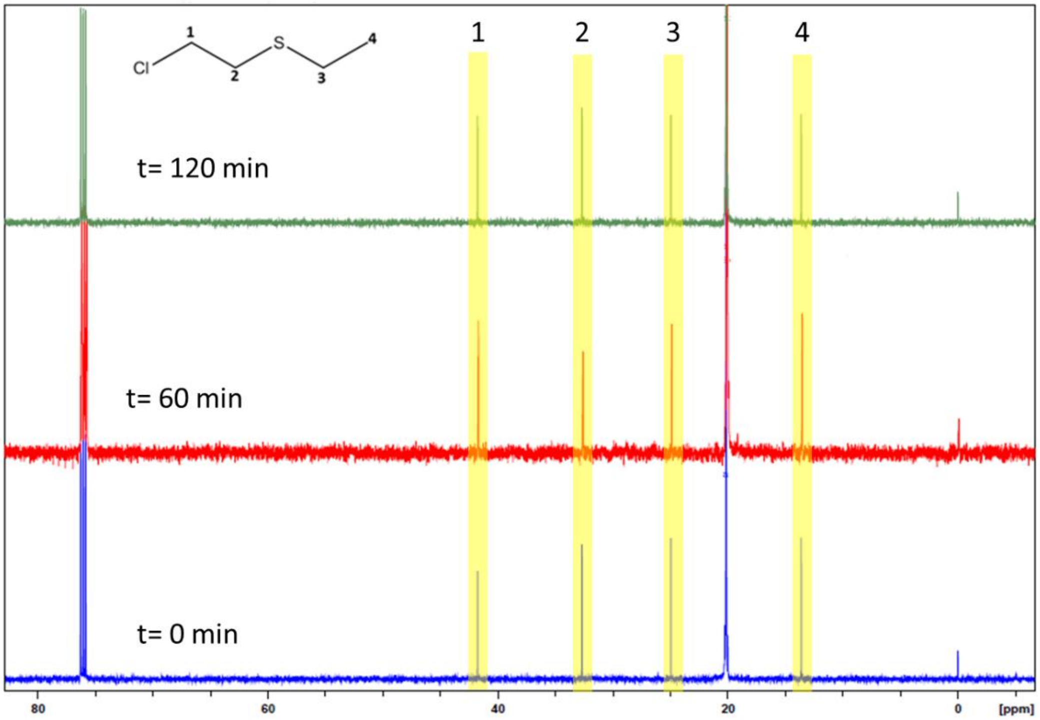

Figure 2-13. ^{13}C NMR- Degradation of CEES in toluene with no catalyst. First 60 min in the dark, final 60 min the sample was exposed to UV irradiation.

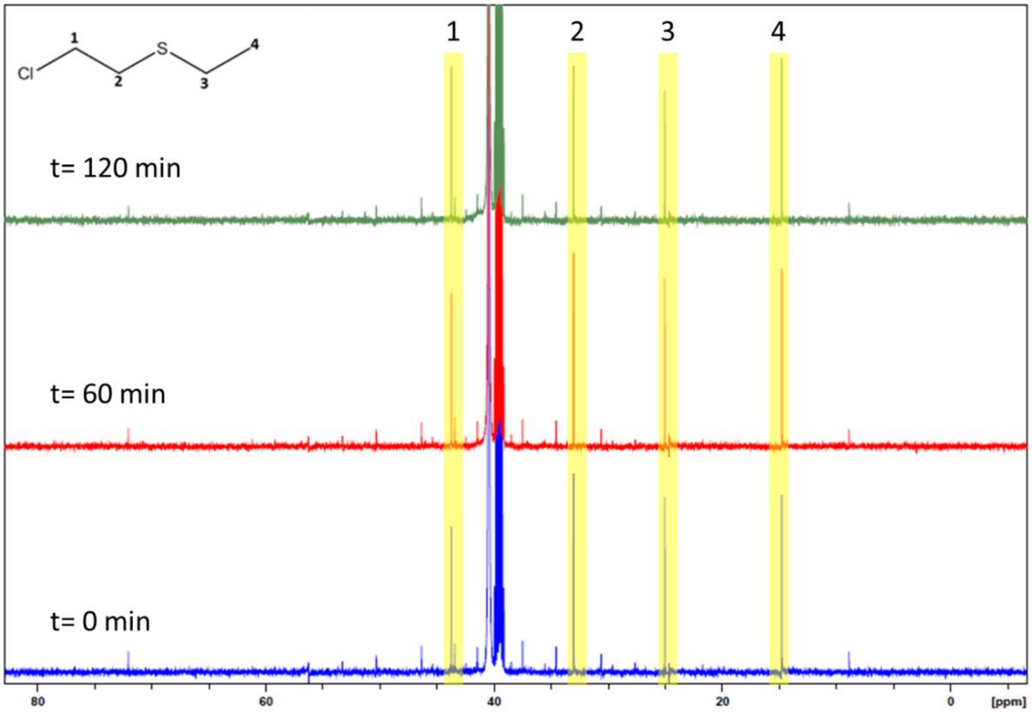

Figure 2-14. ^{13}C NMR- Degradation of CEES in DMSO with no catalyst. First 60 min in the dark, final 60 min the sample was exposed to UV irradiation.

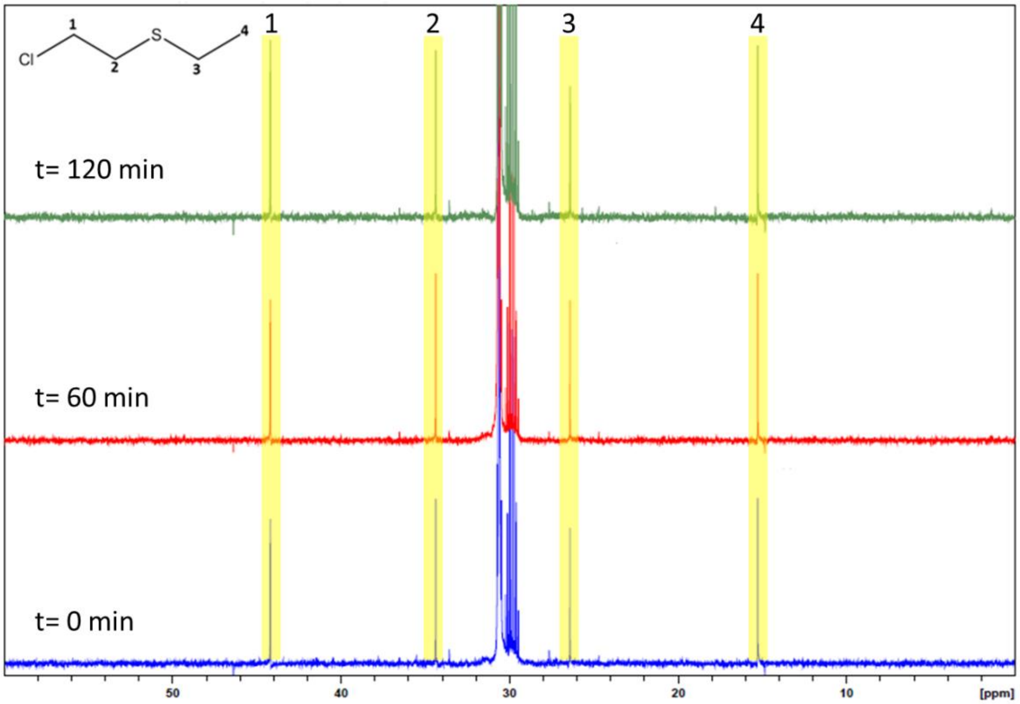

Figure 2-15. ^{13}C NMR- Degradation of CEES in acetone with no catalyst. First 60 min was in the dark, final 60 min the sample was exposed to UV irradiation.

The results were consistent when using non-nucleophlic solvents to degrade CEES. There was little to no change over the course of 120 min. The results from the experiments with CEES and no catalyst led to the same experiments being repeated but in the presence of photocatalyst. 50 mg of TiO_2 was added to the CEES solution and allowed to stir for 1 h prior to UV irradiation. The solution was then irradiated and aliquots were extracted periodically and analyzed via ^{13}C NMR. Results can be seen in **Figures 2-16 to 2-19**, respectively.

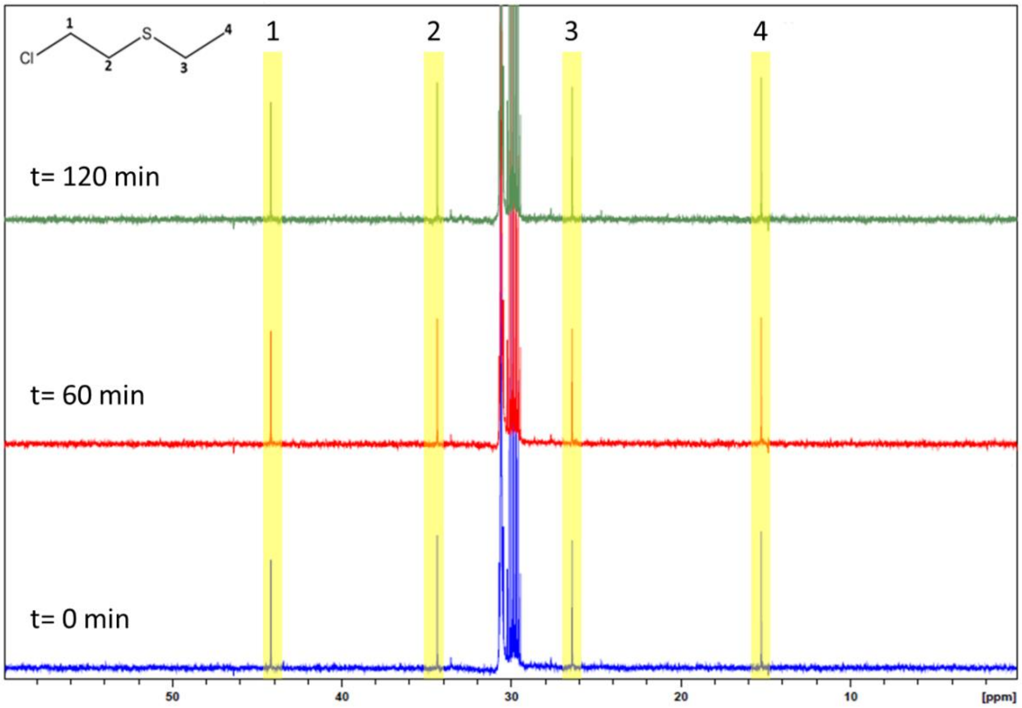

Figure 2-16. ^{13}C NMR- Degradation of CEES with TiO_2 nanofibers in acetone. First 60 min was in the dark, final 60 min the sample was exposed to UV irradiation.

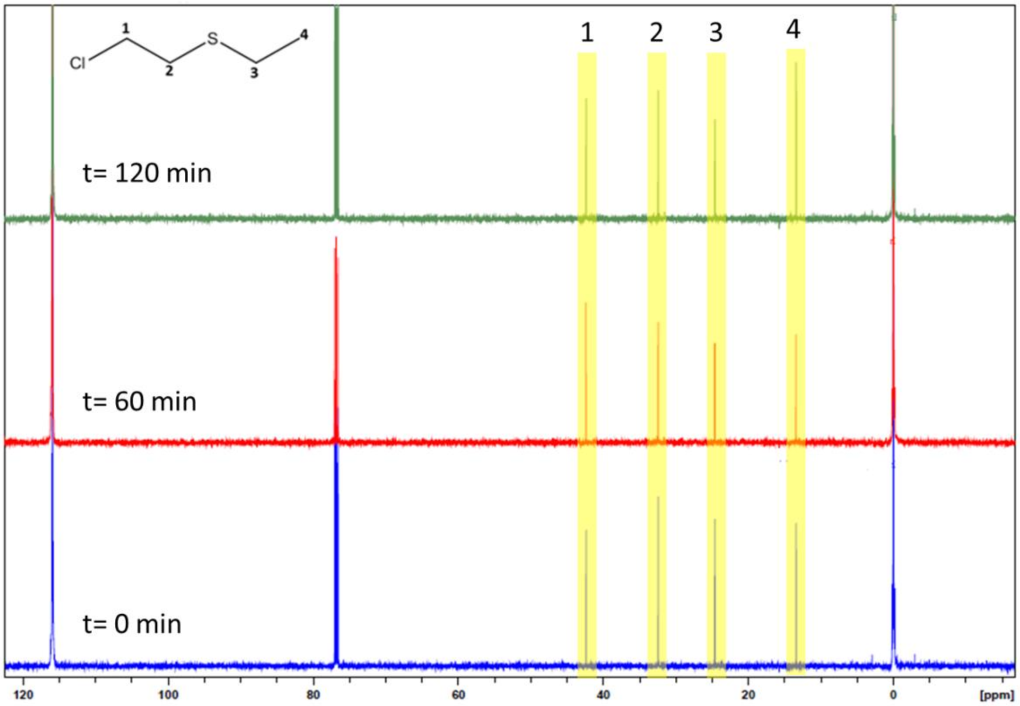

Figure 2-17. ^{13}C NMR- Degradation of CEES with TiO_2 nanofibers in acetonitrile. First 60 min was in the dark, final 60 min was exposed to UV irradiation.

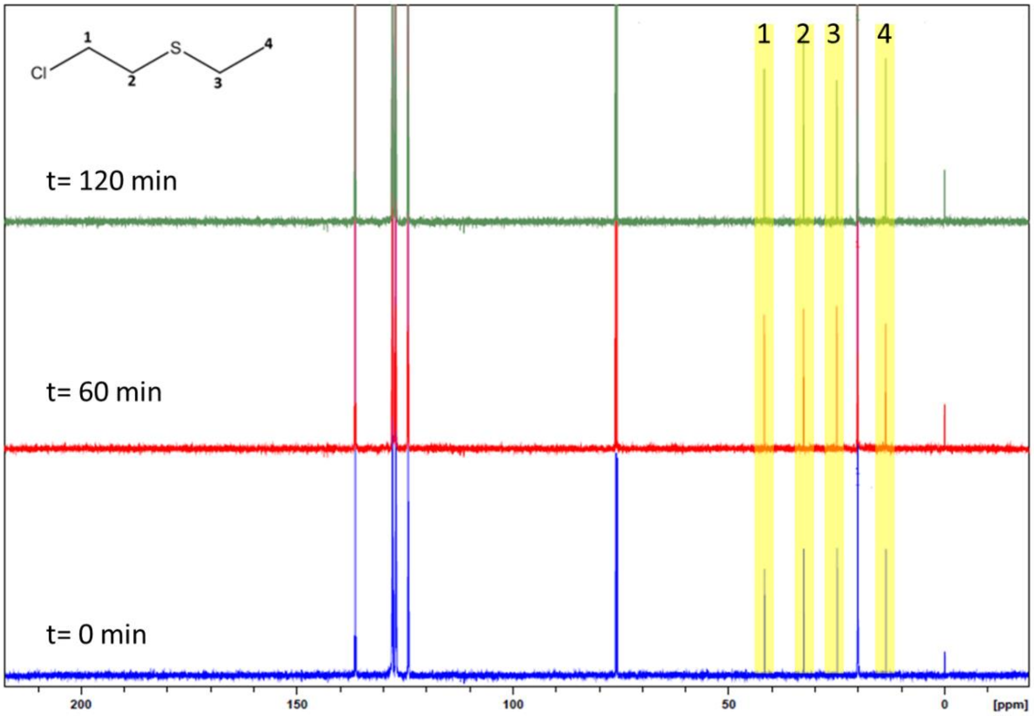

Figure 2-18. ^{13}C NMR- Degradation of CEES with TiO_2 nanofibers in toluene. First 60 min was in the ark, final 60 min the sample was exposed to UV irradiation.

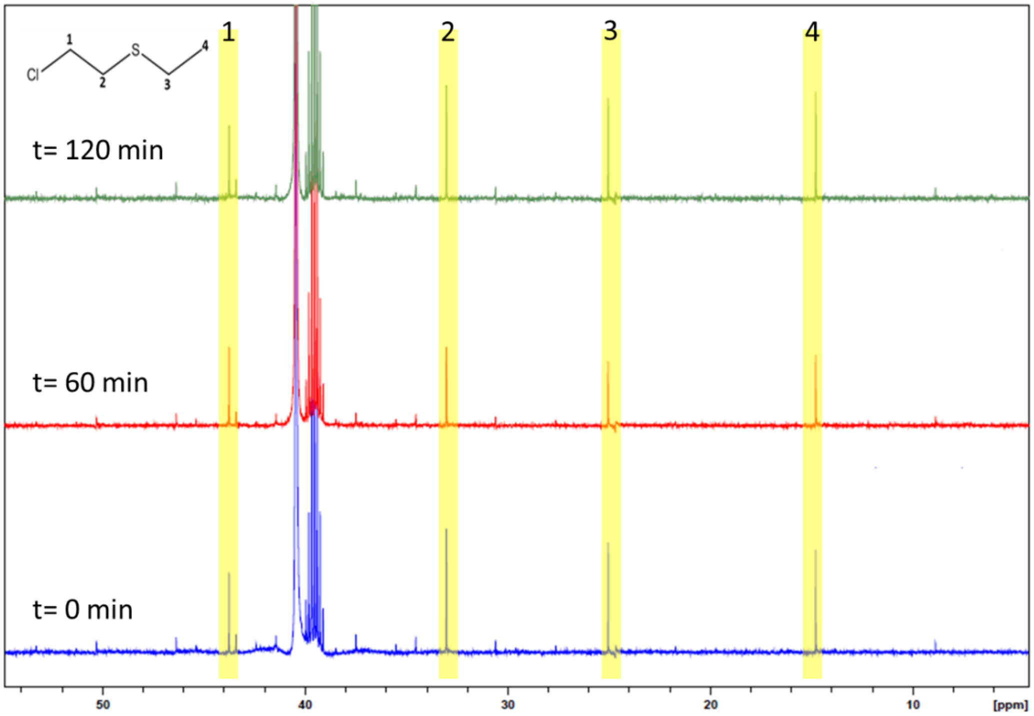

Figure 2-19. ^{13}C NMR- Degradation of CEES with TiO_2 nanofibers in DMSO. First 60 min was in the dark, the final 60 min was exposed to UV irradiation.

Analysis of the NMR spectra showed that even in the presence of UV light and a photocatalyst, no degradation occurred over the course of 120 min. The results of the experiments both with and without the catalyst lead to the conclusion that a polar solvent is a necessary for the degradation mechanism of CEES.

2.3.2.3 Solventless Photodegradation of 2-Chloroethyl ethyl sulfide

It is imperative for TiO_2 to photocatalytically degrade a pollutant that both water and UV irradiation are present during the degradation process. In the case of non-nucleophilic solvents, the lack of absorbed water would not promote the formation of a hydroxyl radical. The absence of UV irradiation for the catalyst could also prevent degradation. The reactions were being performed in a Pyrex vial. As seen in **Figure 2-**

20, this vial will absorb the majority of the UV light. Therefore, the incident radiation is not able to reach the catalyst and generate the electron-hole pairs required for photocatalytic degradation.

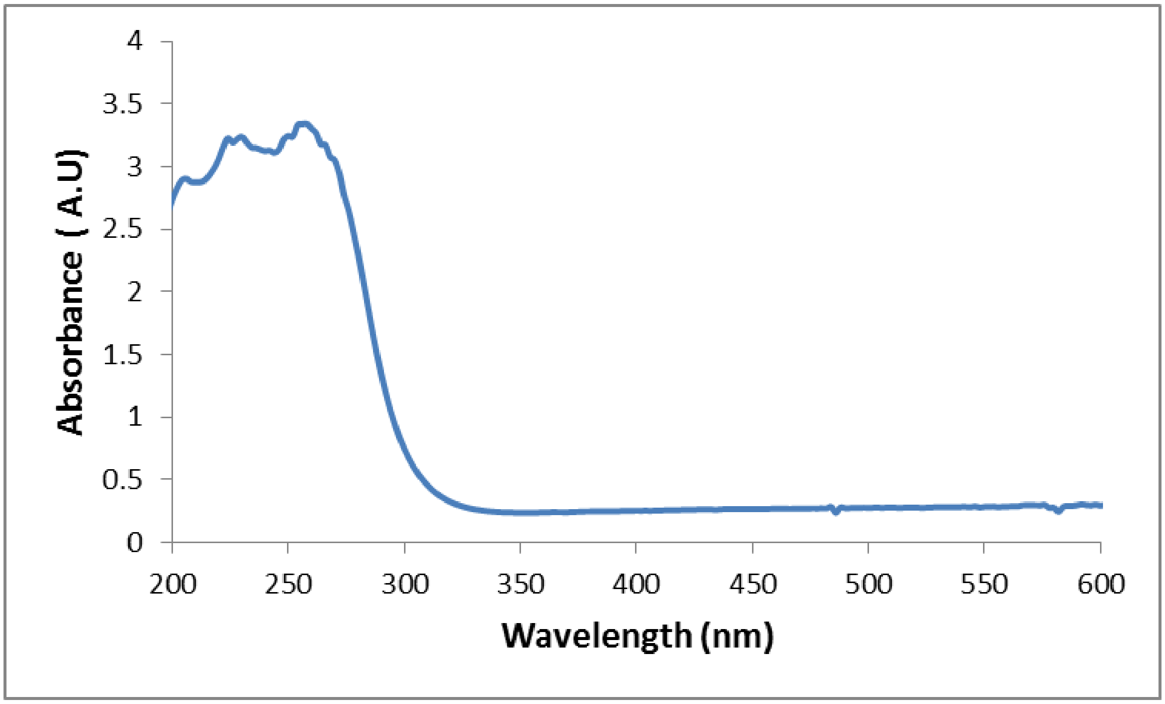

Figure 2-20. UV-Vis spectrum of glass reaction vial.

Because the reaction vial employed to date in degradation reactions absorbed the UV light necessary to create the radical species imperative for degradation, modifications were made to the procedure. The reaction vial used subsequently was made from quartz. To further analyze the photocatalytic ability of TiO_2 vs. CEES the catalyst was soaked prior to CEES and UV exposure to guarantee water is adsorbed in the surface and will result in radical production. 10 mg of TiO_2 nanofibers were soaked in 0.5 mL of deionized water for 1 h. Any excess water that was not absorbed by the catalyst was removed prior to addition of CEES. 0.105 mL of CEES was added to the top of the catalyst and immediately exposed to UV light or kept in the dark. Both light and dark experiments were carried out to compare the importance of UV irradiation to the degradation process.

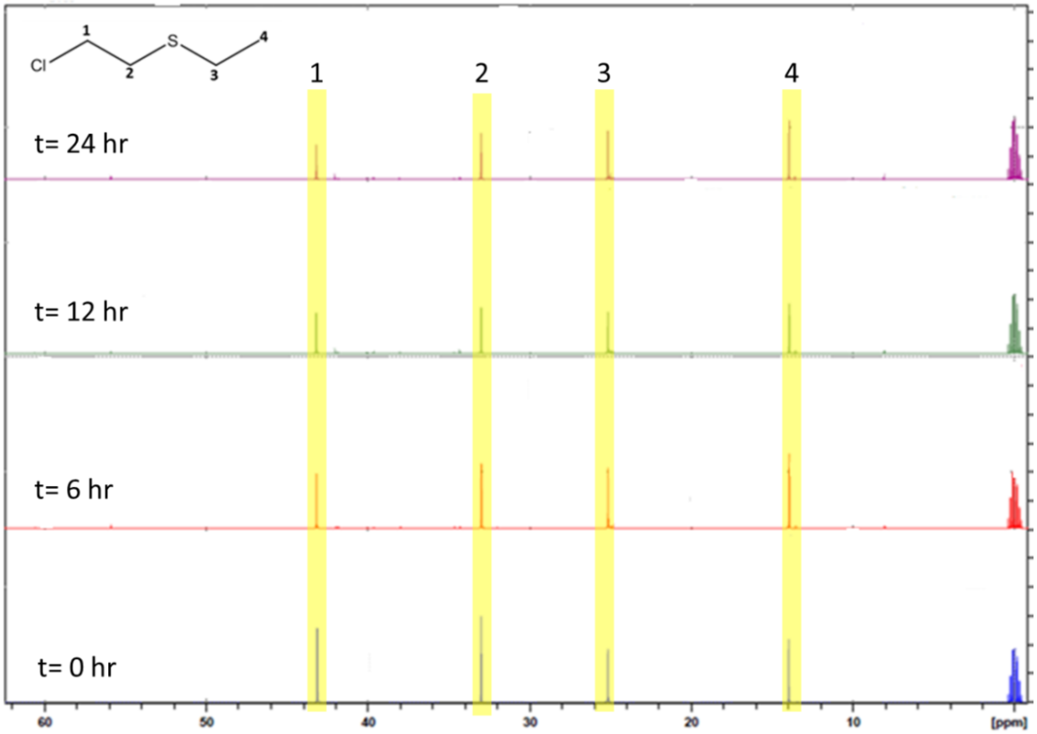

Figure 2-21. ^{13}C NMR- Solventless degradation of CEES with TiO_2 nanofibers in the dark

As shown in **Figure 2-21**, it was observed that even after 24 h of CEES exposure to TiO_2 the four characteristic singlets remain and possess approximately the same amount of intensity throughout. The experiment was then repeated under identical conditions, except in the presence if UV light. The premise was that the UV light would excite an electron from the valence band to the conduction band of the TiO_2, and atmospheric oxygen would react with the electron in the conduction band producing superoxide radicals, while the absorbed water would react the positive hole in the valence band resulting in hydroxyl radicals. The radicals are very reactive and responsible for the photodegradation of organic pollutants.

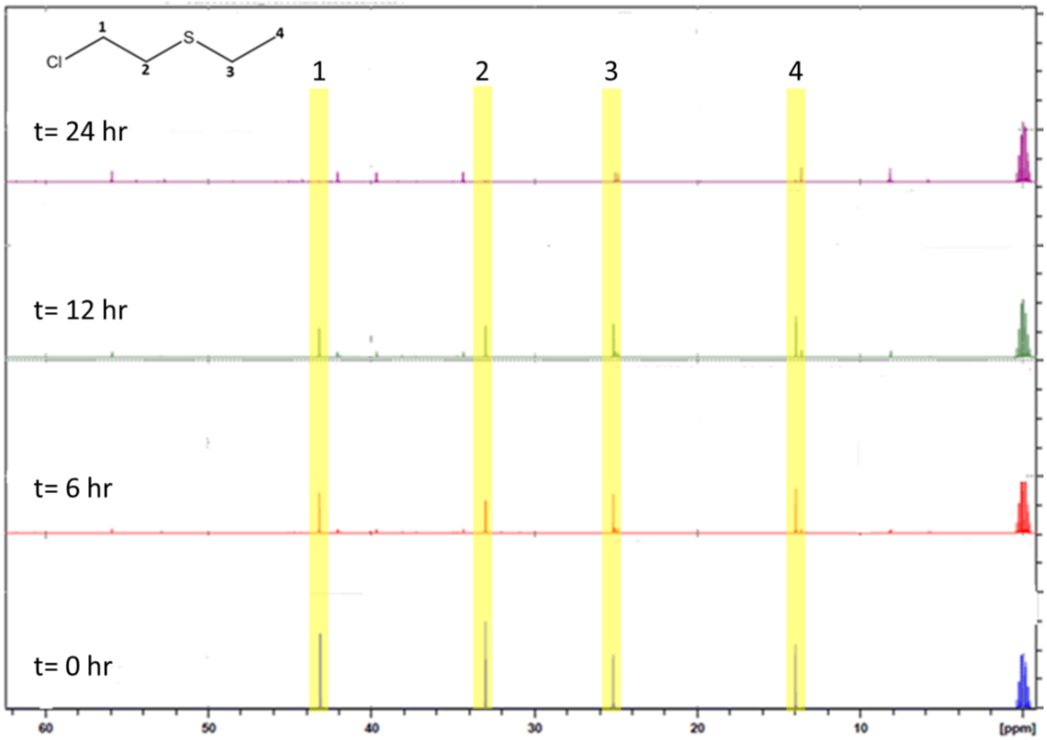

Figure 2-22. ^{13}C NMR- Solventless degradation of CEES with water saturated TiO_2 nanofibers under UV irradiation.

The catalyst was saturated with a small amount of water prior to addition of CEES. The absorbed water of the surface of the catalyst would produce hydroxyl radicals in the presence of UV irradiation, which in turn would promote the degradation of CEES. After 12 h in the CEES photodegradation with UV light, a small decrease in the intensity of the peaks is evident as well as the small formation of product peaks that were earlier described in the hydrolysis of CEES. After 24 h, the four characteristic singlets have disappeared and the product peaks are beginning to increase in intensity; **Figure 2-22**. The comparison of these degradation experiments in both light and dark conditions lead to the conclusion that of UV irradiation was necessary to initiate the photocatalytic ability of TiO_2. We were able to theorize from the results that the catalyst is aiding in the hydrolysis degradation reaction of CEES over 24 hours.

2.3.3 Photocatalytic Degradation of Dimethyl methylphosphonate

2.3.3.1 Hydrolysis study of Dimethyl methylphosphonate

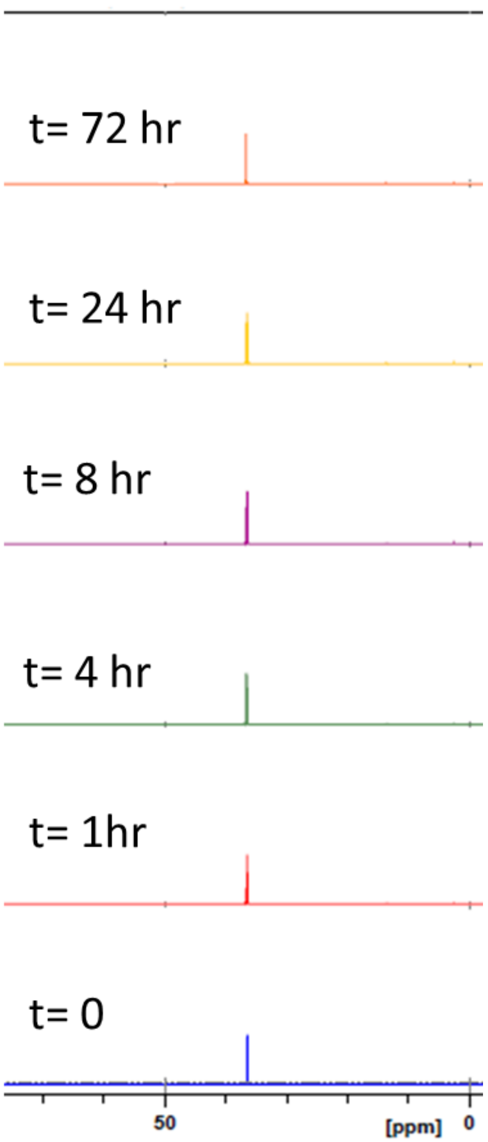

Figure 2-23. 31P NMR- Hydrolysis study of DMMP over 72 h.

DMMP is highly water stable, as can be seen by ^{31}P NMR analysis over a 72 h exposure to water as a control experiment. A 1 M aqueous solution of DMMP was prepared and stirred vigorously over the course of 72 h. At specific time intervals aliquots were extracted and analyzed via ^{31}P NMR. Over the duration of the experiment, the characteristic singlet at 37.7 ppm did not decrease in intensity, **Figure 2-23.** The results correlate well with literature reports regarding the hydrolysis of GD occurring at a slow rate under neutral conditions.[26]

2.3.3.2 Photodegradation of Dimethyl methylphosphonante with P25 Nanoparticles under UV Irradiation

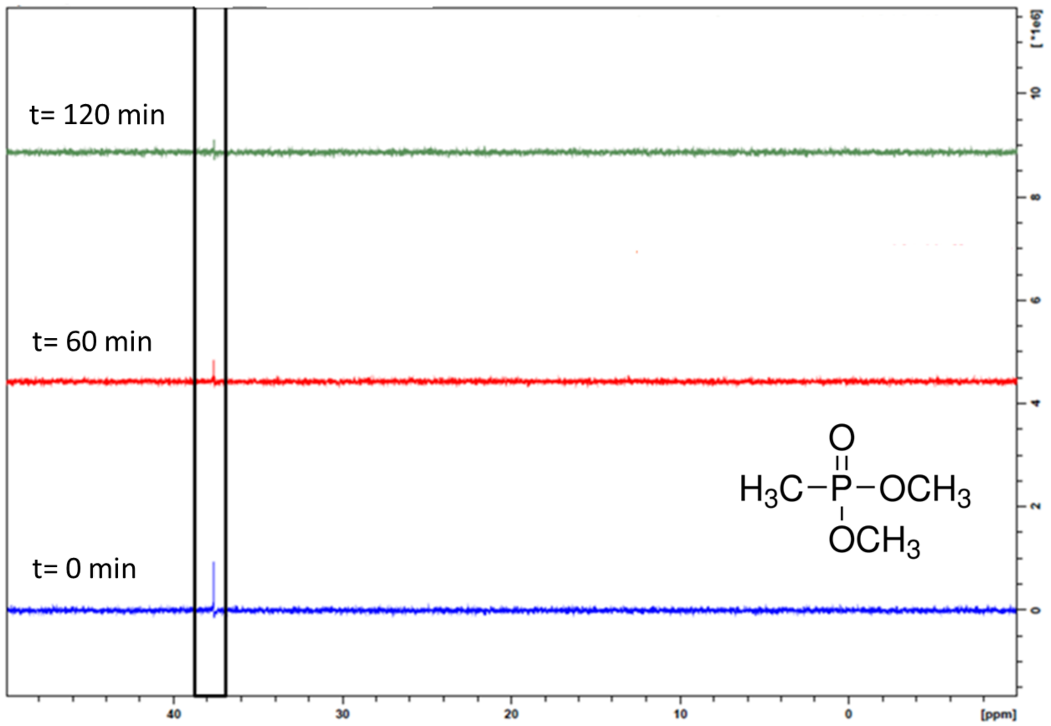

Figure 2-24. ^{31}P NMR- Photodegradation of DMMP with Degussa P25 Nanoparticles.

A 100 µM aqueous solution of DMMP was prepared, and 50 mg of P25 nanoparticles was added to the solution at which time the UV lamp was turned on. This solution was exposed to UV irradiation for 2 h, during which time aliquots were extracted and analyzed via ^{31}P NMR, **Figure 2-24.** Results are based on the intensity of the signature phosphorus peak at 37.7 ppm. It is evident that even after 2 h of irradiation, the presence of the singlet at 37.7 ppm remains; however the intensity of that peak has decreased over time. This signifies that some degradation has occurred, but DMMP is still present in solution even after the catalyst has had sufficient exposure to the irradiation to promote degradation.

2.3.3.3 Photodegradation of Dimethyl methylphosphonate with TiO_2 Nanofibers under UV Irradiation

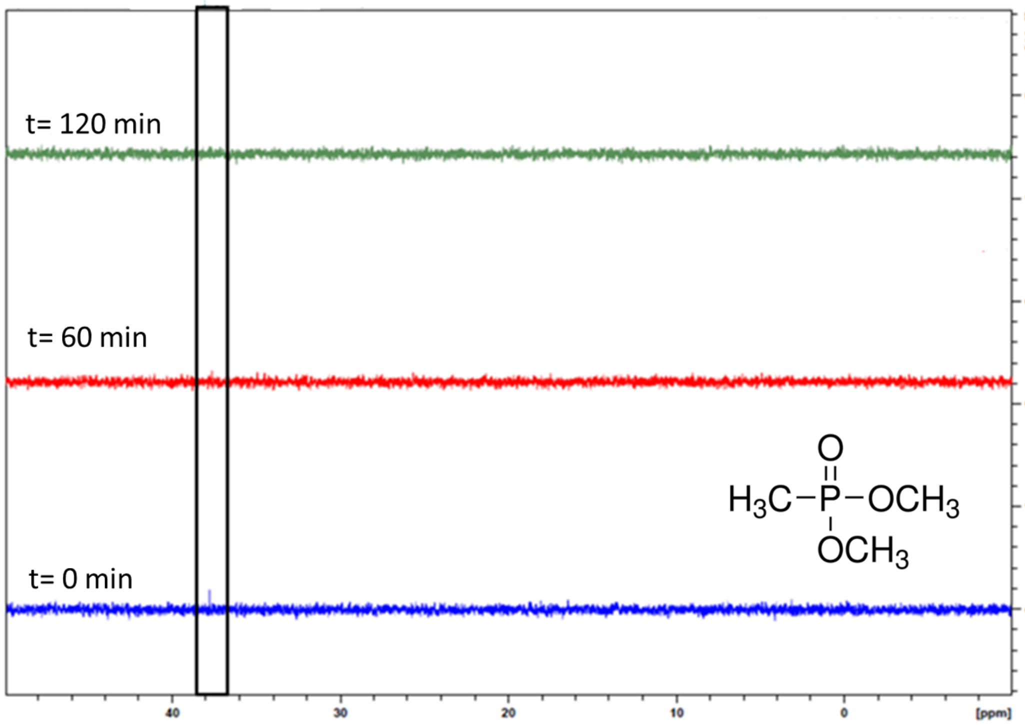

Figure 2-25. ^{31}P NMR- Photodegradation of DMMP with TiO_2 nanofibers

P25 nanofibers were seen to have little effect on DMMP under UV irradiation. The electrospun nanofibers were introduced to DMMP under identical reaction conditions to examine the influence of the nanofibers to degradation compared to nanoparticles. A 100 µM solution of DMMP was prepared and 50 mg of TiO_2 nanofibers was added to the solution, at which time the UV lamp was turned on. The solution was stirred continuously over the course of the experiment. After 2 h of exposure to UV irradiation in the presence of the TiO_2 nanofibers, the characteristic phosphorus peak at 37 ppm was no longer detectable, **Figure 2-25**. The disappearance of the phosphorus resonance is indicative of degradation of DMMP. The phosphorus atom is hypothesized to be bound to the catalyst, and then explains for the absence of peaks in the ^{31}P NMR.

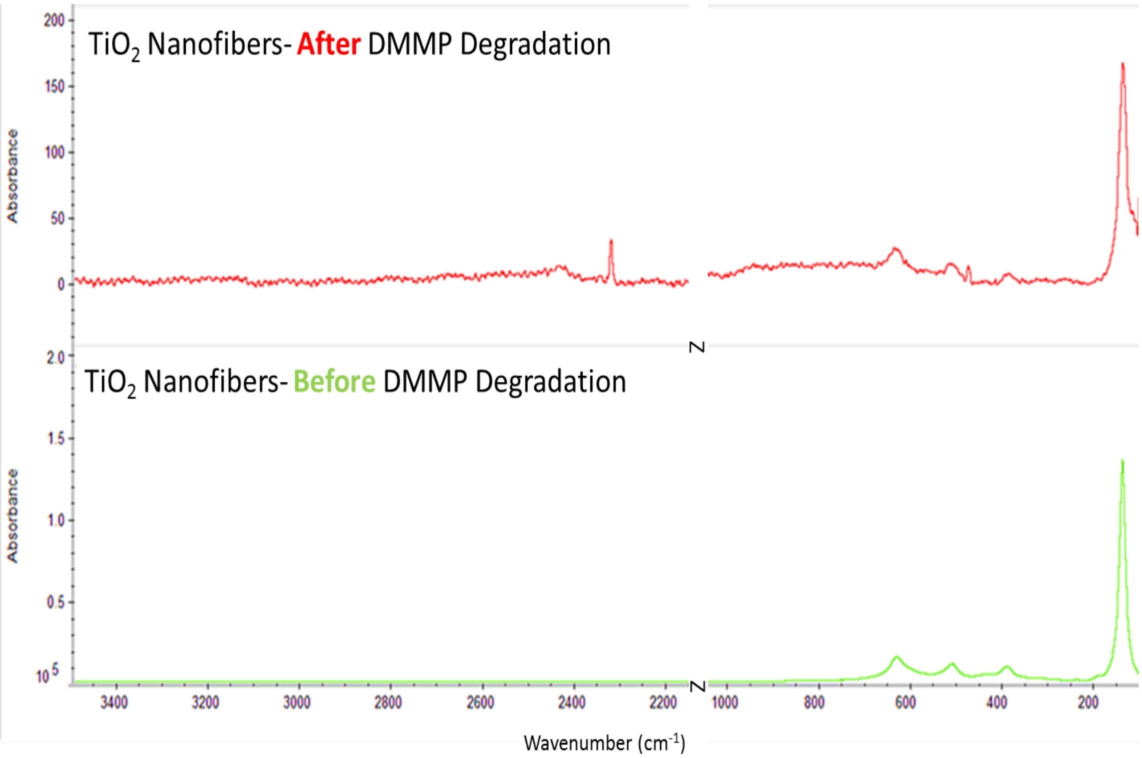

Figure 2-26. Raman spectrum of TiO_2 nanofibers before and after the photodegradation of DMMP.

Raman spectroscopy was utilized to attempt to determine the location of the phosphorus after the degradation of DMMP. Literature reports suggest that GD is reacting with Ti and can form titanophonates (Ti-O-Ti or Ti-O-P), due to the side reaction with water.[3,4] The resulting peak at 2325 cm^{-1} indicated a possible binding interaction between the phosphorus and titanium centers, **Figure 2-26**. Further analysis needs to be done to confirm this hypothesis.

2.3.3.4 Comparison of Photocatalytic Performance of Nanofibers v. Nanoparticles: The Role of Surface Area

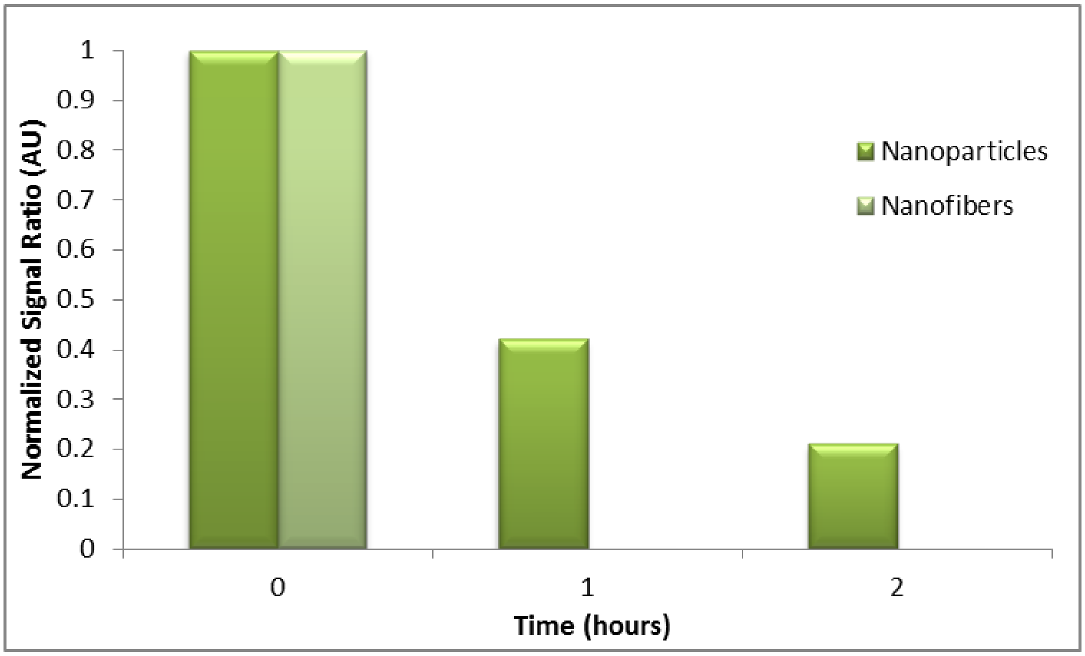

Figure 2-27. Bar graph depicting normalized signal ratio vs. time of DMMP degradation with both TiO_2 nanofibers and P25 nanoparticles

Surface area is thought to play a significant role in the decontamination process because the larger the surface area, the greater the opportunity for hydroxyl radicals to be formed, which is critical to decontamination. Alternatively, the highly porous nanofibers may allow for a larger interface between the pollutant and catalyst, as well as other contributing factors such as the crystal structure and charge transfer. For a given mass of catalyst, the nanofibers may present greater contact. Due to the disappearance of the phosphorus peak associated with degradation, it is suggested that the degraded phosphorus product is retained on the surface of TiO_2 or within the nanofiber. This result is crucial in proving the surface area of the catalyst is not a primary cause for degradation. The comparison of DMMP ^{31}P signal ratio of nanofibers and nanoparticles is shown in **Figure 2-27**.

2.4 Conclusions

TiO_2 nanofibers were successfully fabricated from a sol-gel solution, followed by electrospinning and annealing/calcination with a thermal treatment under atmospheric conditions. Nanofiborous TiO_2 possesses a variety of valuable attributes as stated above in the mitigation of SCWAs. The synthesized fibers were used directly in photocatalytic degradation of CEES and DMMP, and were found to promote enhanced rates of degradation.

Photocatalytic and hydrolytic degradations of CEES were found to enhance the rate of hydrolysis of SCWAs. A better understanding was gained in studying the hydrolysis of CEES using ^{13}C NMR. It was concluded that the presence of a nucleophilic, polar solvent was necessary to enhance the degradation process. This was proven by the saturation of the TiO_2 nanofibers with water prior to exposure to the target pollutant, and results showed an overall increased the degradation of CEES under UV irradiation.

Photocatalytic degradations of DMMP were designed to demonstrate the role of surface area in the degradation process. The comparison of nanofibers vs nanoparticles supports the conclusion that surface area is a less critical factor in the degradation of SCWAs than is surface area, which has been previously examined. This could be attributed to the folded porous morphology of the nanofibers, which allows for more points of contact between the catalyst, $TiO_{2,}$ and the pollutant being examined, which in this case was DMMP. Further possible explanations as to why the nanofibers have an enhanced performance over the nanoparticles include an increase in the total number of active sites promoting a kinetic path, or the nanofibers have different energy in the active sites compared to the nanoparticles resulting in a thermodynamic path.

2.5 References

1. Paz, Y.; Luo, Z.; Rabenberg, L.; Heller, A., Photooxidative self-cleaning transparent titanium dioxide films on glass. *Journal of Materials Research* **1995,** *10* (11), 2842-2848.

2. Paz, Y.; Heller, A., Photo-oxidatively self-cleaning transparent titanium dioxide films on soda lime glass: The deleterious effect of sodium contamination and its prevention. *Journal of Materials Research* **1997,** *12* (10), 2759-2766.

3. Wagner, G. W.; Chen, Q.; Wu, Y., Reactions of VX, GD, and HD with Nanotubular Titania. *The Journal of Physical Chemistry C* **2008,** *112* (31), 11901-11906.

4. Wagner, G. W.; Peterson, G. W.; Mahle, J. J., Effect of Adsorbed Water and Surface Hydroxyls on the Hydrolysis of VX, GD, and HD on Titania Materials: The Development of Self-Decontaminating Paints. *Industrial & Engineering Chemistry Research* **2012,** *51* (9), 3598-3603.

5. Wagner, G. W.; Procell, L. R.; Munavalli, S., 27Al, 47,49Ti, 31P, and 13C MAS NMR Study of VX, GD, and HD Reactions with Nanosize Al2O3, Conventional Al2O3 and TiO2, and Aluminum and Titanium Metal. *The Journal of Physical Chemistry C* **2007,** *111* (47), 17564-17569.

6. O'Shea, K. E.; Beightol, S.; Garcia, I.; Aguilar, M.; Kalen, D. V.; Cooper, W. J., Photocatalytic decomposition of organophosphonates in irradiated TiO2 suspensions. *Journal of Photochemistry and Photobiology A: Chemistry* **1997,** *107* (1–3), 221-226.

7. Smith, B. M., Catalytic methods for the destruction of chemical warfare agents under ambient conditions. *Chemical Society Reviews* **2008,** *37* (3), 470-478.

8. Schneider, J.; Matsuoka, M.; Takeuchi, M.; Zhang, J.; Horiuchi, Y.; Anpo, M.; Bahnemann, D. W., Understanding TiO2 Photocatalysis: Mechanisms and Materials. *Chemical Reviews* **2014,** *114* (19), 9919-9986.

9. Riegel, G.; Bolton, J. R., Photocatalytic Efficiency Variability in TiO2 Particles. *The Journal of Physical Chemistry* **1995,** *99* (12), 4215-4224.

10. Tian, G.; Fu, H.; Jing, L.; Xin, B.; Pan, K., Preparation and Characterization of Stable Biphase TiO2 Photocatalyst with High Crystallinity, Large Surface Area, and Enhanced Photoactivity. *The Journal of Physical Chemistry C* **2008,** *112* (8), 3083-3089.

11. Obuya, E. A.; Harrigan, W.; Andala, D. M.; Lippens, J.; Keane, T. C.; Jones Jr, W. E., Photodeposited Pd nanoparticle catalysts supported on photoactivated TiO2 nanofibers. *Journal of Molecular Catalysis A: Chemical* **2011,** *340* (1–2), 89-98.

12. Obuya, E. A.; Joshi, P. C.; Gray, T. A.; Keane, T. C.; Jones, W. E., Jr., Application of Pt.TiO2 nanofibers in photosensitized degradation of rhodamine B. *International Journal of Chemistry* **2014,** *6* (1), 1-16.

13. Liu, J.; McCarthy, D. L.; Cowan, M. J.; Obuya, E. A.; DeCoste, J. B.; Skorenko, K. H.; Tong, L.; Boyer, S. M.; Bernier, W. E.; Jones Jr, W. E., Photocatalytic activity of

TiO2 polycrystalline sub-micron fibers with variable rutile fraction. *Applied Catalysis B: Environmental* **2016,** *187*, 154-162.

14. Choi, S. K.; Kim, S.; Lim, S. K.; Park, H., Photocatalytic Comparison of TiO2 Nanoparticles and Electrospun TiO2 Nanofibers: Effects of Mesoporosity and Interparticle Charge Transfer. *The Journal of Physical Chemistry C* **2010,** *114* (39), 16475-16480.

15. Antonietta Zoroddu, M.; Medici, S.; Ledda, A.; Marina Nurchi, V.; I. Lachowicz, J.; Peana, M., Toxicity of Nanoparticles. *Current Medicinal Chemistry* **2014,** *21* (33), 3837-3853.

16. Dai, Y.; Cobley, C. M.; Zeng, J.; Sun, Y.; Xia, Y., Synthesis of Anatase TiO2 Nanocrystals with Exposed {001} Facets. *Nano Letters* **2009,** *9* (6), 2455-2459.

17. Nagamine, S.; Tanaka, Y.; Masahiro, O., Fabrication of Hollow TiO2 Fibers Templated by Electrospun Aqueous Poly(ethylene oxide) (PEO) Solution. *Chemistry Letters* **2009,** *38* (3), 258-259.

18. Wu, M.-C.; Chan, S.-H.; Lin, T.-H., Fabrication and photocatalytic performance of electrospun PVA/silk/TiO2 nanocomposite textile. *Functional Materials Letters* **2015,** *08* (03), 1540013.

19. Lee, Y.-I.; Lee, J.-S.; Park, E.-S.; Jang, D.-H.; Lee, J.-E.; Kim, K.; Myung, N. V.; Choa, Y.-H., Effect of Calcination Temperature on the Photocatalytic Properties of Electrospun TiO2 Nanofibers. *Journal of Nanoscience and Nanotechnology* **2014,** *14* (10), 8005-8009.

20. Reneker, D.; Chun, I., Nanometre diameter fibres of polymer, produced by electrospinning. *Nanotechnology* **2003,** *7* (3), 216.

21. Dong, H.; Nyame, V.; MacDiarmid, A. G.; Jones; Jr., W. E., Polyaniline/poly(methyl methacrylate) coaxial fibers: The fabrication and effects of the solution properties on the morphology of electrospun core fibers. *Journal of Polymer Science Part B: Polymer Physics* **2004,** *42* (21), 3934-3942.

22. He, J.-H.; Wu, Y.; Zuo, W.-W., Critical length of straight jet in electrospinning. *Polymer* **2005,** *46* (26), 12637-12640.

23. Mahshid, S.; Askari, M.; Ghamsari, M. S., Synthesis of TiO2 nanoparticles by hydrolysis and peptization of titanium isopropoxide solution. *Journal of Materials Processing Technology* **2007,** *189* (1–3), 296-300.

24. Ohtani, B.; Prieto-Mahaney, O. O.; Li, D.; Abe, R., What is Degussa (Evonik) P25? Crystalline composition analysis, reconstruction from isolated pure particles and photocatalytic activity test. *Journal of Photochemistry and Photobiology A: Chemistry* **2010,** *216* (2–3), 179-182.

25. Bae, S. Y.; Winemiller, M. D., Mechanistic Insights into the Hydrolysis of 2-Chloroethyl Ethyl Sulfide: The Expanded Roles of Sulfonium Salts. *The Journal of Organic Chemistry* **2013,** *78* (13), 6457-6470.

26. Munro, N. B.; Talmage, S. S.; Griffin, G. D.; Waters, L. C.; Watson, A. P.; King, J. F.; Hauschild, V., The sources, fate, and toxicity of chemical warfare agent degradation products. *Environmental Health Perspectives* **1999,** *107* (12), 933-974.

CHAPTER 3: Composite Nanofiber Blends: The Introduction of Metal-Organic Frameworks to Enhance Degradation

3.1 Introduction

The use of TiO_2 as a catalyst for degradation of organic toxins has been well documented in the literature.[1] Commonly titania is seen as spherical nanoparticles, new advances in catalytic performance have led to altering the shape and surface morphology of the catalyst. TiO_2 nanofibers represent an alternative materials approach to conventional nanoparticle composites for use in photocatalytic degradation.[2] The one-dimensional morphology of TiO_2 nanofibers is preferred, as they exhibit excellent mobility of charge carriers, high surface area, and the existence of pores leading to enhanced accessibility.[3] The use of nanotubular titania against CWAs has been documented in the literature with success in decontamination of agents such as HD, VX and GD.[4,5 ,6]

Electrospinning, a non-mechanical electrostatic process, produces nanometer to micrometer width fiber using an electrostatically driven jet of polymer solution.[7,8,9] Electrospun metal oxide nanofibers have been used in a variety of applications including photocatalysis[10], sensing[11], and solar cells.[12] Recent results have demonstrated that composite polymer precursor materials used in the fabrication of electrospun TiO_2 nanofibers have catalytic ability in the degradation of simulated chemical warfare agents (SWCAs).

Electrospun nanofibers of polymethyl methacrylate (PMMA) and titanium triisopropoxide (TTiP) were found to possess catalytic properties when introduced to methyl paraoxon, a SCWA. In addition to the photocatalytic advantages of these fibers, increased flexibility and durability were observed compared to electrospun TiO_2 nanofibers. The resulting fibers would also be more compatible with low temperature processing of multifunctional materials, including MOFs and sensors.

MOFs are hybrid compounds consisting of an inorganic metal node coordinated to an organic ligand. The inorganic and organic components can be altered and functionalized leading to a variety of chemical structures, all potentially tunable to a specific application including catalysis[13], gas storage[14], separation[15] and molecular sensing.[16] Modification of the secondary building unit (SBU) consisting of a polydentate organic ligand can result in better reactivity and selectivity of the MOF to CWAs. Further engineering could lead to the fabrication of MOFs into nano-powdered or nanofibrous forms for application in textiles, filtration, and coatings.

Originally MOFs were constructed with the intent to be used as a heterogeneous catalyst.[17] The UiO-family of MOFs became increasingly significant to catalysis applications due to its chemical and physical stability.[18,19] MOFs are excellent candidates for the destruction of chemical warfare agents which has been demonstrated in the literature. Their properties of exceptionally large surface area, porosity, pore size and variety of functionality[20] as well as their robustness are well suited for the harsh conditions caused by CWAs.[21] UiO-66 is a zirconium based MOF comprised of Zr_6O_6 SBU connected to a 12 bidendate terephthalic acid ligand. A reaction scheme of UiO-66 can be seen in **Figure 3-1**. The Zr_6O_6 SBU provides catalytic ability and increased chemical stability compared to other MOFs, as well as the versatility of Zr based MOFs with CWAs.[22]

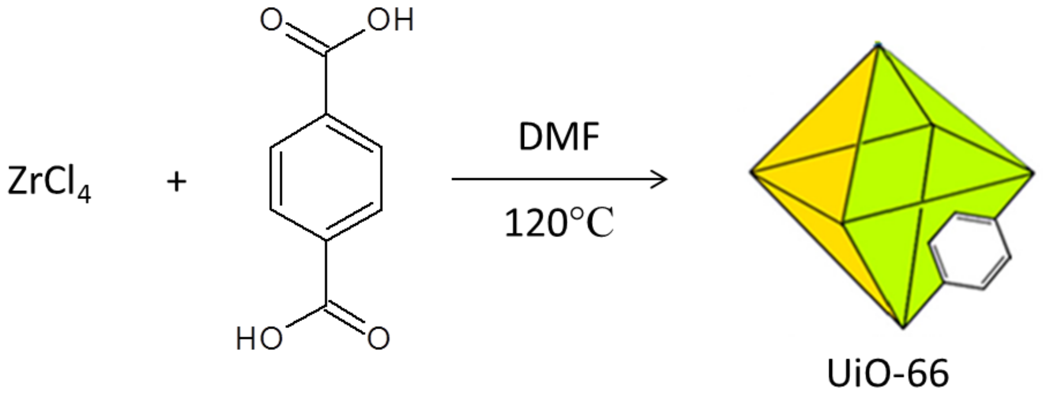

Figure 3-1. Reaction scheme of the formation of UiO-66.

Multiple Zr-OH-Zr moieties found in UiO-66 can mimic the Lewis acid active sites found in G-agents, leading to binding followed by hydrolysis.[1] UiO-66 has shown the capability to carry out catalytic hydrolysis which has been seen in the degradation of a phosphate containing simulated chemical warfare agents demonstrating impressive half-lives.[23] The UiO-66 series has been found to behave as a semiconductor when exposed to light. This in turn makes them a unique and novel material for light harvesting and photo-induced catalysis.[24] The addition of an amino group to the UiO-66 produces multiple advantages including increased functionality[25]and increased absorption capacity.[20] The amino group can shift the photo-absorption of the UiO-66 from the UV to the visible region, making it an excellent candidate for solar induced photocatalysis.[26] A reaction scheme for the formation of UiO-66 NH_2 can be seen in **Figure 3-2**.

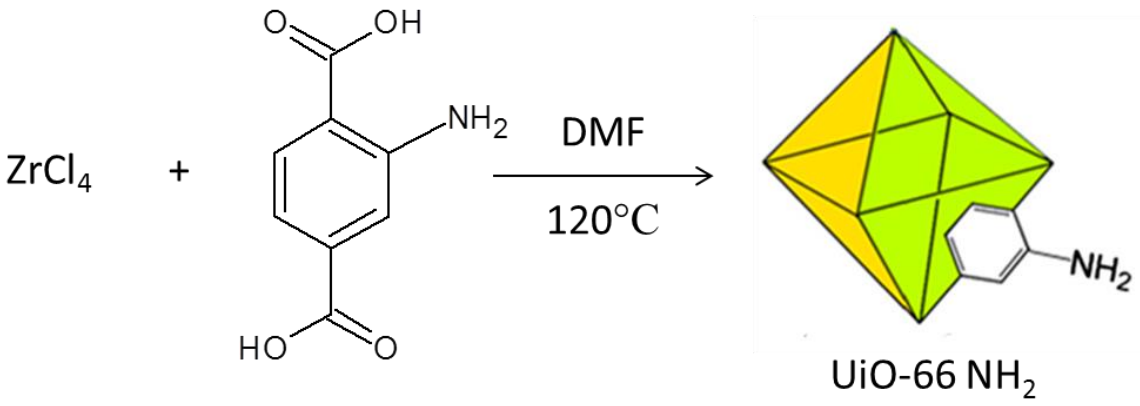

Figure 3-2. Reaction scheme for the formation of UiO-66 NH_2

Organophosphates are among the world's most deadly toxins. Currently employed as chemical warfare agents, phosphate esters have the ability to rapidly inhibit acetylcholinesterase, a critical enzyme for nerve synapses to function properly which ultimately leads to death.[27] Destruction of these CWAs is imperative. Heterogeneous catalysis by nanostructured materials has proven to be suitable method for degradation of biopharmaceutical toxic organic pollutants[28] and may also be viable for degradation of CWAs. Curently available CWA degradation techniques include incineration, water hydrolysis followed by biotreatment, and water hydrolysis followed by supercritical water oxidation.[29,30] Drawbacks to these techniques include the selectivity of the analyte, degradation of the enzyme over extended treatment time and lack of robustness for practical applications. Transitioning to a more effective approach using heterogeneous catalysis by nanostructured materials, solid catalysts including titania and MOFs have demonstrated a means to effectively destroy CWAs.[4]

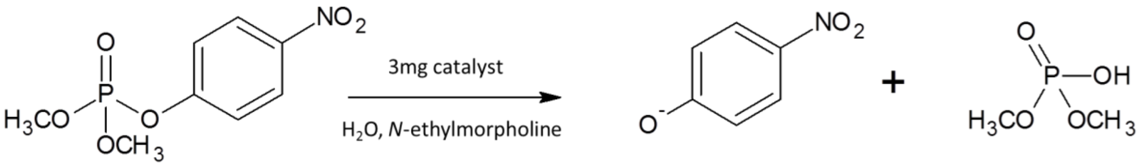

Figure 3-3. Hydrolysis mechanism of methyl paraoxon.

In this chapter, the synthesis and fabrication of UiO-66 and UiO-66 NH_2 polymer fiber composites and their characterization are discussed. This focus includes the encouraging results of blended electrospun UiO-66 in a PMMA/TTiP fibrous matrix producing conversions and half-lives commensurate with those previously observed for the hydrolysis of methyl paraoxon (**Figure 3-3**), by MOF powders.[23,31,32] The results are compared directly with varying compositions of nanofibers, both with and without UiO-66, to demonstrate the need for the fibrous matrix. Degradation reactions are then repeated with composite polymer fibers both with and without UiO-66 NH_2. Samples were subjected to dark, ultraviolet and visible light conditions. The results are compared with materials containing UiO-66 to determine if the addition of a functional group to the MOF will enhance the efficiency.

3.2 Experimental

3.2.1 Materials

Polymethylmethacrylate (PMMA) (M_w960,000), titanium (IV) isopropoxide (TTiP), N,N-dimethylformamide (DMF), chloroform and ***O*-(4-nitrophenyl) phosphate** (methyl paraoxon, DMNP) (M_w247.14) 4-ethylmorpholine (M_w115.17),was purchased from Sigma Aldrich and used without any further purification. UiO-66 (Zr) and UiO-66 NH_2 were provided by Edgewood Chemical Biological Center.

3.2.2 Synthesis of Metal-Organic Framework

3.2.2.1 Synthesis of UiO-66 and UiO-66 NH_2

An equal molar mixture of $ZrCl_4$ (19 mmol, 4.42 g) and terephthalic acid (UiO-66, 19 mmol, 3.15 g) or 2-amino terephthalic acid (UiO-66-NH_2, 19 mmol, 3.44 g) were mixed at room temperature in approximately 700 mL of DMF. The mixture was split into two 500 mL jars and heated at 120 °C for 24 h. Each solution was cooled to room temperate, the solvent was decanted, the resulting MOFs were washed with DMF (3 X 50 mL), and the MOFs from the two jars were combined. The resulting MOFs were rinsed with 50 mL of methanol 4 times over 3 days and then activated under vacuum at 150 °C.[33]

3.2.3 Electrospinning of Composite Polymer Fibers

MOF/polymer composite fibers were fabricated using a sol gel synthesis and electrospinning. A sol gel solution in a 1:2 ratio of PMMA to TTiP was prepared in a 1:1 ratio of chloroform and N,N-dimethylformamide. Here 320 mg of PMMA was dissolved in 2 mL of chloroform and allowed to stir until the polymer was fully dissolved. 0.67 mL of TTiP was added dropwise to the polymer solution and allowed to stir for an additional 30 min, at which time 2 mL of DMF was added to the solution to increase the dielectric constant and stirred for an additional 2 h. 30 min prior to electrospinning, 5 wt% of UiO-66 or UiO-66 NH_2 was added and dispersed in the sol gel solution.

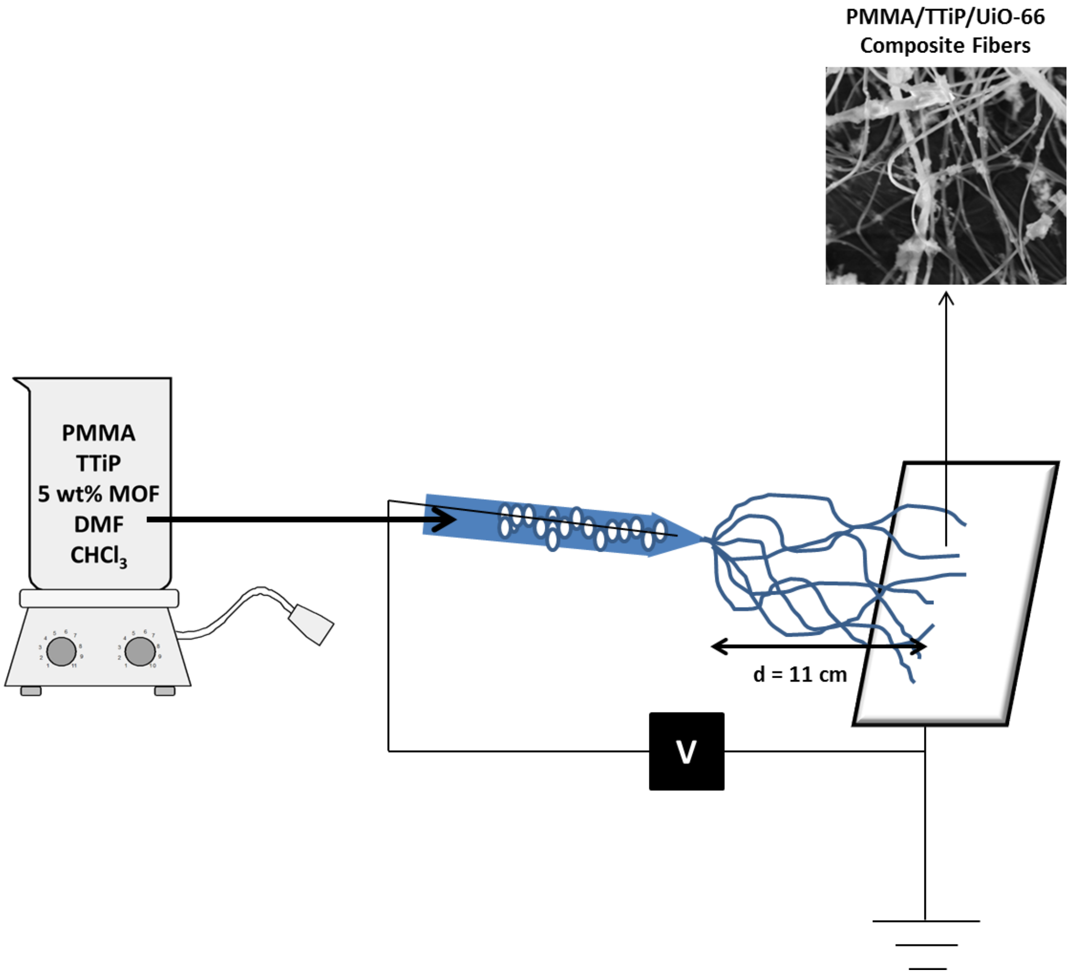

Figure 3-4. Schematic figure of electrospinning apparatus used to fabricate PMMA/TTiP/MOF composite fibers.

A Spellman SL 30 generator was used to apply 25kV/cm across the sol gel polymer solution, resulting in the deposition of nanofibers on the electrically charged collector. A schematic of the electrospinning apparatus can be seen in **Figure 3-4**. The composite nanofibers are left in ambient conditions to allow for hydrolysis of the TTiP to $Ti(OH)_{4,}$ and then further condensation over time to amorphous TiO_2.[34]

3.2.4 Characterization Methods

A Spellman SL 30 generator was used to apply a high voltage across the copper wire to create a high electrical potential attaching to the collector. Photodegradations used an Oriel 66001 UV lamp with Oriel 68805 40-200 Watt universal Arc lamp power supply, which covers the entire ultra-violet, 100- 400 nm range. UV-Visible analysis of the aliquot was performed on an 8452A Hewlett Packard Diode Array spectrophotometer with the wavelength from 190 to 820 nm to characterize the absorption spectrum of each aliquot to determine the concentration of the product formation. The morphological and structural characteristics of the nanofibers and nanoparticles were measured by field emission scanning electron microscopy (FESEM, Supra 55 VP from Zeiss equipped with an EDAX energy dispersive X-ray spectroscopy detector), and X-ray diffraction (XRD, PANalytical's X'Pert PRO Materials Research Diffractometer with Cu Kα radiation (λ = 1.5418 Å)), respectively. Transmission electron microscopy (TEM) images were obtained using a JEOL 2010 FETEM instrument. The TEM samples were dispersed in EtOH by sonication and the resulting solution were placed on a lacey carbon grid, which was left in air to evaporate the solvent. Nitrogen adsorption isotherms were measured for MOF/poylmer nanofibers using a Micromeritics TriStar 3000 analyzer at 77 K. Prior to analysis, each material was out gassed overnight at 50 °C under a flow of dry nitrogen.

Brunauer-Emmett-Teller (BET) modeling was performed to obtain the specific surface areas (m^2/g). ATR-FTIR measurements were done on a Bruker Tensor 27 FTIR with a Bruker Platinum ATR accessory equipped with a single reflection diamond crystal.

3.2.5 Degradation Procedure

3.2.5.1 Methyl Paraoxon Testing

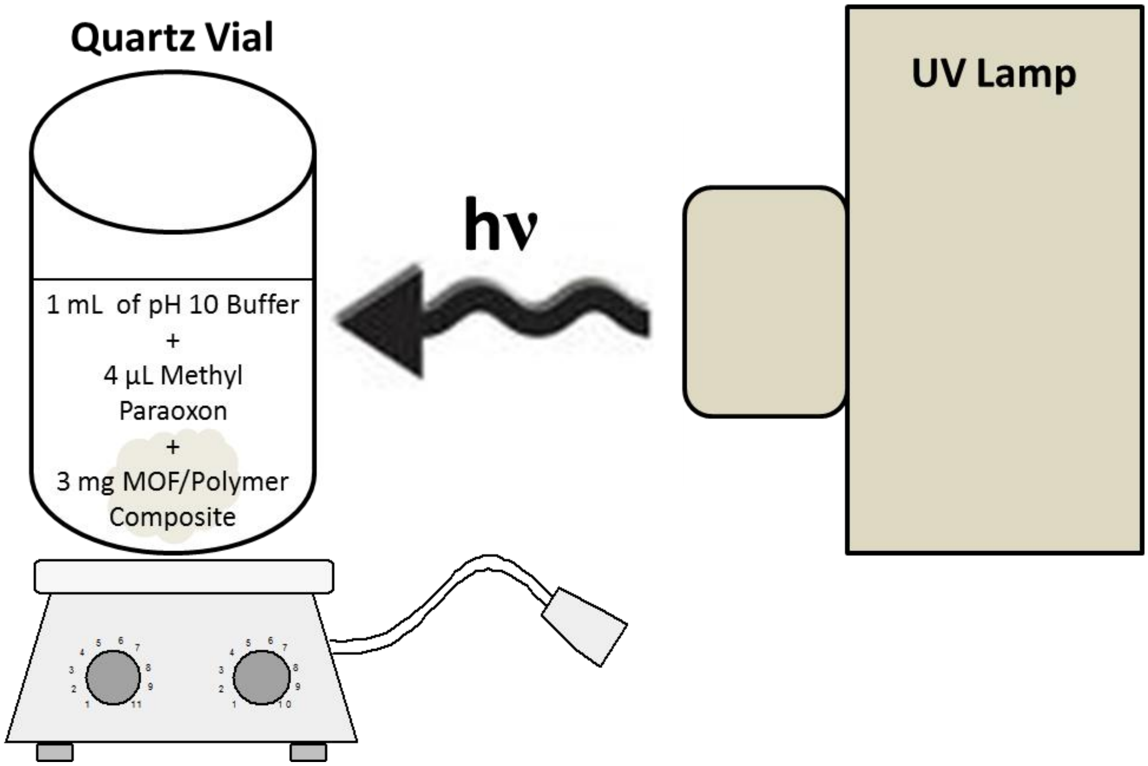

Figure 3-5. Reaction set-up for degradation of methyl paraoxon with MOF/polymer composite fibers.

All degradation experiments were carried out at room temperature. A 3 mg solid sample containing 5 wt% MOF/polymer composite fibers were introduced to an aqueous solution of N-ethyl morpholine (1 mL). The mixture was continuously stirred over the course of the experiment (2 h). To the dispersed suspension, 4 μL of methyl paraoxon (5.2 mg, 0.021 mmol) was introduced to the solution. Reactions were performed both with and without UV irradiation for comparison. At this point 10 μL aliquots were extracted at over 120 min. Aliquots were diluted to 5 mL with 0.45 M aqueous N-ethylmorpholine and measured using UV-Vis spectroscopy. P- nitrophenoxide was monitored via UV-Vis due to its absorbance at 407 nm. Standard control reactions were performed under the same conditions.

3.3 Results and Discussion

3.3.1 Characterization of MOF/polymer Catalyst

MOF/polymer composite fibers were fabricated using a sol gel synthesis and electrospinning as aforementioned. A sol gel solution in a 1:2 ratio of PMMA to TTiP was prepared in a 1:1 ratio of chloroform and N,N-dimethylformamide and 5wt% of MOF was added to the solution just prior to electrospinning. A high voltage was applied to the sol gel solution, creating a high electrical potential attaching to the collector where a fiborous mat was produced.

3.3.1.1 Polymer Composite Fibers Containing UiO-66

3.3.1.1.1 Scanning Electron Microscopy and Tunneling Electron Microscopy

Electrospun nanofibers were analyzed by Scanning Electron Microscopy (SEM) it can be seen in **Figure 3-6** the PMMA/TTiP nanofibers (**Figure 3-6 a**) have a folded/wrinkled surface morphology with consistent lengths and diameters throughout the sample. Addition of UiO-66 to the nanofiber led the diameter of the fiber to decrease drastically as well as a visible transformation in the surface morphology of the fibers. PMMA/TTiP/UiO-66 is shown from SEM (**Figure 3-6 b**) to have an average diameter of 750 nm. Samples containing only PMMA and UiO-66 also possessed a large variation in diameter throughout the sample. The fibers still retained a folded surface morphology without TTiP however the fibers seem more random and agglomerated as well as smaller in diameter. The PMMA/UiO-66 fibers bore an average diameter was determined to be approximately 625 nm. The fibers became wiry in nature with agglomerates of what were determined to be UiO-66.

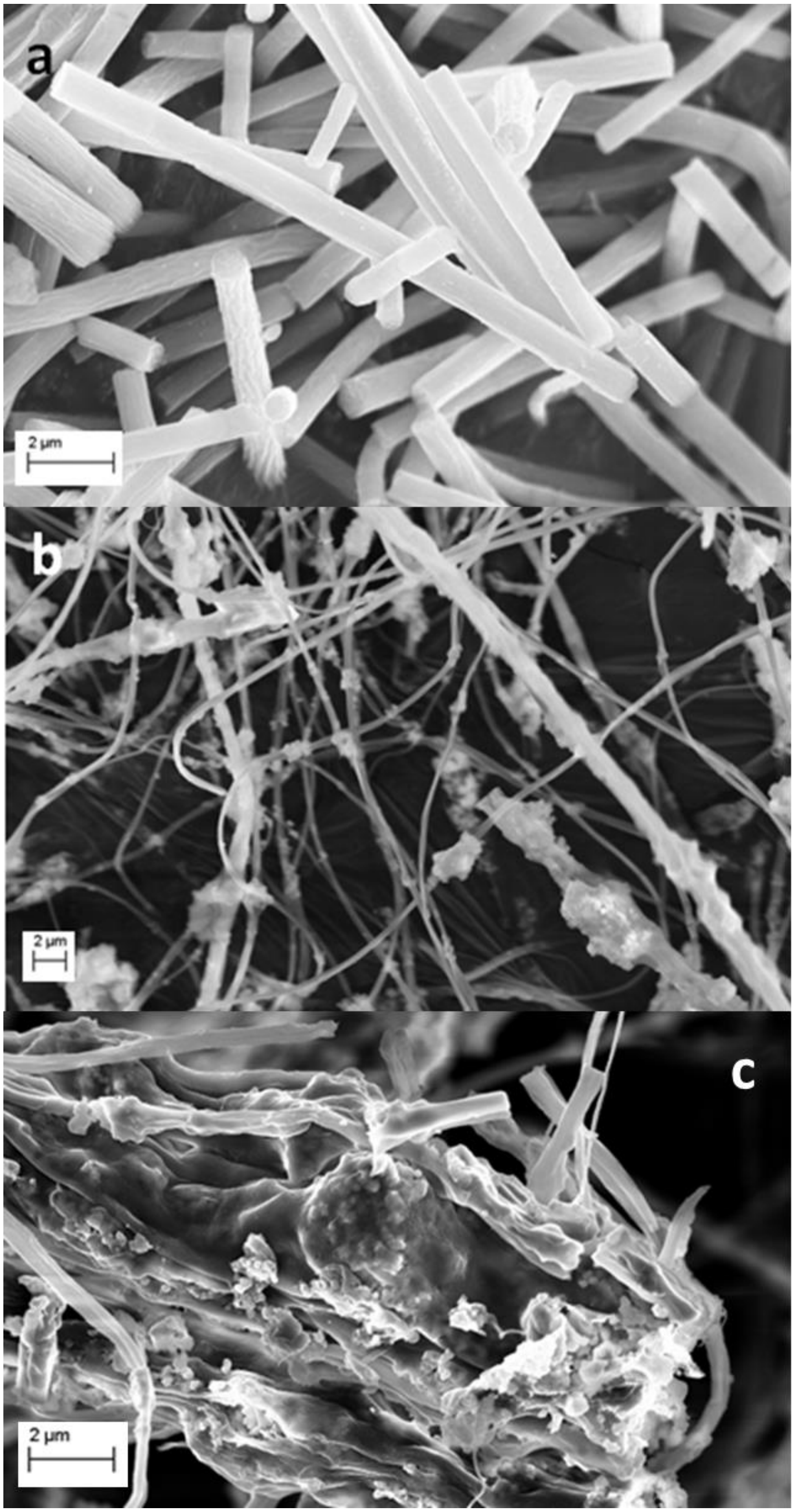

Figure 3-6. Scanning electron microscopy imaging of (a) PMMA/TTiP composite fibers and (b) PMMA/TTiP/UiO-66 composite fibers (c) PMMA/UiO-66

Further investigation of the fibers by TEM as shown in **Figure 3-7** reveals that UiO-66 is not decorated solely on the surface of the nanofiber, but in fact a small layer of PMMA/TTiP wraps around the MOF, embedding it within the fiber itself. It is clear the MOF alone is cube shaped (b) and upon electrospinning the precursors, PMMA and TTiP the structural morphology of the MOF is maintained (a).

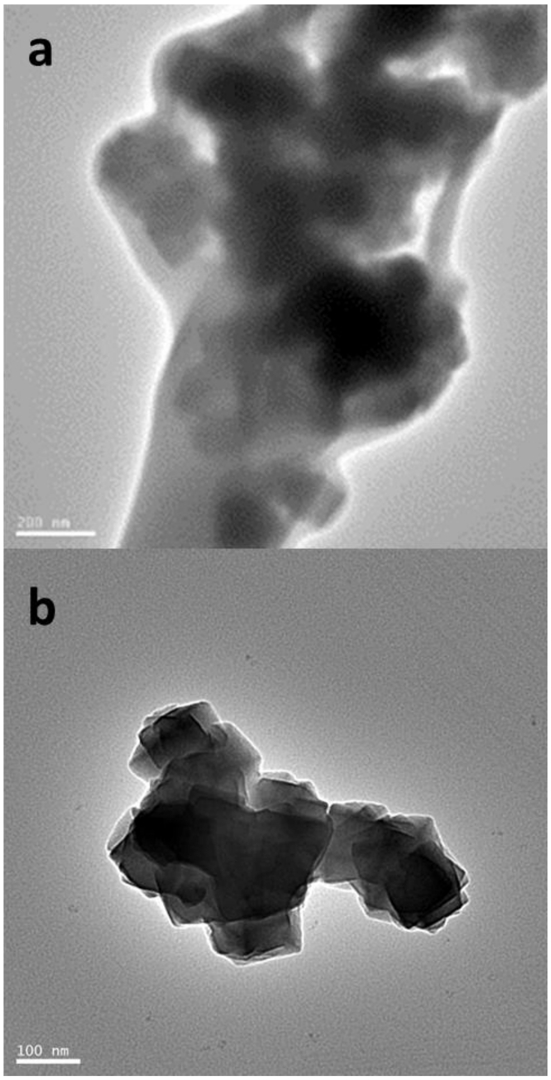

Figure 3-7. Transmission electron microscopy imaging (a) PMMA/TTiP/UiO-66 composite fibers and (b) UiO-66.

3.3.1.1.2 X-Ray Diffraction and Attenuated Total Reflectance Infrared Spectroscopy

UiO-66 displays many characteristic XRD peaks, but two are indicative of UiO-66 at 2Ө value of 7.34° and 8.48° , which are still present upon electrospinning UiO-66 with PMMA and TTiP seen in **Figure 3-8**.[35] Both prior to the addition of the sol gel and after electrospinning the intensity of those characteristic peaks remained constant.

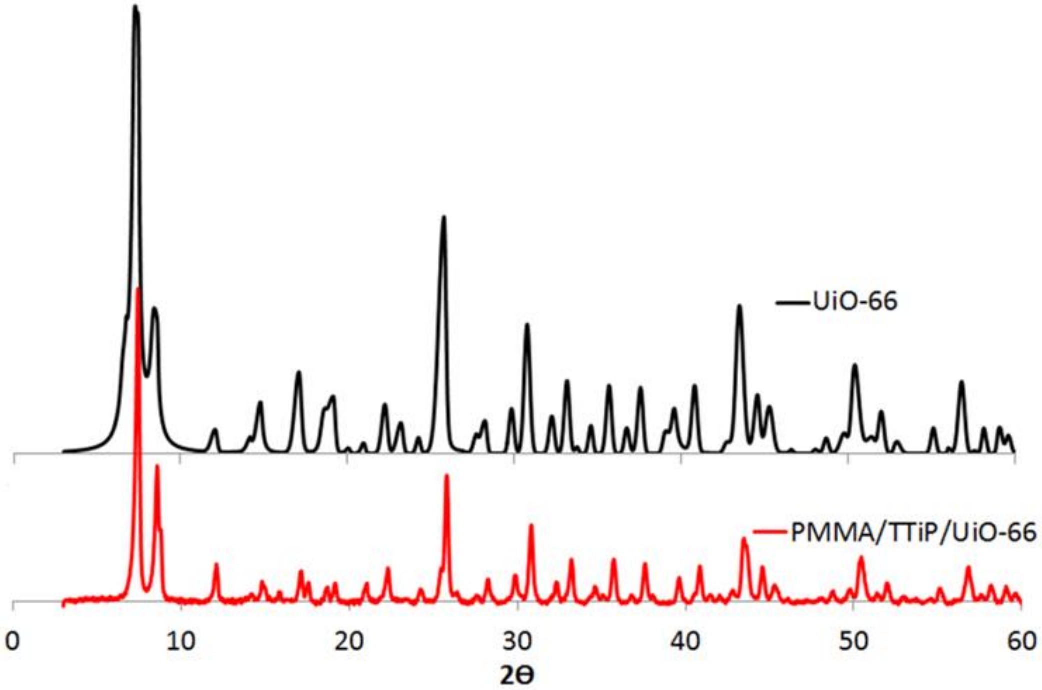

Figure 3-8. XRD pattern of UiO-66 (black) and PMMA/TTiP/UiO-66 (red) composite fibers.

Attenuated total reflectance Fourier transform infrared (ATR-FTIR) spectroscopy was used to characterize the functional groups of the polymer seen in **Figure 3-9**. PMMA contains characteristic peaks below 2000 cm^{-1} with a C=O ester stretch at 1720 cm^{-1} and a C-O-C mode between 1200 and 1100 cm^{-1}. UiO-66 did display a characteristic peak not commonly shared with PMMA seen at 1550 cm^{-1}. Upon analysis of the composite fibers containing both PMMA and UiO-66, the strong C=O ester stretch is visible as well as the stretch for UiO-66.

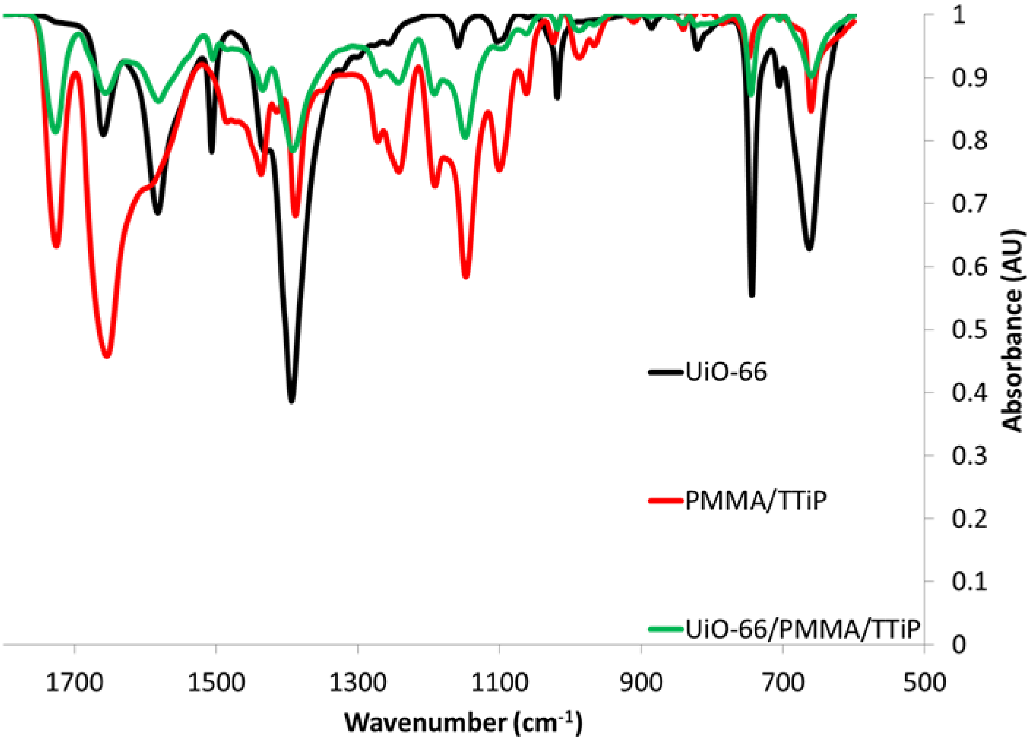

Figure 3-9. ATR-FTIR spectra of UiO-66 (black), PMMA/TTiP (red) and PMMA/TTiP/UiO-66 (green)

Completion of analysis by SEM, TEM, XRD and ATR-FTIR confirmed the integrity of the UiO-66 and the polymer composite fibers remained intact after the electrospinning process.

3.3.1.2 Polymer Composite Fibers Containing UiO-66 NH_2

3.3.1.2.1 Scanning Electron Microscopy and Tunneling Electron Microscopy

Composite polymer fibers containing UiO-66 NH2 were analyzed by SEM and TEM. **Figure 3-10** represents PMMA fibers containing both UiO-66 NH_2 and TTiP. PMMA/TTiP/UiO-66 NH_2 retained the same folded surface morphology as the fibers seen in **Figure 3-6**. The diameters of these fibers were also consistent with the PMMA/TTiP/UiO-66 composite fibers with diameters averaging approximately 795 nm. When TTiP is not included as a precursor to the composite fiber the morphology changes to a more amorphous surface. However the UiO-66 NH_2 looks to be incorporated within the fiber consistent with all other composite fibers. The diameter averaged approximately 425 nm and was very consistent throughout the sample, with little deviation.

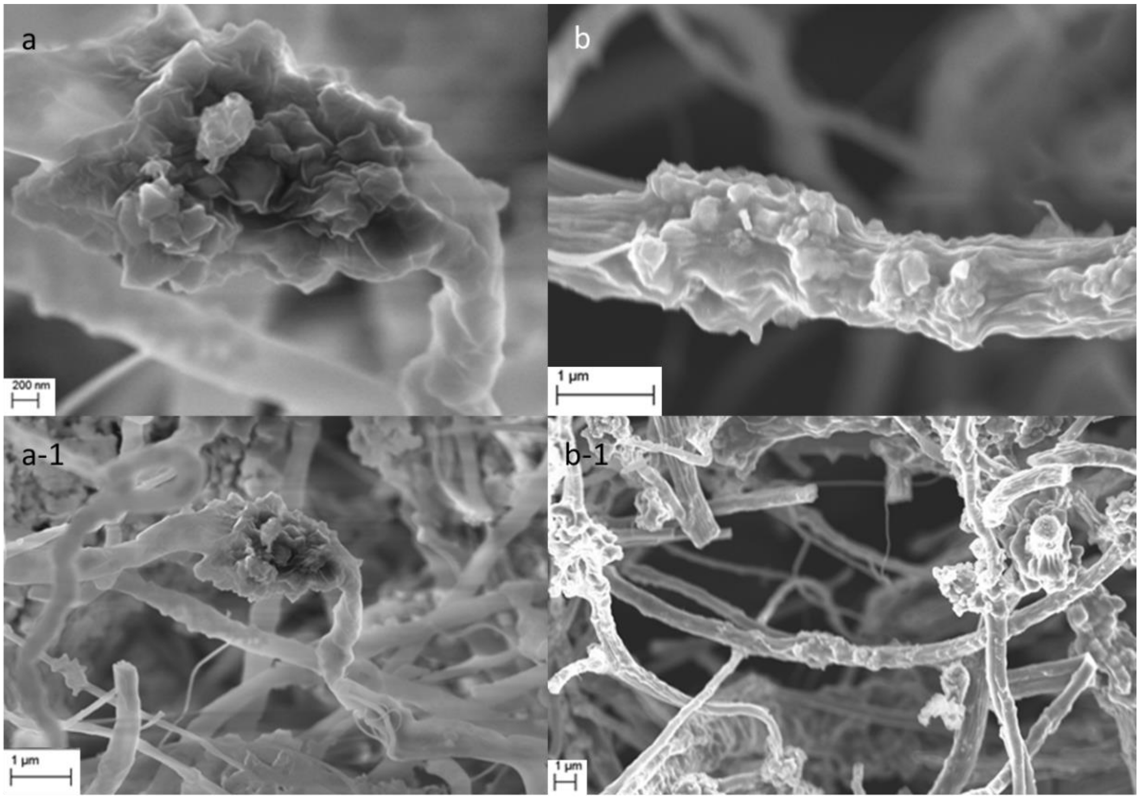

Figure 3-10. SEM imaging of (a), (a-1) PMMA/UiO-66 NH_2 and (b), (b-1) PMMA/TTiP/UiO-66 NH_2

TEM imaging was necessary to investigate the size and shape of the UiO-66 NH_2 MOF is more defined, as seen in **Figure 3-11**. The cubic shape is consistent with that of UiO-66 which is expected since the only variable change was the addition of an amine group. The diameter of the MOF was uniform, with small variations averaging approximately 75 nm.

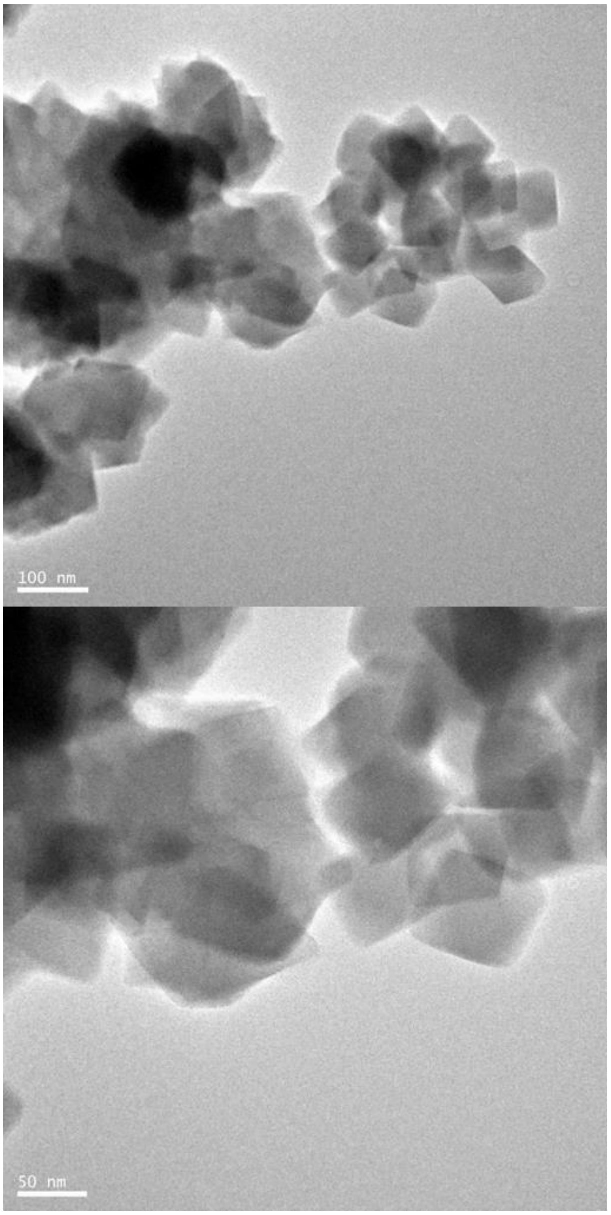

Figure 3-11. TEM imaging of UiO-66 NH_2

3.3.1.2.2 X-Ray Diffraction

UiO-66 NH_2 displays many of the same characteristic XRD peaks as UiO-66 including the two diffraction lines that are indicative of UiO-66 series at a 2Θ of 7.34° and 8.48°.

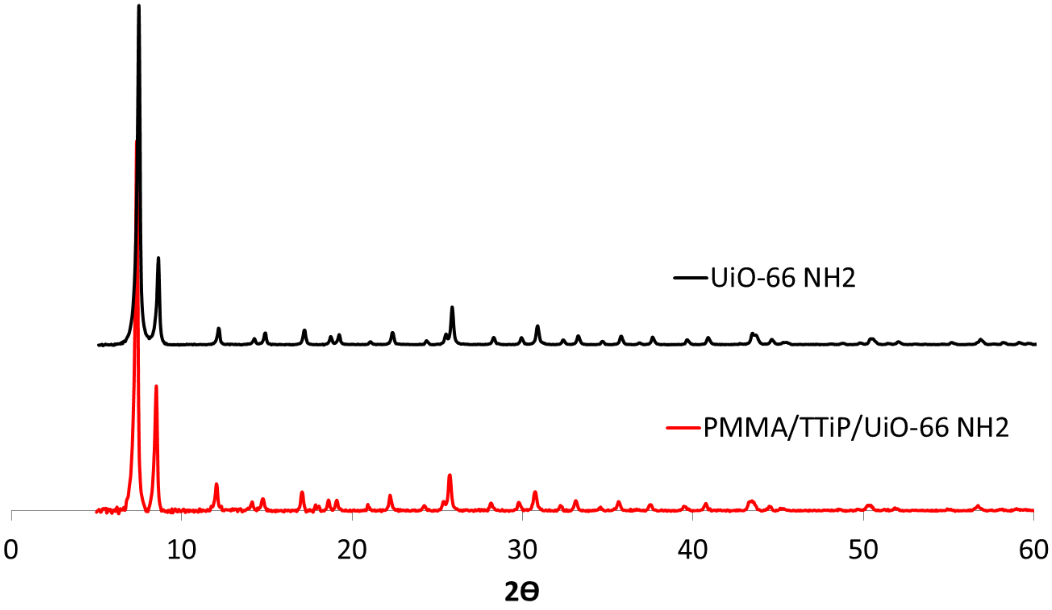

Figure 3-12. XRD pattern of UiO-66 NH_2 (black) and PMMA/TTiP/UiO-66 NH_2 (red)

The resulting XRD diffraction pattern is shown in **Figure 3-12**, with the characteristic diffraction lines remaining both prior to and post electrospinning. There are no other peaks present or shifting in the post electrospun sample (red) that would suggest the formation of amorphous or any other form of TiO_2.

3.3.1.3 Electrospun TiO_2/ UiO-66 Nanofibers

3.3.1.3.1 Scanning Electron Microscopy and X-Ray Diffraction

Fabrication of TiO_2/UiO-66 nanofibers was achieved by adding 5 wt % UiO-66 to the sol gel prior to electrospinning and calcining the nanofibers at 285°C for 4 hours. SEM analysis showed the fibers possess an average diameter of 388nm, **Figure 3-13**.

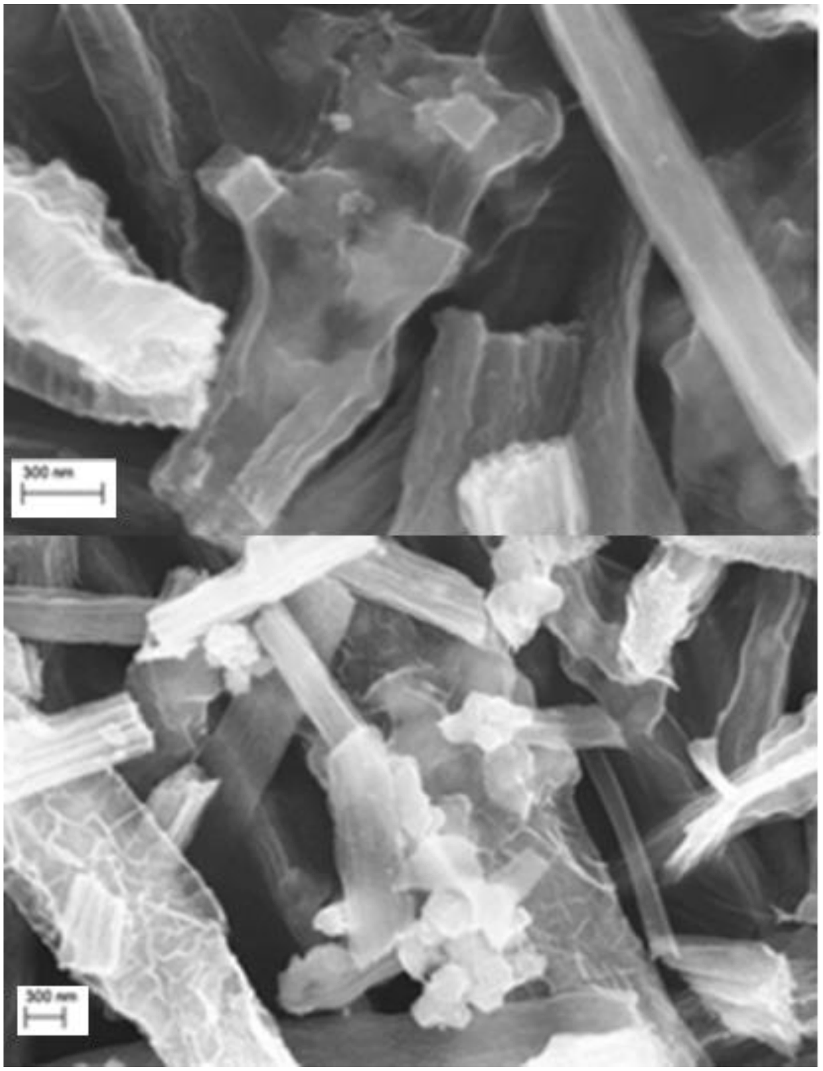

Figure 3-13. SEM images of 5 wt% UiO66/TiO_2 nanofibers post 285°C calcination.

UiO-66 was also seen within the fibers and not solely on the surface. In analysis of the SEM images UiO-66 appears to have maintained it cubic shape. Some of the TiO_2 has changed in morphology from folded and wrinkled to what seems to be cracked and fractured. XRD was carried out to confirm that the structural integrity of the MOF stayed intact by examining the diffraction pattern.

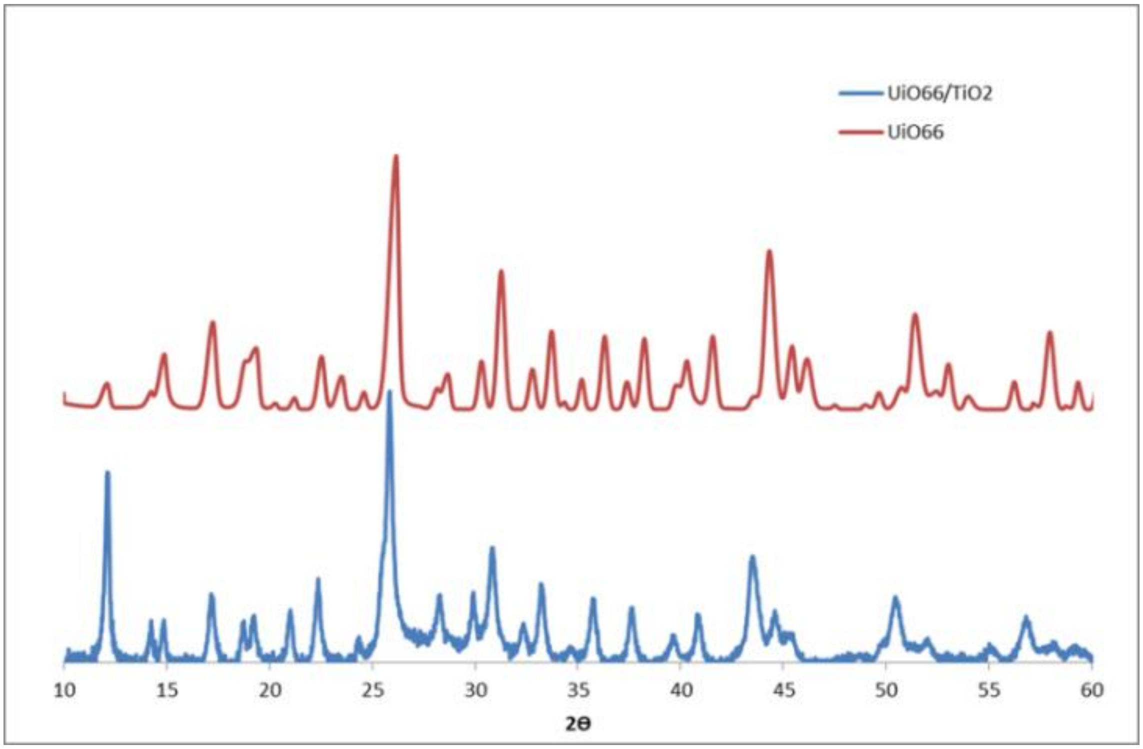

Figure 3-14. XRD comparison of UiO-66 to TiO_2/ UiO-66 nanofibers.

The XRD of the TiO_2/UiO-66 was compared to pure UiO-66. There is a strong characteristic peak of UiO-66 located at 25 °. It can be seen that even after 4 h of thermal treatment at 285 °C the diffraction line remains as well as the intensity, **Figure 3-14**.

3.3.2 Degradation of Methyl Paraoxon with UiO-66 Composite Fibers

3.3.2.1 Light versus Dark

Fabricated electrospun PMMA/TTiP/UiO-66 composite fibers were used to degrade methyl paraoxon demonstrating exceptionally fast kinetics and high conversion to nitrophenoxide. 5 wt% UiO-66 blended with PMMA and TTIP nanofibers were introduced to an aqueous solution of N-ethyl morpholine used as a pH 10 buffer. Methyl paraoxon was introduced to the solution and aliquots were extracted at pre-determined times and concentration was measured using UV-Vis spectroscopy, **Figure 3-15.**

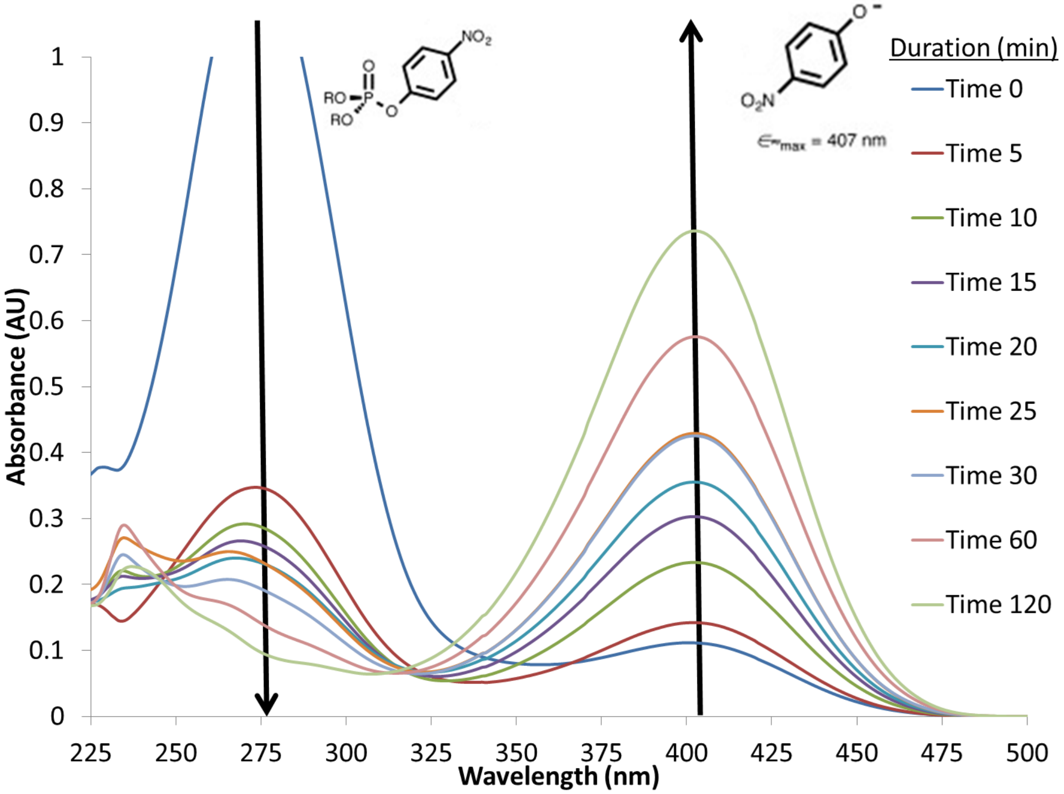

Figure 3-15. UV-Vis spectra of the degradation of methyl paraoxon with PMMA/TTiP/UiO-66 without UV irradiation.

Within the first 5 min of contact between the fibers and methyl paraoxon, a drastic decrease in the reactant peak was observed, at which time the nitro phenoxide product peak absorbance at 407 nm started to increase. The hypothesis is this is a heterogeneous binding event where pre-adsorption is occurs. There is considerable complexity to the kinetics of the overall reaction. By 120 min, 94 % of the methyl paraoxon was fully converted to 4-nitrophenoxide and dimethyl phosphate with a calculated half-life of 29 min and first order initial rate constant of 0.023 M·minute. The resulting solution showed a visible yellow color due to the presence of 4-nitrophenoxide.

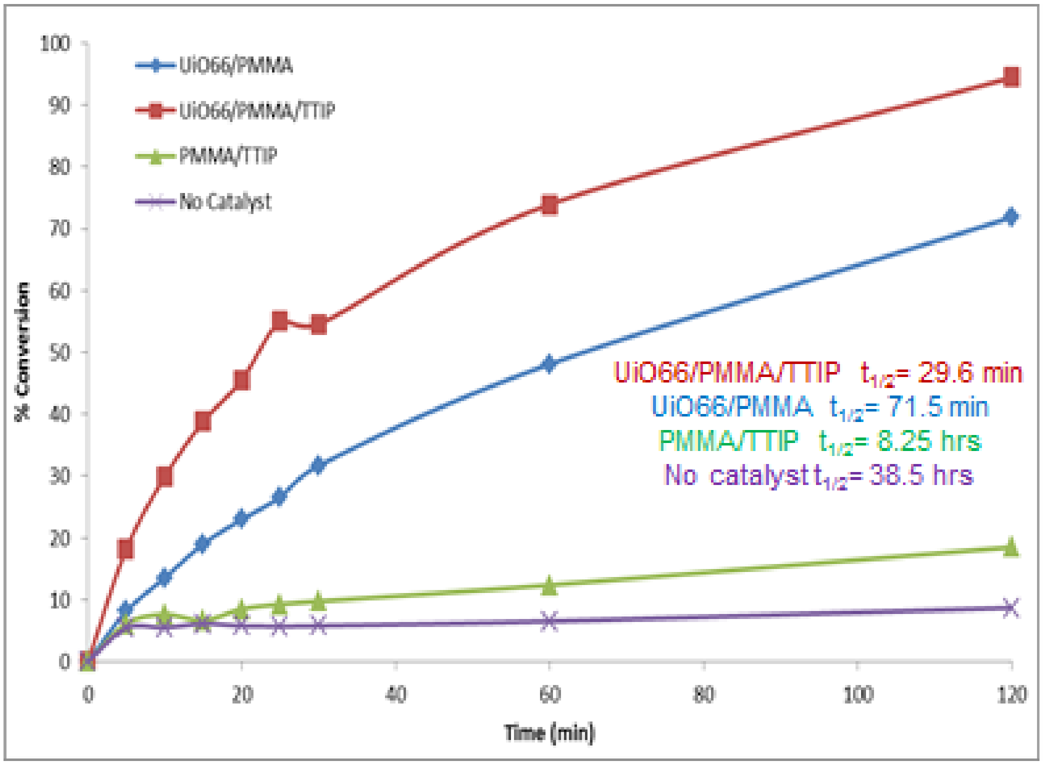

Figure 3-16. Comparison of catalyst with varying compositions. Percent conversions are shown as a function of time in minutes.

A series of experiments were performed both with and without the catalyst as well as catalyst both with and without TTiP and UiO-66. In **Figure 3-16**, the catalyst without TTiP on PMMA and 5wt% UiO-66 still had a considerable degradation response to methyl paraoxon, while PMMA/TTiP without the UiO-66 exhibited an even slower degradation rate. Both the TTiP and UiO-66 can be acting as a Lewis acid to promote a base catalyzed reaction. This would result in the fast half-life and high percent conversion to nitrophenoxide.

MOF/polymer composite fiber blends and their behavior in both dark and light conditions have been investigated. What has been observed is a drastic variation in half-life and percent conversion when methyl paraoxon is degraded in the dark vs. light. PMMA/TTiP/UiO-66 composite fibers were used to degrade methyl paraoxon demonstrating exceptionally fast kinetics and high percent conversion after 120 min of exposure, **Figure 3-17**.

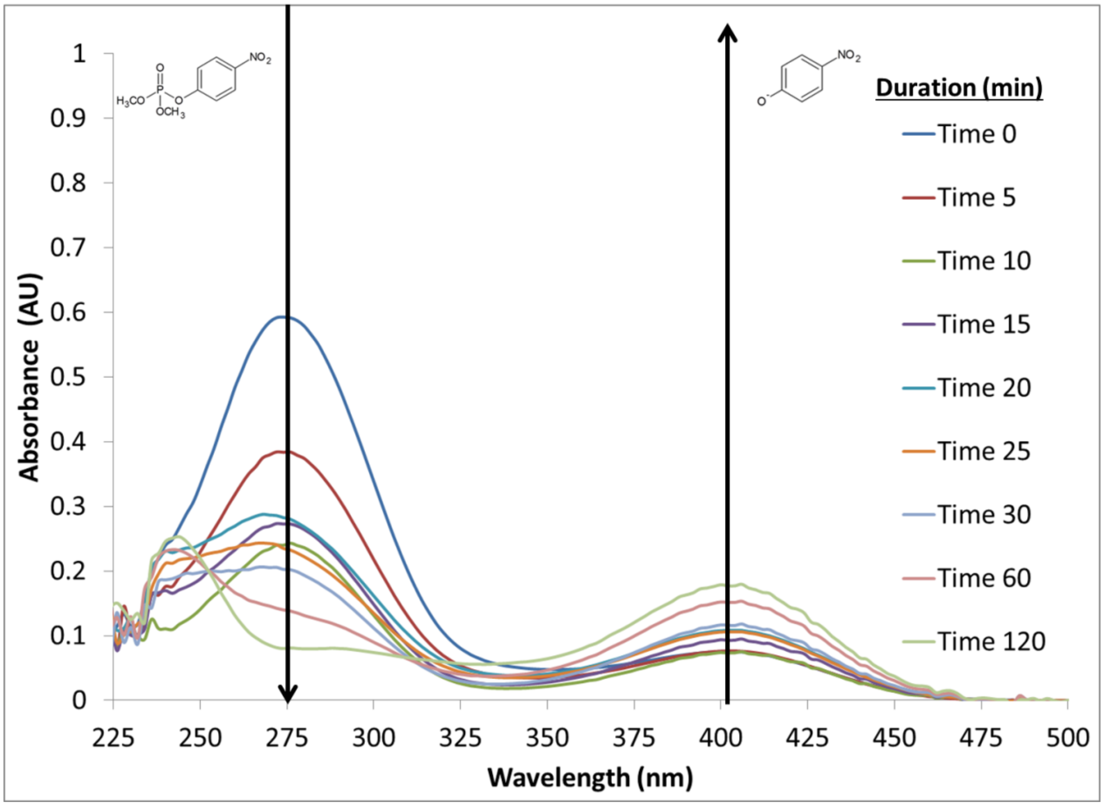

Figure 3-17. UV-Vis spectra of the degradation of methyl paraoxon with PMMA/TTiP/UiO-66 with UV irradiation.

In the presence of UV irradiation a very different outcome is observed. The decrease of the parent peak is a slower process, and there is very little change in absorbance of the nitrophenoxide product after 120 min. Only 22.9 % of methyl paraoxon was converted to product, with a half- life of 6.79 hours and a first- order initial rate constant of 0.002 M·min. Light and dark experiments were compared for samples with varying concentration, **Table 3-1**.

Sample	Dark		UV Light	
	t½ min	% Conversion	t½ min	% Conversion
PMMA/TTiP/UiO-66	29.6	94.8	407	22.9
PMMA/UiO-66	71.5	71.8	256	39.4
PMMA/TTiP	495	18.5	768	14.1
UiO66	*45	*85	106	69.9
No Catalyst	2310	8.69	990	11.4

Table 3-1. Table comparing light v. dark degradations of methyl paraoxon. Table shows the trend of half-life and % conversion for each sample. *Degradation results of UiO-66 in the dark were obtained from Northwestern and reported in *Angewandte Chemie International Edition* **2014,** *53* (2), 497-501.

The hypothesis is that there are different mechanistic reactions occurring in the dark vs, the light. Literature reports have established that the dark reactions are the result of base-catalyzed hydrolysis, and will result in a species with an absorbance in the visible region. Therefore, the growth of the product peak can be monitored and the half-lives and percent conversions can be calculated assuming these samples have first-order kinetics. Further analysis was conducted into the kinetics of these degradation experiments and results can be seen in Section 3.3.2.2. When the reaction was performed in the light long half-lives and low conversions were observed. There was also no clear trend in results when the degradation was performed in the light, as there was in the dark reactions.

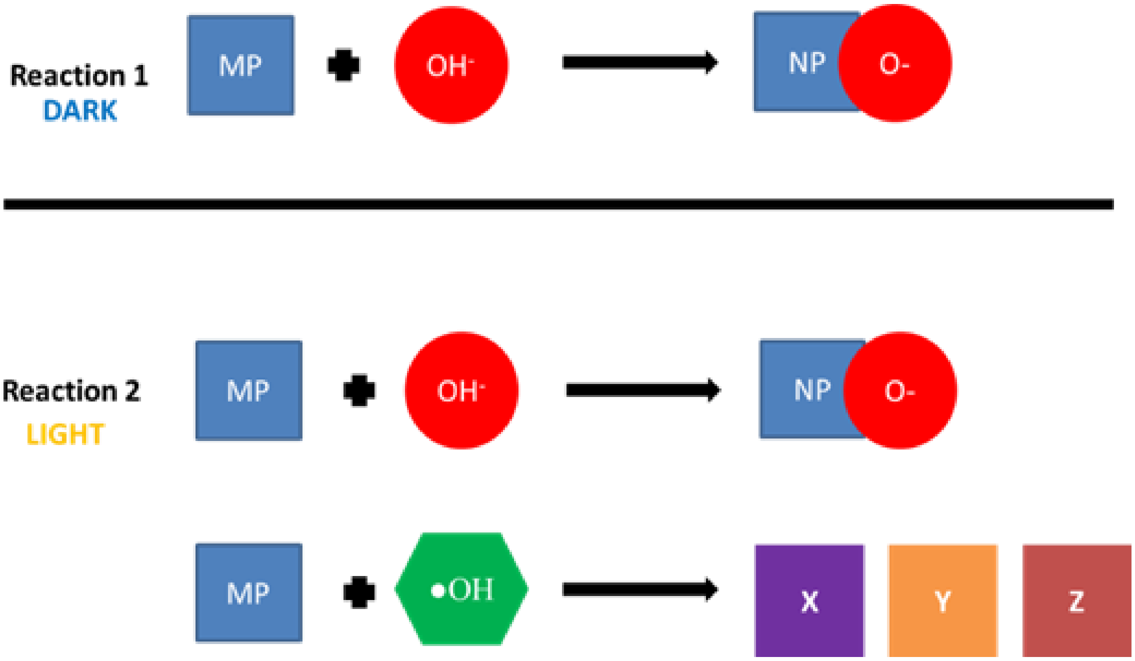

Figure 3-18. Proposed mechanistic reaction of methyl paroxon degradation in the dark v. the light.

Initially it was hypothesized that the light introduced to the reaction was decreasing the rate of degradation somehow, but that may not be the case. However, it is possible that different mechanisms are occurring in the light that do not produce species that absorbs UV or visible light, therefore making it difficult to monitor the degradation process using UV Vis spectroscopy, **Figure 3-18**. It is known that photocatalysts use radical degradation with the aid of irradiation to produce reactive radical species, which in turn degrade the target pollutant. This has led to the hypothesis that the composite fibers containing TTiP have hydrolyzed and produced a small amount of amorphous TiO_2. Therefore, upon irradiation with UV light, electron-hole pairs are formed and will react with any absorbed water and oxygen, producing hydroxyl and peroxide radicals promoting degradation of the methyl paroxon but producing a non UV-Vis absorbing product. In previous experiments with other simulants seen in Chapter 2, NMR was used as a technique to observe and track degradation. NMR methods could be used to examine the radical degradation of methyl paraoxon in the light to confirm our hypothesis.

3.3.2.2 Statistical and Kinetic Data

Multiple trials of these experiments were needed to obtain statistical bases for assessment and more accurate kinetic data. Testing began with the PMMA/TTiP/UiO-66 sample described in Table 3-2. The degradation procedure and catalyst remained unchanged to ensure accurate results. The experiments were done over the course of 3 months and the results were unexpected.

Sample	**Date**	**t ½**	**% Conversion**	**Rate Order**	**Rate Constant (M·min)**
PMMA/TTiP/UiO-66	7/28/15	29.6 min	94.8	1st	0.0230
PMMA/TTiP/UiO-66	10/15/15	42.5 min	87.5	1st	0.0163
PMMA/TTiP/UiO-66	10/22/15	N/A	74.5	2nd	0.0237

Table 3-2. PMMA/TTiP/UiO-66 degradation with methyl paraoxon was repeated on three different dates ranging over 3 months. The table shows a decrease in percent conversion as time elapses.

It was seen that each time the experiment was performed, the half-life and percent conversion became longer and lower respectively. Current hypotheses are that the TTiP is hydrolyzing and forming some type of amorphous TiO_2 that is possibly aggregating, and the longer the catalyst is exposed to atmospheric conditions the more TiO_2 is formed that will aggregate. Due to the previous results and hypothesis aforementioned the longer half-life and lower percent conversion would make sense for the reason that another degradation mechanism resulting from TiO_2 would be competing with the hydrolysis mechanism of the methyl paraoxon.

After seeing a sizeable variation in percent conversions and rate constants in **Table 3-3**, a new sample of PMMA/TTiP/UiO-66 was fabricated under the same parameters for testing. These fibers underwent four degradation experiments with methyl paraoxon to gather statistical data and grasp a better understanding kinetically what is occurring.

Sample PMMA/TTiP/UiO-66	**% Conversion**	**Rate Order**	**Rate Constant (M·min)**	**t ½**
Trial 1	58.7	2nd	0.0111	N/A
Trial 2	54.1	2nd	0.0095	N/A
Trial 3	73.4	2nd	0.0225	N/A
Trail 4	66.8	2nd	0.0167	N/A

Table 3-3. PMMA/TTiP/UiO-66 trial data. This table depicts percent conversion, rate order, rate constant and half-life.

During this series of testing all of the rates were second order, making it nearby impossible to calculate the half-lives of these reactions due to the fact the concentration varies over the course of the 120 min degradation. Second-order kinetics are dependent upon the initial concentration and because there are two separate species being monitored and used to determine rate constant and percent conversion, it becomes impossible to say with certainty the projected half-life. However, what is seen in **Table 3-3** is consistent; as the percent conversion increases so does the rate of the reaction.

All four trials were combined in a graph to display the error between experiments, **Figure 3-19**. As the duration of time increases through the experiment, the error bars increase. It is uncertain what would be the cause of such a large possible variation at the later time of the experiment.

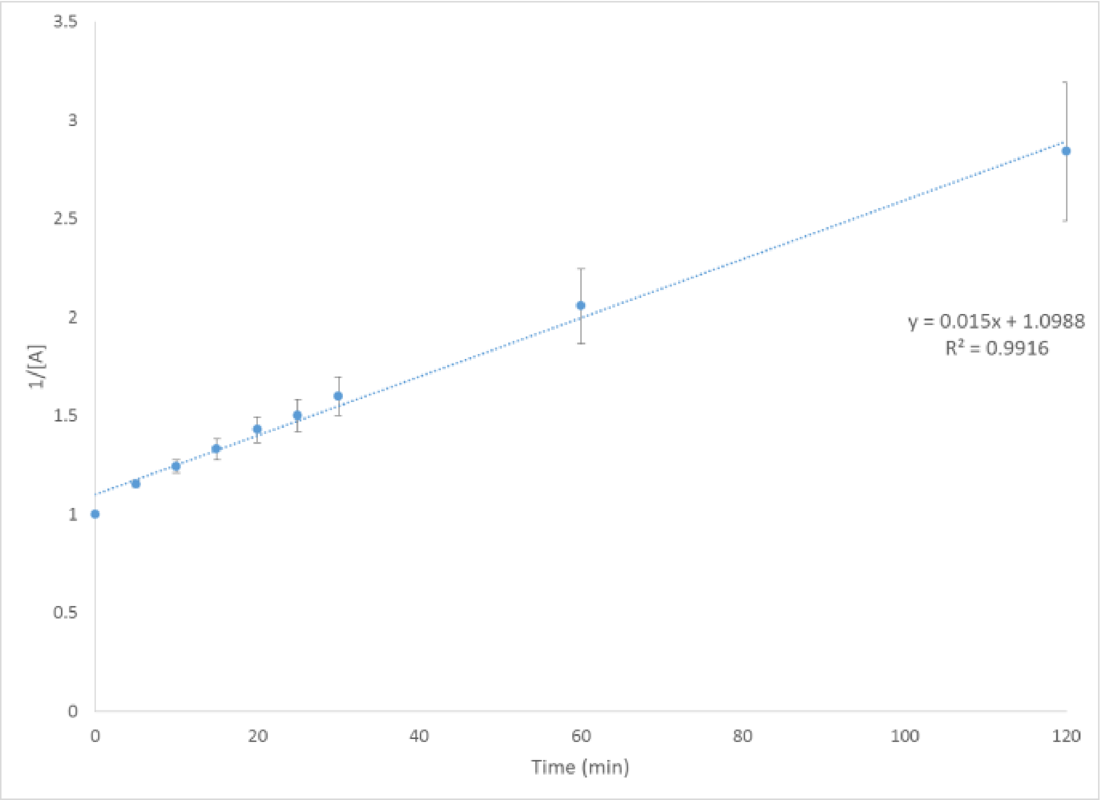

Figure 3-19. Graph depicting time vs. 1/[A] and the error bars associated with the four trials run with the sample originating from the same batch.

Experiments are still ongoing to determine the cause of variation in the rate and percent conversion of methyl paraoxon. Theories have been drawn but it is still too early to come to any definitive conclusions.

During the course of the experiments a dip in the absorbance of the reactant became noticeable. It was uncertain what this decreased absorbance was attributed too and it only seemed to effect the last aliquot at 120 min, **Figure 3-20**. Hypotheses include that the N-ethyl morpholine buffer in which the degradation experiments are carried out might be the cause of this negative absorbance.

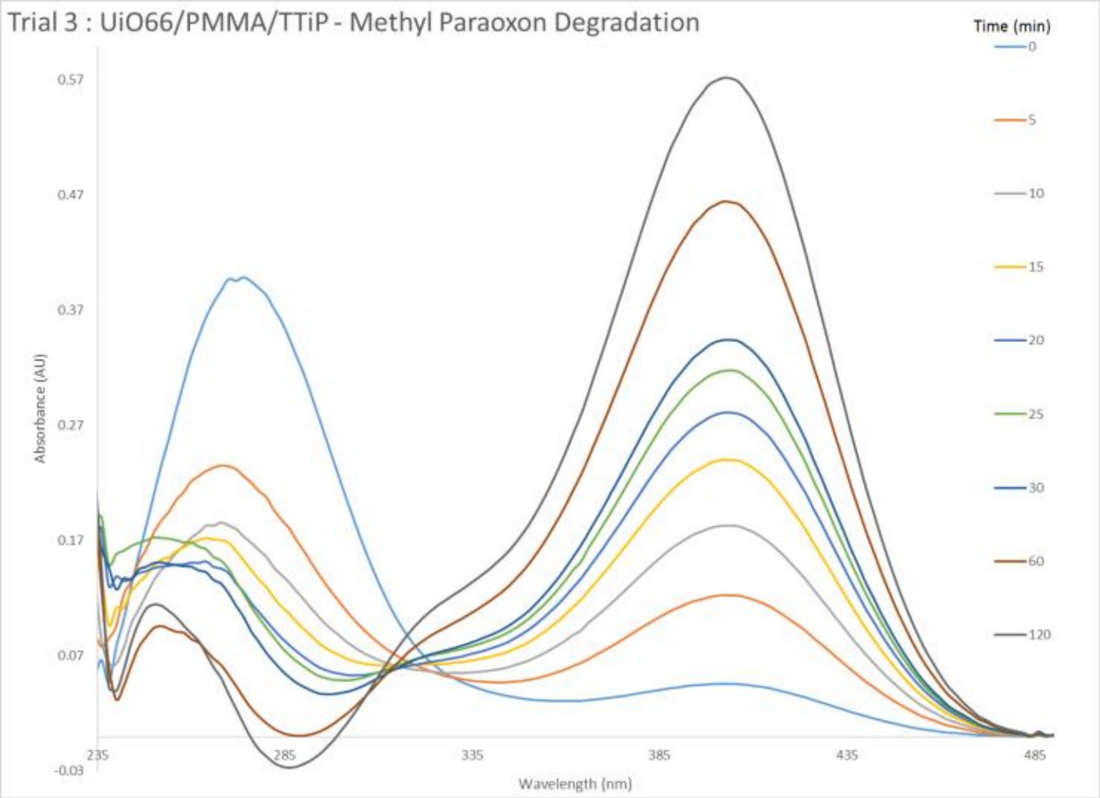

Figure 3-20. UV-Vis spectra from trial 3 with UiO66/PMMA/TTiP degradation of methyl paraoxon. The spectra show the dip in concentration of the parent peak after 120 minutes of exposure during the degradation.

To confirm this hypothesis a UV Vis spectrum was obtained of the buffer solution both before the experiment began and at the completion of 120 min. What was seen was validation that the decreased absorbance at around 285 nm was due to the N-ethyl morpholine absorption as well as baseline interference from the instrument.

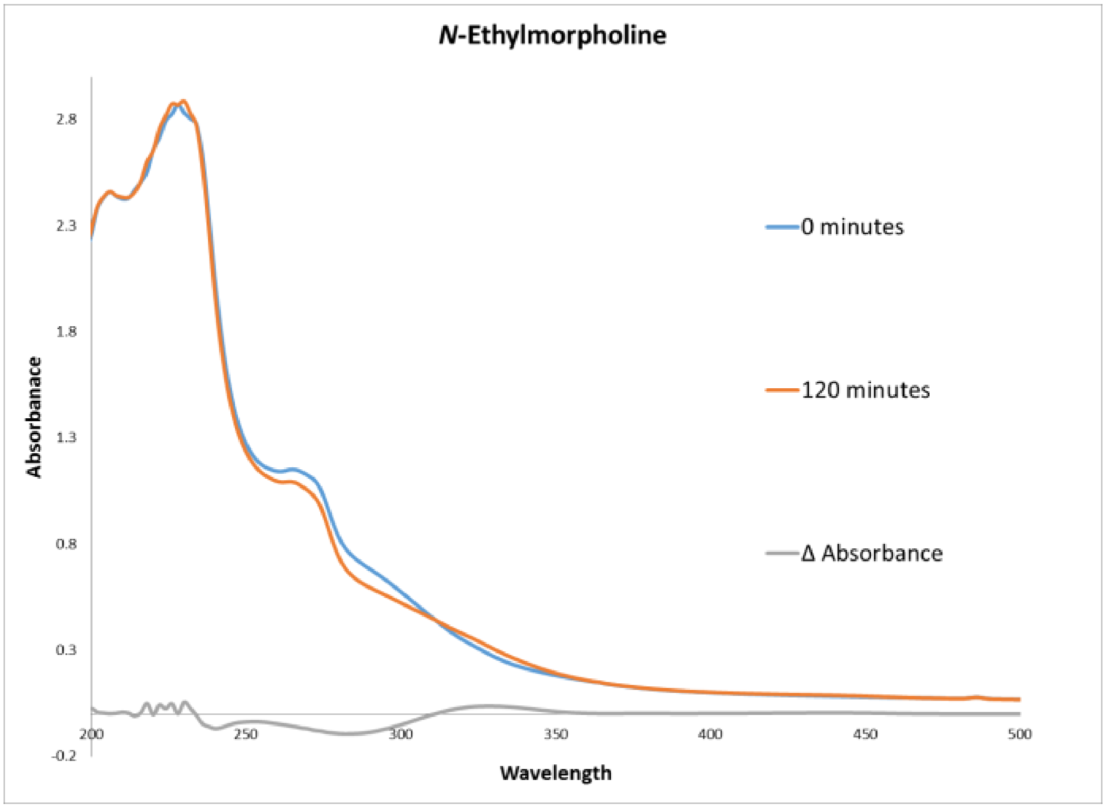

Figure 3-21. UV-Vis spectra of N-ethyl morpholine before and after 120 minute degradation with methyl paraoxon. The sample was extracted from stock solution prior to and post degradation.

In **Figure 3-21**, the absorbance spectrum matches before and after the experiment with the exception of around 280 nm. This change in absorbance over time led to the decreased absorbance seen in **Figure 3-18**. This will need to be taken into consideration in future degradation experiments. In forthcoming experiments the disappearance of the parent peak of methyl paraoxon will also be studied to determine its kinetics.

The statistical trials proved to have a best fit to second-order kinetics and an hypothesis was formed about competing mechanistic reactions. Preliminary analysis indicated the loss of the reactant favors a second-order reaction in the sample showing a conversion of 94.3%. The formation of the product peaks shows a clear preference to a first-order reaction, which was seen during the initial analysis of the data, **Figure 3-22 and 3-23**.

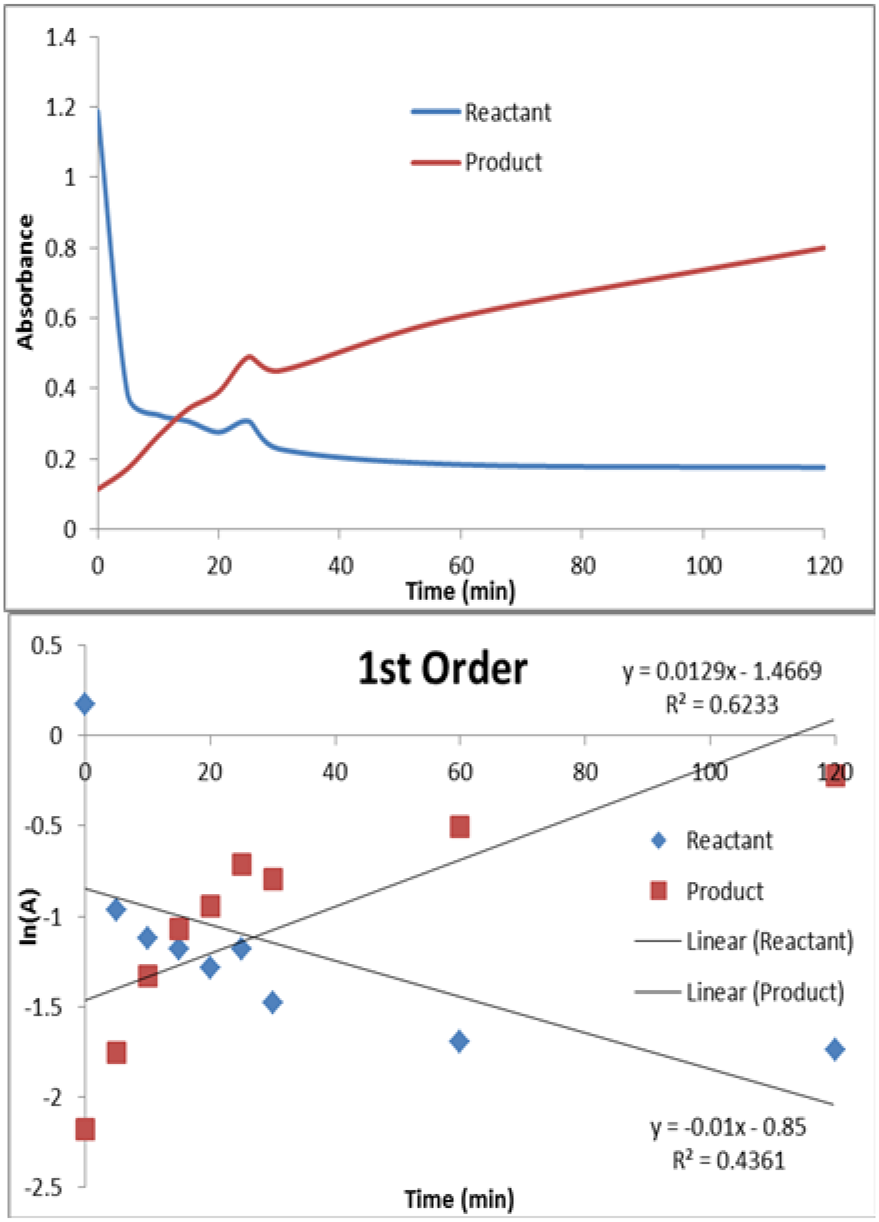

Figure 3-22. PMMA/TTiP/UiO-66 nanofibers with 94.3 % conversion, first-order analysis.

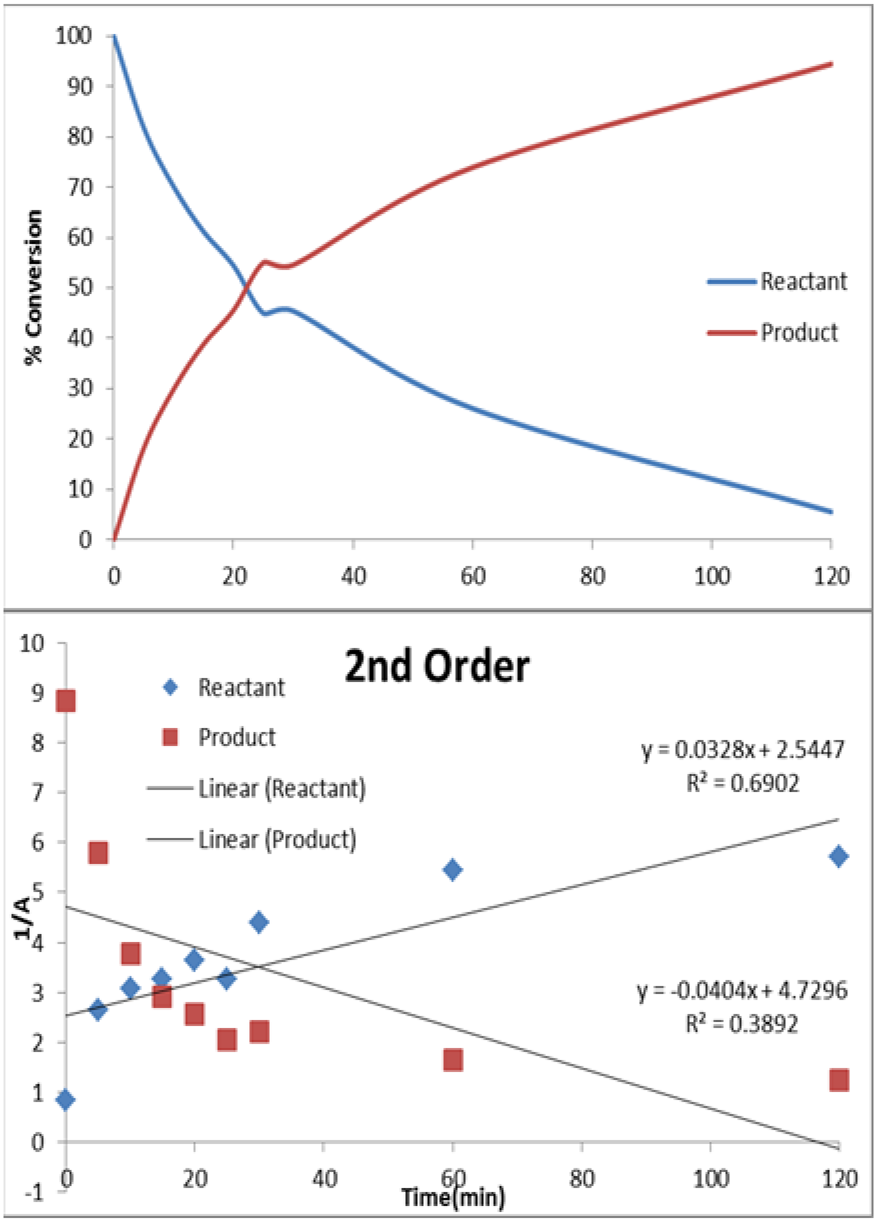

Figure 3-23. PMMA/TTiP/UiO-66 nanofibers with 94.3 % conversion, second-order analysis.

When examining the result acquired from Trial 3 of the statistical data there was a distinct preference for second-order kinetics for the formation of the nitrophenoxide product. In the initial examination of the reactant, second-order process is also observed which is comparable to the sample in **Figure 3-24 and 3-25**.

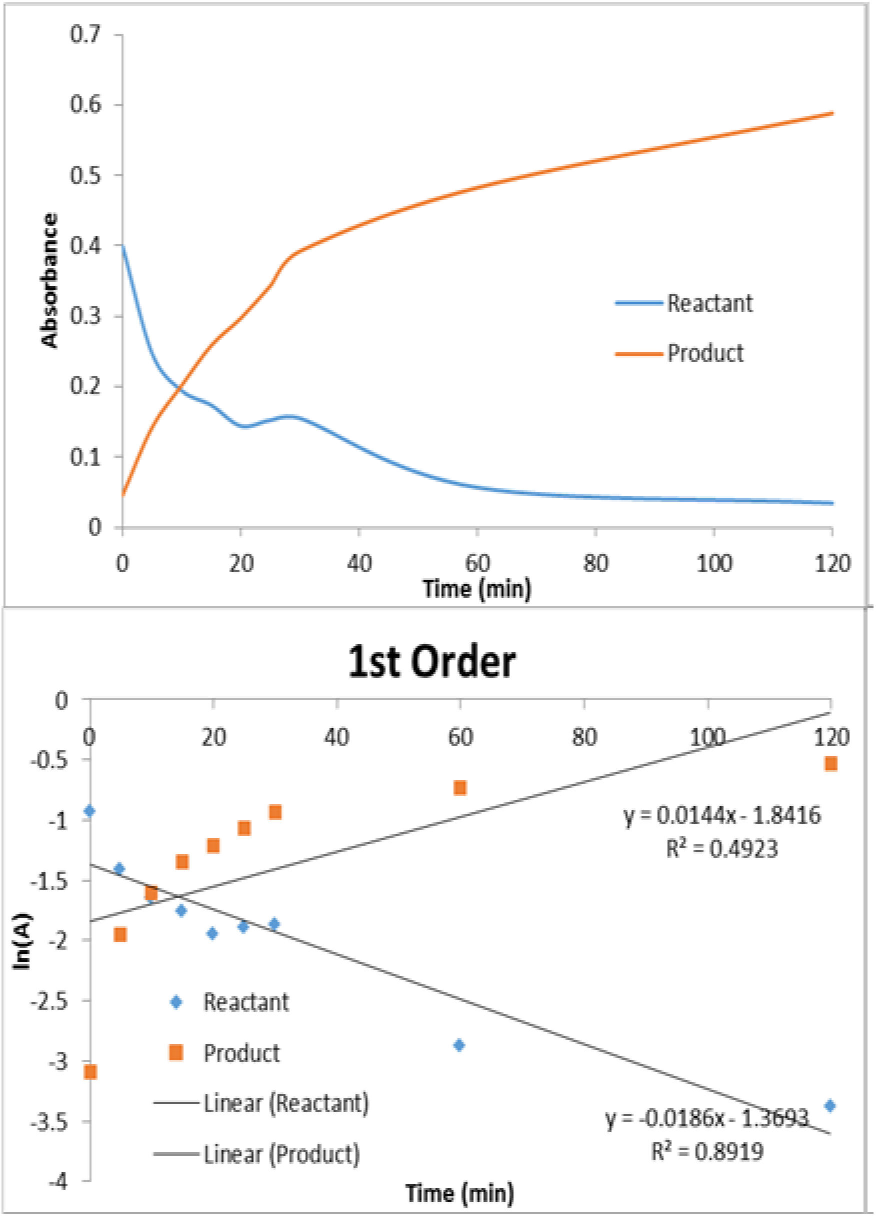

Figure 3-24. PMMA/TTiP/UiO-66 nanofibers with 73.4 % conversion, first-order analysis.

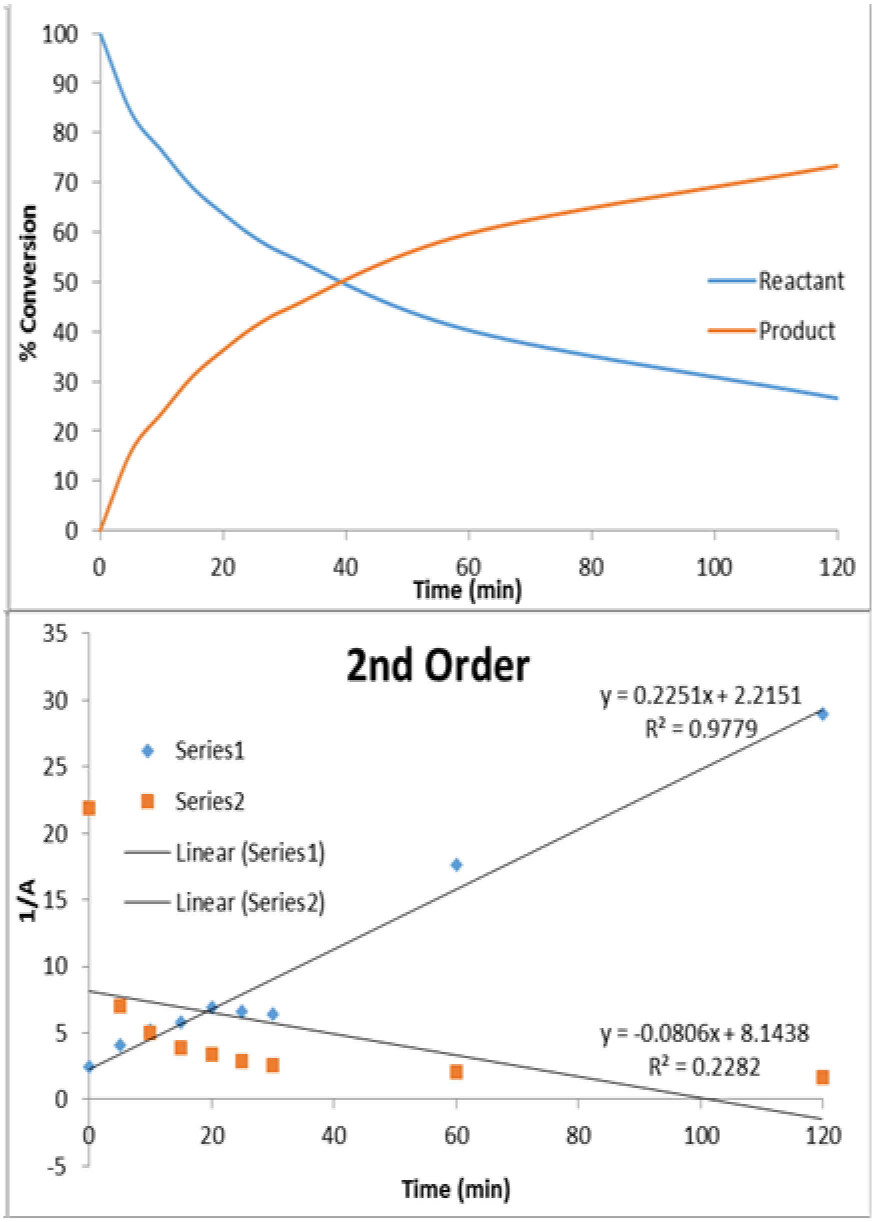

Figure 3-25. PMMA/TTiP/UiO-66 nanofibers with 73.4 % conversion, second-order analysis.

Most of the complexity of the observed kinetics lies within the first 5 min of the reaction. The forming hypothesis is this is a heterogeneous binding event in the first 5 min, where pre adsorption is occurring. There is considerable complexity to the kinetics of the overall reaction, and further analysis into the understanding of this process is ongoing.

3.3.3 Degradation of Methyl Paraoxon with UiO-66 NH_2 Composite Fibers

3.3.3.1 Light vs. Dark

Electrospun PMMA/TTiP/UiO-66 NH_2 composite fibers were fabricated under the same conditions aforementioned with UiO-66. 5 wt% UiO-66 NH_2 blended with PMMA and TTIP nanofibers were introduced to an aqueous solution of N-ethyl morpholine used as a pH 10 buffer. Methyl paraoxon was introduced to the solution and aliquots were extracted at pre-determined times and the concentration was measured using UV-Vis spectroscopy.

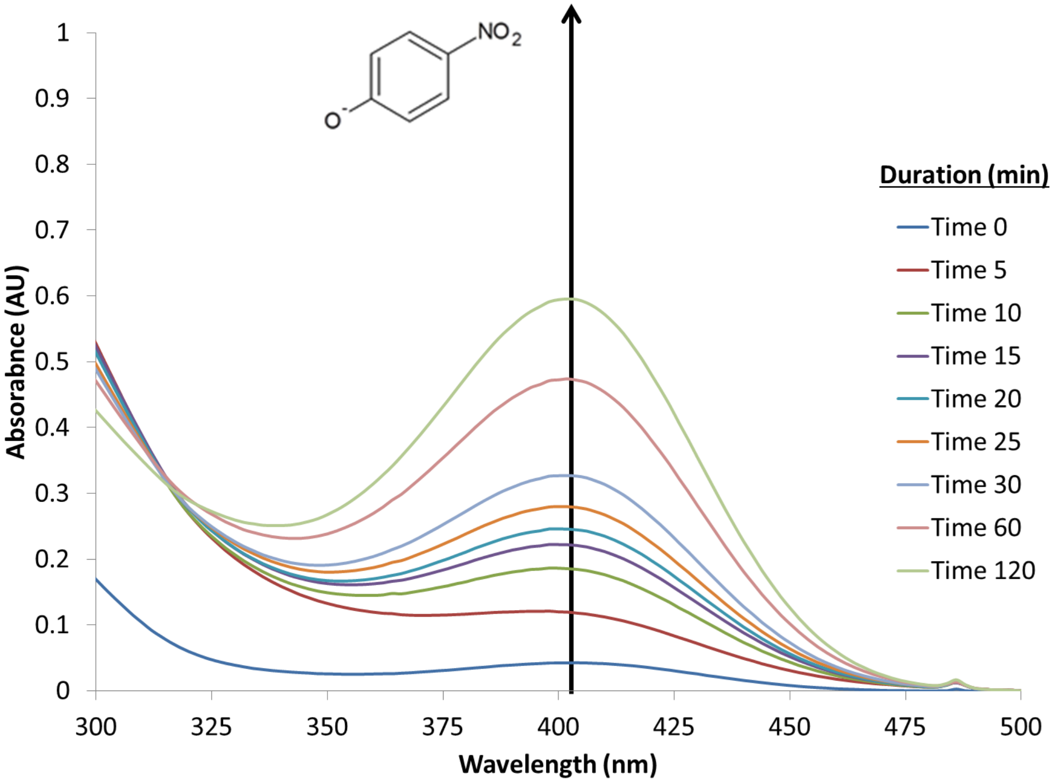

Figure 3-26. UV-Vis spectra of the degradation of methyl paraoxon with PMMA/TTiP/UiO-66 NH_2 without UV irradiation.

The nitrophenoxide product peak grew over the course of 120 min. After about 10 min, an absorbance maximum was visible for the product at 407 nm. Methyl paraoxon in the presence on PMMA/TTiP/UiO-66 NH_2 showed a 76.1 % conversion to product. The resulting percent conversion is considerably lower than the seen for polymer composite fibers containing UiO-66 at 94.3 % conversion without the presence of UV irradiation, **Figure 3-26**.

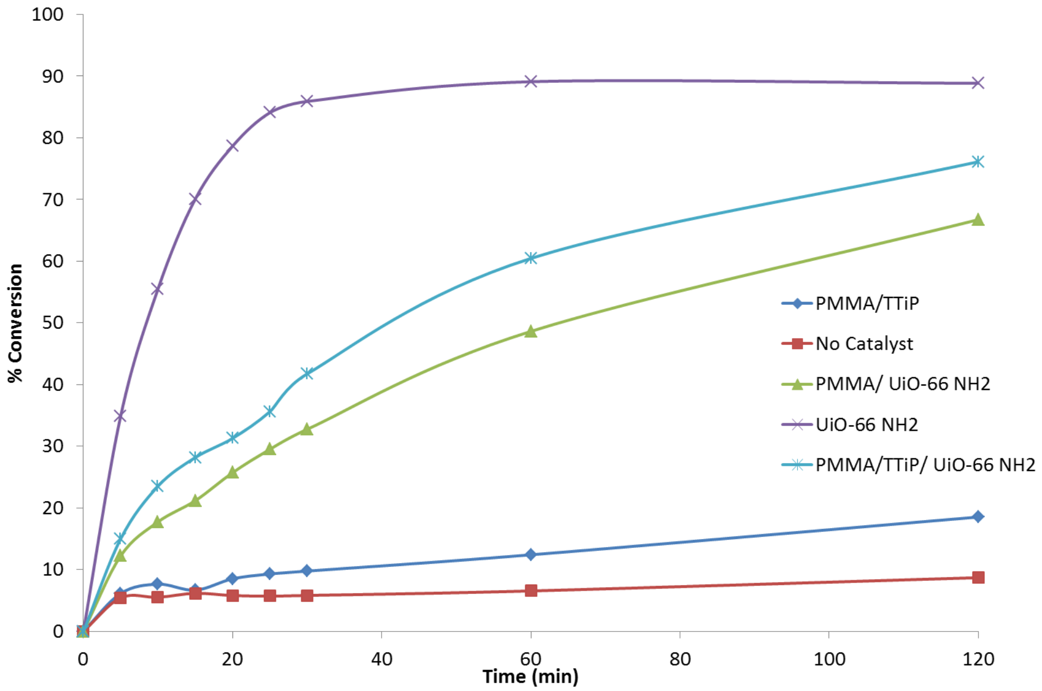

Figure 3-27. Comparison of catalyst with varying compositions. Conversions as a function of time.

When comparing different composition samples it can be seen that UiO-66 NH_2 alone has the highest conversion, and the composite fibers containing the MOF have significantly lower in values, **Figure 3-27**. It was also observed that there was a higher rate of conversion within the first 30 min in the sample containing just the MOF then seen in any of the other samples that were analyzed. This has led to possible theories that the amine functional group from the MOF could be playing a role in hindering the degradation process. This could arise from other potential binding interactions between the UiO-66 NH_2 and the PMMA/TTiP not seen in samples containing solely UiO-66.

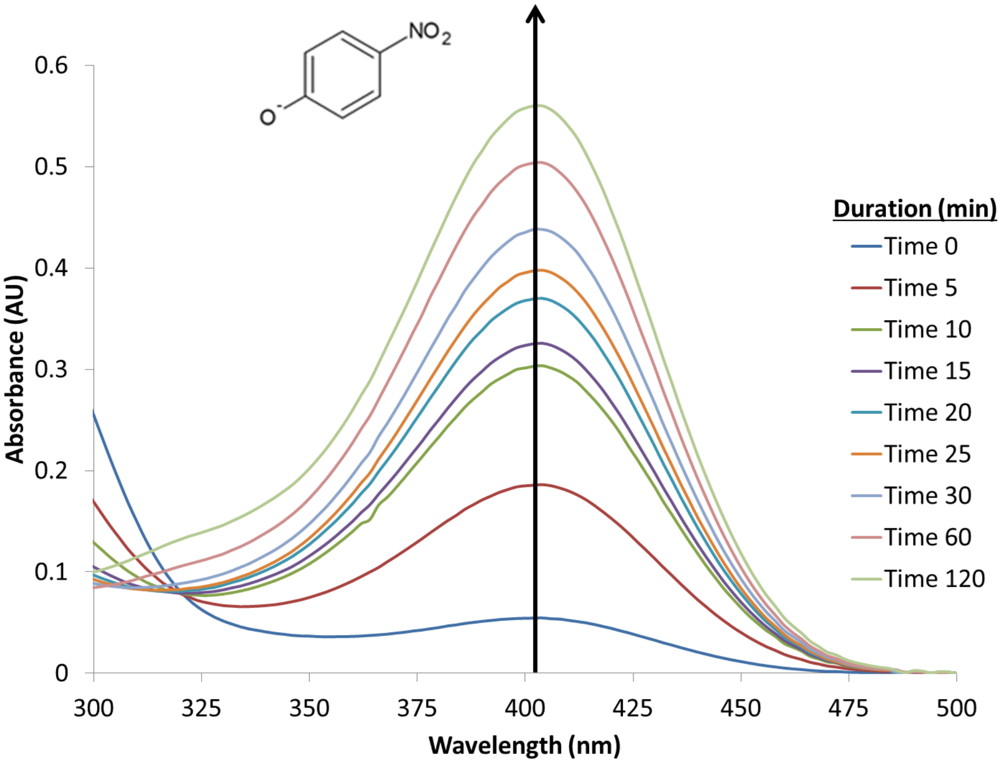

Figure 3-28. UV-Vis spectra of the degradation of methyl paraoxon with PMMA/TTiP/UiO-66 NH_2 with UV irradiation.

The sample was then exposed to UV irradiation under consistent experiment parameters. The conversion of PMMA/TTiP/UiO-66 NH_2 in the presence of UV irradiation was 71.8 %, which is comparable and likely with the margin of error as the same sample in dark conditions, **Figure 3-28.** However, there was a larger increase in absorbance within the first 5-10 min of irradiation.

Sample	Dark	UV Light
	% Conversion	**% Conversion**
PMMA/TTiP/UiO-66 NH_2	76.1	71.8
PMMA/UiO-66 NH_2	66.7	52.9
PMMA/TTiP	18.5	14.1
UiO-66 NH_2	88.8	47.1
No Catalyst	8.69	11.4

Table 3-4. Table comparing light v. dark degradations of methyl paraoxon. Table shows the trend of % conversion for each sample

There is no visible trend in the conversions of the samples in both the dark and under UV irradiation, in contrast to the samples containing UiO-66. It seems as though the TTiP is not promoting the base catalyzed reaction of the UiO-66 $NH_{2,}$ and in this case the MOF alone produces the highest percent conversion of methyl paraoxon to nitrophenoxide in 120 min. In the dark the UiO-66 NH_2 is the most effective, where as in the presence of UV light the polymer composite containing the MOF has the high conversion. It should also be noted that the polymer composite sample containing the MOF was not affected by the source of irradiation. It again is proposed that there are potentially two competing mechanisms in the light and the dark, as well as the polymer composite fibers containing UiO-66 NH_2 produce a product other than nitrophenoxide. In the light the dominant product does not absorb in the UV-Vis region, and therefore is untraceable via UV-Vis spectroscopy. This would explain the low conversions seen for the polymer composite fibers in **Table 3-4.**

The catalyst PMMA/TTiP/UiO-66 NH_2 was introduced to the same reaction conditions used in degradations in the dark and UV irradiation. Instead of using a quartz vial to ensure the penetration of the UV light into the catalyst a pyrex glass vial was used. This will filter out the UV region of the irradiation result in only visible light reaching to the catalyst.

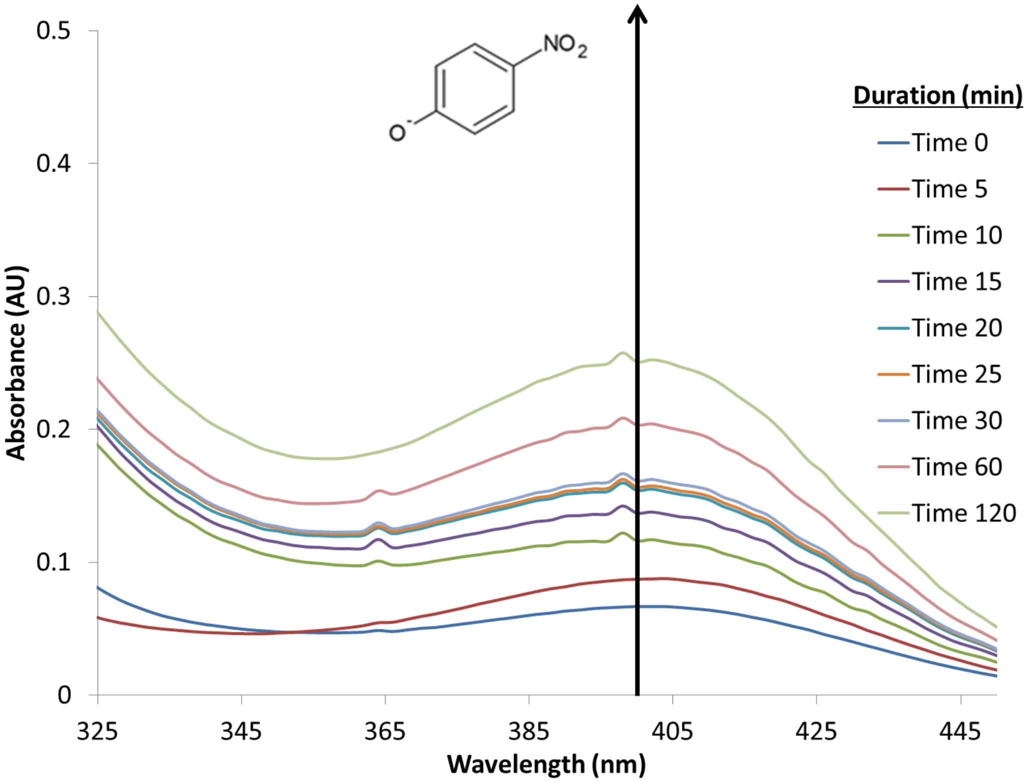

Figure 3-29. UV-Vis spectra of the degradation of methyl paraoxon with PMMA/TTiP/UiO-66 NH_2 with Visible irradiation.

What was seen was unexpected; the conversion from methyl paraoxon to nitro phenoxide was only 31.8 %, compared to 71.8 % with UV irradiation, **Figure 3-29**. In addition, a blue shift in maximum absorbance was observed, to 400 nm from of 407 nm typically seen in previous degradations with methyl paraoxon. Further analysis is necessary to determine the kinetics and the order of the reaction and to draw any definitive conclusions.

3.3.3.2 Kinetic Data

Due to the observations seen with differing of rate orders in the dark and light with samples containing UiO-66, the same approach was taken to calculated the rate order and initial rate constant of the samples containing UiO-66 NH_2 that were exposed to light and in the dark.

Sample	Dark		UV Light	
	Rate Order	**Initial Rate Constant**	**Rate Order**	**Initial Rate Constant**
PMMA/TTiP/UiO-66 NH_2	2nd	0.0264	2nd	0.0198
PMMA/UiO-66 NH_2	2nd	0.0163	2nd	0.0079
UiO-66 NH_2	2nd	0.0682	2nd	0.0053

Table 3-5. Table comparing rate order and initial rate constant of methyl paraoxon degradation reactions in the dark and in UV light with polymer composite samples containing UiO-66 NH_2

Polymer composite samples containing UiO-66 NH_2 showed a second-order rate in both the dark and when exposed to UV irradiation. The rate constant of these samples is consistent with the percent conversion. The reaction using only MOF had the fastest reaction rate compared to the polymer composites. However, when the same samples are subjected to UV light their rate order remains the same but the rate constant approximately halves. The resulting data can be seen in **Table 3-5**. This again is consistent with the theory of competing mechanisms that are producing reaction products that do not absorb in the UV-visible region of the electromagnetic spectrum.

Literature reports state that the presence of the amine functional group can shift the absorbance of the MOF into the visible region being useful for visible initiated photocatalysis. PMMA/TTiP/UiO-66 NH_2 visible light and UV light degradation results were compared and results can be seen in **Table 3-6**.

Sample	**Visible Light**		**UV Light**	
	Rate Order	**Initial Rate Constant**	**Rate Order**	**Initial Rate Constant**
PMMA/TTiP/UiO-66 NH_2	2nd	0.0032	2nd	0.0198

Table 3-6. Table comparing rate order and initial rate constant of methyl paraoxon degradation reactions in visible and in UV light with PMMA/TTiP/UiO-66 NH_2

The same UV lamp source was used in the experiments with visible irradiation. The reaction was carried out in a Pyrex glass therefore, filtering out the UV and only allowing visible light to penetrate the sample. There are several reasons for why the rate constant and conversion are drastically different. The initial hypothesis was that there should be no change in the rate constant and conversion by just changing the reaction vessel. This is because if the polymer/MOF catalyst is activated by visible light, this was reaching the sample regardless of the vial composition. Results proved this hypothesis to be false. There was a six-fold decrease in reaction rate with visible light compared to the UV.

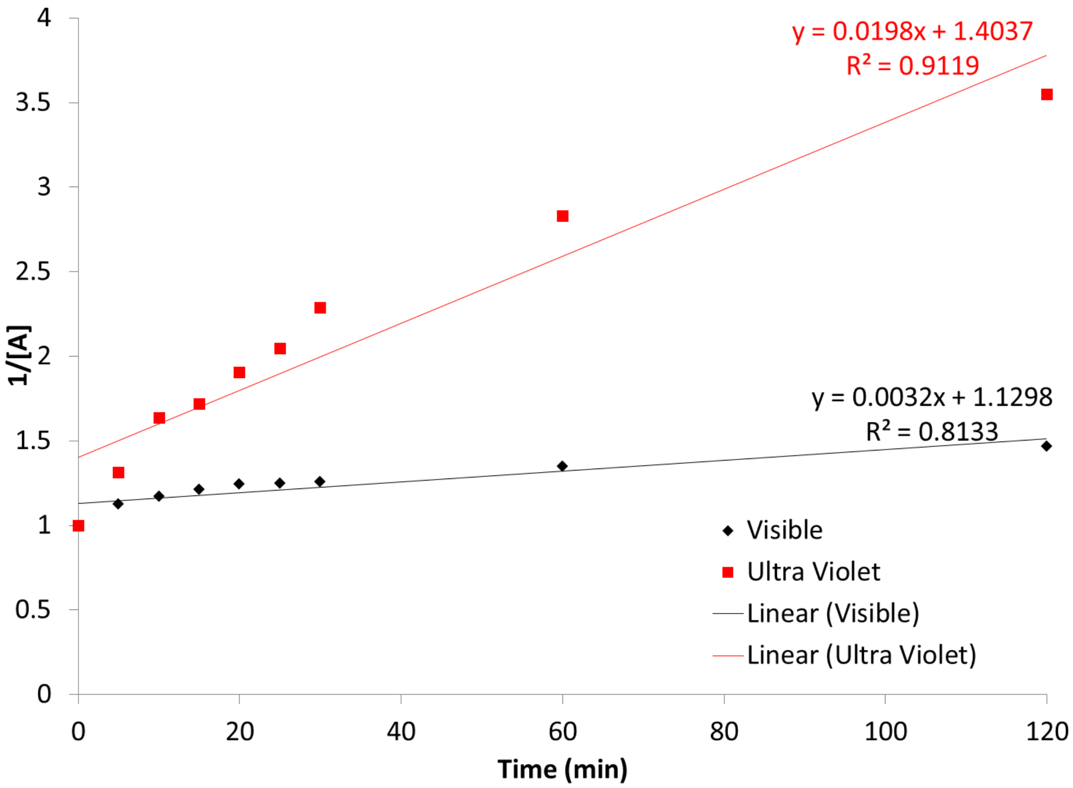

Figure 3-30. Rate plot of methyl paraoxon degradation with PMMA/TTiP/UiO-66 NH_2 with visible irradiation (black) and UV irradiation (red)

When analyzing the second-order rate plot for the samples in the visible and the UV it is seen in **Figure 3-30** that the sample subjected to UV light has a better fit to the linear trend, whereas the visible sample seems to possess a more logarithmic fit. This again supports the conclusion that different potential mechanisms that are dependent on the wavelength of irradiation.

3.3.3 Degradation of Methyl Paraoxon with TiO_2/UiO-66 Fibers

3.3.3.1 Light vs. Dark

Fabricated and characterized nanofibers were used in a series of methyl paraoxon degradations. Fibers were exposed to both light and dark conditions under the Jones group parameters for degradation as previously described. The resulting data was evaluated and shown in **Table 3-7 and Figure 3-31**.

	Dark	**Light**
% Conversion	45.9	24.6
Rate Order	1st	2nd
Rate Constant	0.0049 M·min	0.0024 M·min
t½	2.35 h	N/A

Table 3-7. Degradation of methyl paraoxon with TiO_2/UiO-66 nanofibers. Comparison of light vs. dark degradation and the percent conversion, rate order, rate constant and half-life deduced.

In the dark the conversion and half-life are low and longer, respectively, then what we have seen in the past with other methyl paraoxon degradations. When the data acquired in the light was analyzed we see that the conversion is half of what is seen in the dark. Further calculations led to the determination of a second-order reaction in the light.

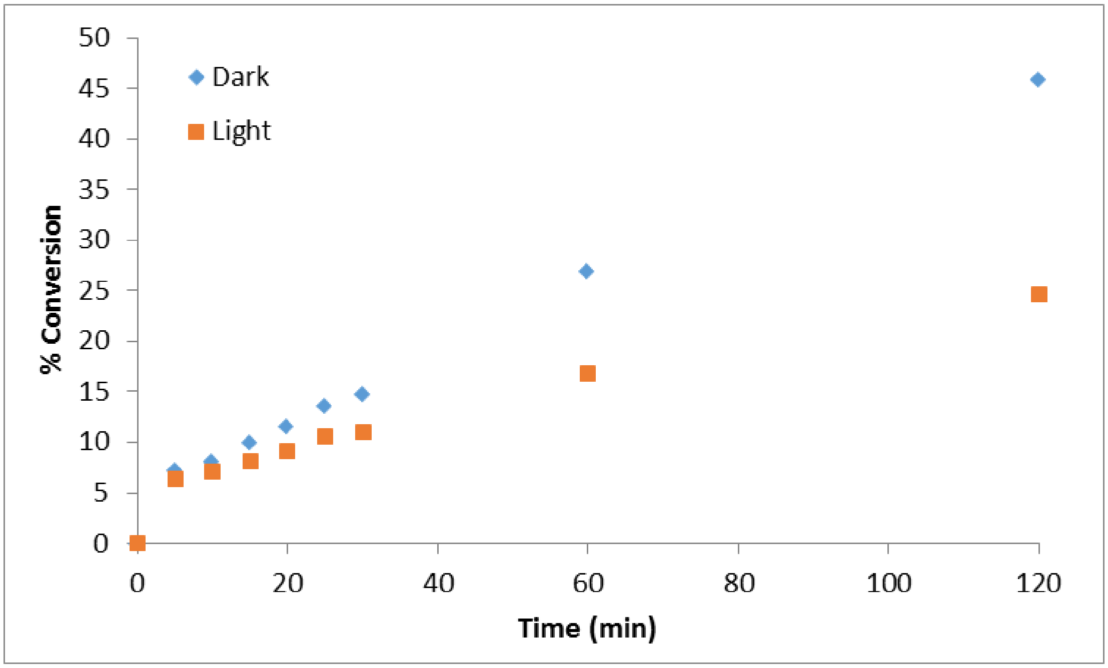

Figure 3-31. Time v. % Conversion of light v. dark degradation of methyl paraoxon with TiO_2 /UiO-66 nanofibers.

The results further support the theory of multiple reaction mechanism and explain the variations in conversion and the order of the reaction. As mentioned in earlier Chapter 2, TiO_2 exploits reactive radical species to initiate the degradation process. In **Figure 3-31** it is seen the conversion is almost halved in the presence of UV irradiation. The radical species produced are potentially forming non UV-Visible absorbing species, and therefore cannot be detected by UV-Vis spectroscopy.

3.4 Conclusions

Electrospun polymer composite fibers containing UiO-66 and UiO-66 NH_2 were successfully fabricated from a sol-gel solution. Synthesized fibers were characterized using an assortment of analytical techniques, and the structural integrity of the MOF was maintained during the electrospinning process. The resulting composite fibers were used in the successful degradation of methyl paraoxon showing enhanced efficiency.

Photocatalytic degradations of methyl paraoxon with UiO-66 incorporated into PMMA/TTiP fibers aimed to demonstrate whether addition of a MOF to a polymer composite matrix of fibers would increase the degradation efficiency. It was concluded that the presence of the TTiP and UiO-66 increased conversion and lowered the half-life of the reaction. Results acquired are the best to date in comparison with literature values. Composite fibers containing MOF were also exposed to UV irradiation. Results showed lower conversions and longer half-lives. This led to the conclusion of multiple degradation mechanisms dependent on the irradiation used to drive the reaction. The dark reaction is base catalyzed and undergoes a hydrolysis mechanism. However, in the light, UV radiation produces photo-induced electron hole pairs, which in turn produce reactive radical species and will degrade the targeted pollutant resulting in products that do not possess an absorbance in the UV-Vis region of the electromagnetic spectrum.

UiO-66 NH_2 was incorporated into PMMA/TTiP fibers with the aim of determining whether the functionalization of the UiO-66 would further enhance the degradation efficiency seen in the polymer composite fibers containing UiO-66. It was concluded that the presence of the amine functional group did not enhance the rate of degradation. Degradations of various composites both with and without MOF were conducted in the dark, UV, and visible light, results showed no consistent trend in conversions. However, depending on light source, there were drastic variations in percent conversion and rate. This strengthened the conclusion of multiple mechanistic degradation pathways. The kinetics of the degradations of methyl paraoxon with polymer/MOF composite fibers are complicated and require additional analyses before further conclusions can be made.

3.5 References

1. Schneider, J.; Matsuoka, M.; Takeuchi, M.; Zhang, J.; Horiuchi, Y.; Anpo, M.; Bahnemann, D. W., Understanding TiO2 Photocatalysis: Mechanisms and Materials. *Chemical Reviews* **2014,** *114* (19), 9919-9986.

2. Choi, S. K.; Kim, S.; Lim, S. K.; Park, H., Photocatalytic Comparison of TiO2 Nanoparticles and Electrospun TiO2 Nanofibers: Effects of Mesoporosity and Interparticle Charge Transfer. *The Journal of Physical Chemistry C* **2010,** *114* (39), 16475-16480.

3. Obuya, E. A.; Joshi, P. C.; Gray, T. A.; Keane, T. C.; Jones, W. E., Jr., Application of Pt.TiO2 nanofibers in photosensitized degradation of rhodamine B. *International Journal of Chemistry* **2014,** *6* (1), 1-16.

4. Wagner, G. W.; Chen, Q.; Wu, Y., Reactions of VX, GD, and HD with Nanotubular Titania. *The Journal of Physical Chemistry C* **2008,** *112* (31), 11901-11906.

5. Wagner, G. W.; Peterson, G. W.; Mahle, J. J., Effect of Adsorbed Water and Surface Hydroxyls on the Hydrolysis of VX, GD, and HD on Titania Materials: The Development of Self-Decontaminating Paints. *Industrial & Engineering Chemistry Research* **2012,** *51* (9), 3598-3603.

6. Wagner, G. W.; Procell, L. R.; Munavalli, S., 27Al, 47,49Ti, 31P, and 13C MAS NMR Study of VX, GD, and HD Reactions with Nanosize Al2O3, Conventional Al2O3 and TiO2, and Aluminum and Titanium Metal. *The Journal of Physical Chemistry C* **2007,** *111* (47), 17564-17569.

7. Reneker, D.; Chun, I., Nanometre diameter fibres of polymer, produced by electrospinning. *Nanotechnology* **2003,** *7* (3), 216.

8. Dong, H.; Nyame, V.; MacDiarmid, A. G.; Jones; Jr., W. E., Polyaniline/poly(methyl methacrylate) coaxial fibers: The fabrication and effects of the solution properties on the morphology of electrospun core fibers. *Journal of Polymer Science Part B: Polymer Physics* **2004,** *42* (21), 3934-3942.

9. He, J.-H.; Wu, Y.; Zuo, W.-W., Critical length of straight jet in electrospinning. *Polymer* **2005,** *46* (26), 12637-12640.

10. Frank Agyemang, O.; Faheem, A. S.; Richard, A.-N.; Xinsheng, Y.; Hern, K., A Simple Method of Electrospun Tungsten Trioxide Nanofibers with Enhanced Visible-light Photocatalytic Activity. *Nano-Micro Letters* **2015,** *7* (?).

11. Wang, G.; Ji, Y.; Huang, X.; Yang, X.; Gouma, P.-I.; Dudley, M., Fabrication and Characterization of Polycrystalline WO3 Nanofibers and Their Application for Ammonia Sensing. *The Journal of Physical Chemistry B* **2006,** *110* (47), 23777-23782.

12. Dharani, S.; Mulmudi, H. K.; Yantara, N.; Thu Trang, P. T.; Park, N. G.; Graetzel, M.; Mhaisalkar, S.; Mathews, N.; Boix, P. P., High efficiency electrospun TiO2 nanofiber based hybrid organic-inorganic perovskite solar cell. *Nanoscale* **2014,** *6* (3), 1675-1679.

13. Lee, J.; Farha, O. K.; Roberts, J.; Scheidt, K. A.; Nguyen, S. T.; Hupp, J. T., Metal-organic framework materials as catalysts. *Chemical Society Reviews* **2009,** *38* (5), 1450-1459.

14. DeCoste, J. B.; Weston, M. H.; Fuller, P. E.; Tovar, T. M.; Peterson, G. W.; LeVan, D. M.; Farha, O. K., Metal-Organic Frameworks for Oxygen Storage. *Angewandte Chemie International Edition* **2014,** *53* (51), 14092-14095.

15. DeCoste, J. B.; Peterson, G. W., Metal–Organic Frameworks for Air Purification of Toxic Chemicals. *Chemical Reviews* **2014,** *114* (11), 5695-5727.

16. Kreno, L. E.; Leong, K.; Farha, O. K.; Allendorf, M.; Van Duyne, R. P.; Hupp, J. T., Metal–Organic Framework Materials as Chemical Sensors. *Chemical Reviews* **2012,** *112* (2), 1105-1125.

17. Corma, A.; García, H.; Llabrés i Xamena, F. X., Engineering Metal Organic Frameworks for Heterogeneous Catalysis. *Chemical Reviews* **2010,** *110* (8), 4606-4655.

18. DeCoste, J. B.; Peterson, G. W.; Schindler, B. J.; Killops, K. L.; Browe, M. A.; Mahle, J. J., The effect of water adsorption on the structure of the carboxylate containing metal-organic frameworks Cu-BTC, Mg-MOF-74, and UiO-66. *Journal of Materials Chemistry A* **2013,** *1* (38), 11922-11932.

19. DeCoste, J. B.; Peterson, G. W.; Jasuja, H.; Glover, T. G.; Huang, Y.-g.; Walton, K. S., Stability and degradation mechanisms of metal-organic frameworks containing the Zr6O4(OH)4 secondary building unit. *Journal of Materials Chemistry A* **2013,** *1* (18), 5642-5650.

20. Peterson, G. W.; Moon, S.-Y.; Wagner, G. W.; Hall, M. G.; DeCoste, J. B.; Hupp, J. T.; Farha, O. K., Tailoring the Pore Size and Functionality of UiO-Type Metal–Organic Frameworks for Optimal Nerve Agent Destruction. *Inorganic Chemistry* **2015,** *54* (20), 9684-9686.

21. Moon, S.-Y.; Wagner, G. W.; Mondloch, J. E.; Peterson, G. W.; DeCoste, J. B.; Hupp, J. T.; Farha, O. K., Effective, Facile, and Selective Hydrolysis of the Chemical Warfare Agent VX Using Zr6-Based Metal–Organic Frameworks. *Inorganic Chemistry* **2015,** *54* (22), 10829-10833.

22. Mondloch, J. E.; Katz, M. J.; Isley, W. C., III; Ghosh, P.; Liao, P.; Bury, W.; Wagner, G. W.; Hall, M. G.; De Coste, J. B.; Peterson, G. W.; Snurr, R. Q.; Cramer, C. J.; Hupp, J. T.; Farha, O. K., Destruction of chemical warfare agents using metal-organic frameworks. *Nat. Mater.* **2015,** *14* (5), 512-516.

23. Katz, M. J.; Mondloch, J. E.; Totten, R. K.; Park, J. K.; Nguyen, S. T.; Farha, O. K.; Hupp, J. T., Simple and Compelling Biomimetic Metal–Organic Framework Catalyst for the Degradation of Nerve Agent Simulants. *Angewandte Chemie International Edition* **2014,** *53* (2), 497-501.

24. Shen, L.; Wu, W.; Liang, R.; Lin, R.; Wu, L., Highly dispersed palladium nanoparticles anchored on UiO-66(NH2) metal-organic framework as a reusable and dual functional visible-light-driven photocatalyst. *Nanoscale* **2013,** *5* (19), 9374-9382.

25. Kandiah, M.; Usseglio, S.; Svelle, S.; Olsbye, U.; Lillerud, K. P.; Tilset, M., Post-synthetic modification of the metal-organic framework compound UiO-66. *Journal of Materials Chemistry* **2010,** *20* (44), 9848-9851.

26. Shen, L.; Liang, S.; Wu, W.; Liang, R.; Wu, L., Multifunctional NH2-mediated zirconium metal-organic framework as an efficient visible-light-driven photocatalyst for selective oxidation of alcohols and reduction of aqueous Cr(vi). *Dalton Transactions* **2013,** *42* (37), 13649-13657.

27. Raushel, F. M., Chemical biology: Catalytic detoxification. *Nature* **2011,** *469* (7330), 310-311.

28. Astruc, D.; Lu, F.; Aranzaes, J. R., Nanoparticles as Recyclable Catalysts: The Frontier between Homogeneous and Heterogeneous Catalysis. *Angewandte Chemie International Edition* **2005,** *44* (48), 7852-7872.

29. Rastogi, V. K.; Defrank, J. J.; Cheng, T.-c.; Wild, J. R., Enzymatic Hydrolysis of Russian-VX by Organophosphorus Hydrolase. *Biochemical and Biophysical Research Communications* **1997,** *241* (2), 294-296.

30. Kim, K.; Tsay, O. G.; Atwood, D. A.; Churchill, D. G., Destruction and Detection of Chemical Warfare Agents. *Chemical Reviews* **2011,** *111* (9), 5345-5403.

31. Li, P.; Klet, R. C.; Moon, S.-Y.; Wang, T. C.; Deria, P.; Peters, A. W.; Klahr, B. M.; Park, H.-J.; Al-Juaid, S. S.; Hupp, J. T.; Farha, O. K., Synthesis of nanocrystals of Zr-based metal-organic frameworks with csq-net: significant enhancement in the degradation of a nerve agent simulant. *Chemical Communications* **2015,** *51* (54), 10925-10928.

32. Lange, L. E.; Obendorf, S. K., Degradation studies of methyl parathion with CuBTC metal-organic framework. *Journal of Environmental Chemical Engineering* **2015,** *3* (1), 541-547.

33. Peterson, G. W.; DeCoste, J. B.; Glover, T. G.; Huang, Y.; Jasuja, H.; Walton, K. S., Effects of pelletization pressure on the physical and chemical properties of the metal–organic frameworks Cu3(BTC)2 and UiO-66. *Microporous and Mesoporous Materials* **2013,** *179*, 48-53.

34. Mahshid, S.; Askari, M.; Ghamsari, M. S., Synthesis of TiO2 nanoparticles by hydrolysis and peptization of titanium isopropoxide solution. *Journal of Materials Processing Technology* **2007,** *189* (1–3), 296-300.

35. Cavka, J. H.; Jakobsen, S.; Olsbye, U.; Guillou, N.; Lamberti, C.; Bordiga, S.; Lillerud, K. P., A New Zirconium Inorganic Building Brick Forming Metal Organic Frameworks with Exceptional Stability. *Journal of the American Chemical Society* **2008,** *130* (42), 13850-13851.

CHAPTER 4: Ag Deposition on Electrospun TiO_2 Nanofibers for Visible Plasmon-Exciton Coupling in Nanocomposite Catalysts.

4.1 Introduction

In the past decade, plasmonics have inspired a significant amount of interest in various research communities for applications in nanophotonics, optics, catalysis, and energy conversion. Materials possessing surface plasmon resonances (SPR) such as silver nanoparticles have been studied and are known to exhibit appealing optical characteristics.[1] SPR can be described as the resonance between collective oscillations of conductive electrons at or near the surface of metallic nanostructures (often noble metals), and an incident electromagnetic field. The size and shape of the metallic nanoparticles dictates the magnitude and wavelength at which the resonance occurs. These resonances have been exploited for applications such as catalysis, sensors, and optical devices.[2]

Cyanine dyes are another class of materials that possesses photo sensitization properties useful in enhancing energy conversion. When introduced to certain conditions in solutions the dye monomer will aggregate producing a more narrow absorption band that is bathochromically shifted compared to the absorption of the monomer, these are known as J-aggregates.[3] Within these aggregates systems is an exciton that forms when a photon is absorbed. The resulting excited state may be described by the Frenkel exciton theory which describes an excited state electron-hole pair that is localized to one atom/molecule within a crystal lattice. The exciton can propagate by hopping through the lattice; however the electron-hole remains tightly bound.

The coupling of plasmonic resonance with excitonic resonance has been shown to produce unique optical properties such as Fano resonance, induced transparency, and enhanced fluorescence.[4] Through coupling of the excitonic J- aggregate dye and plasmonic NPs an overlapping of resonance occurs which in turn generates an induced transparency. These transparencies may be light scattering based phenomenon in which the background and scattered light interferes and produces a “dip” in the spectra. This phenomenon is often termed a Fano resonance, **Figure 4-1**.

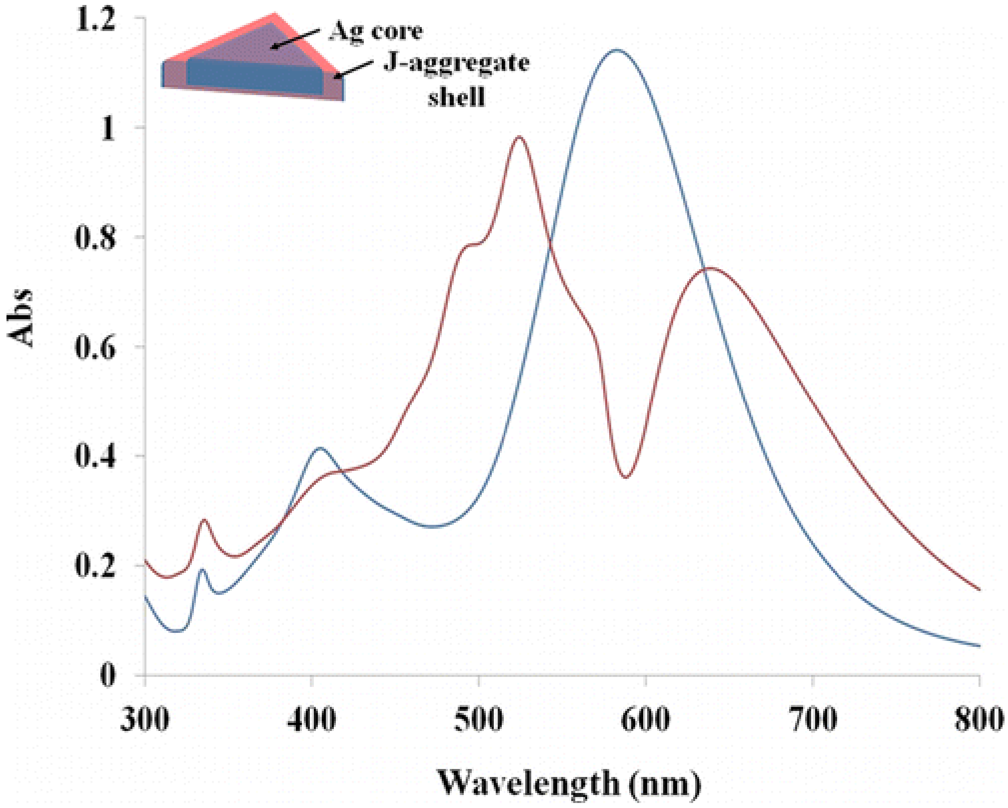

Figure 4-1. Absorption spectra of plasmon-exciton coupling is adapted from DeLacy, B., et. al,*Nano Letters* **2015,** *15* (4), 2588-2593 (right) The blue curve is Ag nanoplatelets in water and the red curve is the J-aggregate coated nanoplatelets. An induced transparency is observed in the red curve.

Alternatively, the transparencies may be an absorption based phenomenon in which the transparency dip is attributed to the overlap of two absorption dominant resonances, which lead to the generation of two new energy states. A transparency, or diminished absorption, is observed between these two energy states. In both scenarios, the overlap of plasmon and exciton resonance have been shown to significantly enhance the near electromagnetic field.[4,5] Recent work done by Norlander, Halas et al. showed an enhancement in fluorescence using nanomatryoshkas (another Fano resonant structure) composed of Au and SiO_2 layers.[6]

Photocatalytic semiconductors such as TiO_2 have been well documented in the literature.[7] Photocatalysts possess the ability to absorb incident irradiation in the UV or visible region of the spectrum promoting an electron from the valence band to the conduction band of a semiconductor creating an electron hole pair. These photoinduced charge carriers can react with surface adsorbed species to form oxidizing and reducing species, as well as reactive radicals; i.e, hydroxyl and superoxide radicals. Once formed, these photochemical products can degrade chemicals that are adsorbed on the surface of the TiO_2 or diffuse to catalytically active sites at the semiconductor/ liquid interface during the lifetime of the exciton.

TiO_2 is an appealing semiconductor photocatalyst; however it has limited use in solar applications due to the fact that only the UV region of the solar spectrum (about 5%) is absorbed owing to its large band gap energy. A number of efforts on surface modification have been made to improve visible light driven photocatalysis. Through the doping of a metal into an active photocatalyst such as TiO_2 with large band gap energies, the metal will create a donor or acceptor level within the conduction band and valence band of the semiconductor, by developing a new photocatalyst.[8] Various metal nanoparticles, such as Cr, Sb[8], Au[9], Ag, Pt[10]; and rare earth metals including La, Ce, Er, Pr, Gd, Nb, and Sm[11], have been employed in visible-light driven photocatalysis. Ag has been coupled with TiO_2 to utilize the benefits of the silvers SPR, which is the collective free electron charge oscillation in the metallic nanoparticles that are excited by visible light.[12]

Through coupling plasmonic and excitonic structures there can be a further enhancement of the charge injection from a J-aggregate dye to a semiconductor than seen with one or the other alone. The impact of plasmon-exciton coupling on the catalysis of the titania will subsequently be determined. These nanocomposites are unique in that they effectively couple both light harvesting and catalytic functions in one material. The charge transfer process is highly dependent on the structure of the material, dynamics and chemical properties of the interfacial region, surface coverage, and bonding. For charge injection to occur it is imperative that the plexciton has an excited state energy level that is higher than the -4.2 eV level of the TiO_2 conduction band. In addition, by ensuring that the plasmonic absorption is lower in energy than the 3.2 eV band gap of the TiO_2, the process will effectively occur in the visible region of the electromagnetic spectrum, **Figure 4-2**.

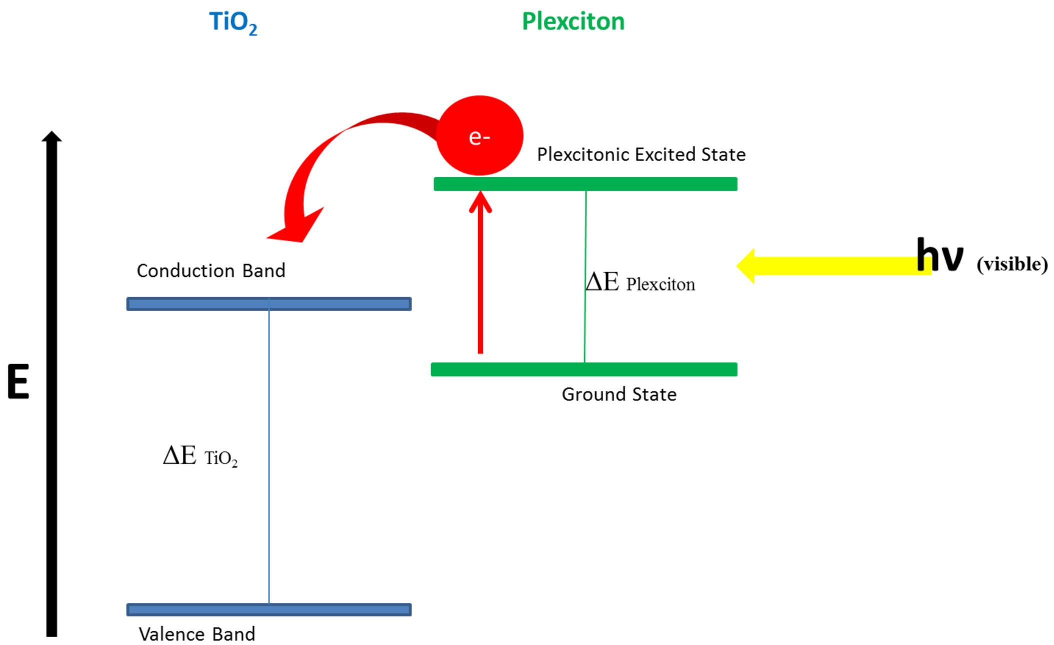

Figure 4-2. Proposed mechanism of electron injection from the plexcitonic material into the TiO_2 conduction band.

In this Chapter, the deposition of Ag nanoparticles on the surface of electrospun TiO_2 nanofibers is discussed, and preliminary degradation results are presented for methyl paraoxon with the metal/semiconductor fibrous material in the light and dark.

4.2 Experimental

4.2.1 Materials

Polymethylmethacrylate (PMMA) (M_w960,000), titanium (IV) isopropoxide (TTiP), N,N-dimethylformamide (DMF), chloroform and *O*-(4-nitrophenyl) phosphate (methyl paraoxon, DMNP) (M_w247.14) 4-ethylmorpholine (M_w115.17), Silver nitrate ($AgNO_3$), acetone, ethylene glycol (EG), polyvinyl pyrrolidone (PVP) were purchased from Sigma Aldrich and used without further purification.

4.2.2 Synthesis of TiO_2 Nanofibers

TiO_2 nanofibers were fabricated by electrospinning a sol-gel precursor solution followed by a thermal treatment. A sol gel solution in a 1:2 ratio of PMMA to TTiP was prepared in a 1:1 ratio of chloroform and N,N-dimethylformamide. Where 320 mg of PMMA was dissolved in 2 mL of chloroform and allowed to stir until all polymer was dissolved. An aliquot of 0.67 mL of TTiP was added dropwise to the polymer solution and allowed to stir for an additional 30 min. Subsequently, 2 mL of DMF was added to the solution to increase the dielectric constant and stirred for an additional 2 h prior to electrospinning. A Spellman SL 30 generator was used to apply 25kV/cm across the sol gel polymer solution resulting in the deposition of nanofibers on the electrically charged collector. A schematic of the electrospinning apparatus can be seen in **Figure 2-2**. The resulting polymer composite nanofibers were left to stand for 12 h at room temperature under ambient conditions. This allowed for complete hydrolysis of TTiP to $Ti(OH)_4$ and then further condensation to amorphous TiO_2 prior to thermal treatment.[13] The fibers were then collected and calcined in a Thermo Scientific Lindberg Blue M Mini-Mite Tube Furnace, 16-Pt; 120V tube furnace at 400 °C for 4 h under atmospheric conditions.

4.2.3 Metal Deposition, Polyol Synthesis

To deposit Ag nanoparticles on the surface of TiO_2 nanofibers, 100 mg of electrospun TiO_2 nanofibers and 20 mL EG were initially added into a 3-neck flask (fitted with a reflux condenser and a Teflon-coated stir bar) and heated at 160 °C. After 30 min of stirring at 160 °C, 5 mL of $AgNO_3$ solution which consisted of 10 mg of Ag NO_3 in 5 mL of ethylene glycol (EG), and 5 mL of polyvinyl pyrrolidone (PVP) solution which consisted of 100 mg of PVP in 5mL of EG were dripped (simultaneously) into the 3-necked flask over a period of 10 min. The mixture was continuously heated to 160 °C for an additional 20 min. The resulting solution was then centrifuged and decanted to remove the excess solution. The Ag-TiO_2 was washed thoroughly acetone to remove EG and excess PVP before further use. The fibers were allowed to dry at room temperature before use.

4.2.4 Methyl Paraoxon Degradation Procedure

All degradation experiments were carried out at room temperature. A 3 mg sample of Ag-TiO_2 was introduced to an aqueous solution of N-ethyl morpholine (1 mL). The mixture was continuously stirred over the course of the experiment (2 h). To the dispersed suspension 4 μL of methyl paraoxon (5.2 mg, 0.021 mmol) was introduced to the solution. Reactions were performed both with and without UV irradiation for comparison. At this point 10 μL aliquots were extracted at over 120 min. Aliquots were diluted to 5 mL with 0.45 M aqueous N-ethylmorpholine and measured using UV-Vis spectroscopy. P- nitrophenoxide was monitored via UV-Visible spectrometry due to its absorbance at 407 nm. Standard control reactions were performed under the same conditions, including the degradation of methyl paraoxon in the presence of TiO_2 nanofibers without Ag.

4.2.5 Characterization Methods

A Spellman SL 30 generator was used to apply a high voltage across the copper wire to create a high electrical potential attaching to the collector. Thermal treatment was carried out using a Thermo Scientific Lindberg Blue M Mini-Mite Tube Furnace, 16-Pt; 120V tube furnace heated to 400 °C for 4 h under atmospheric conditions. Photodegradations used an Oriel 66001 UV lamp with Oriel 68805 40-200 Watt universal Arc lamp power supply, which covers the entire ultra-violet, (100- 400 nm) range. UV-Visible spectrometric analysis of the aliquot was performed using an 8452A Hewlett Packard Diode Array spectrophotometer instrument with a wavelength from 190 to 820 nm, to characterize the absorption spectrum of each aliquot to determine the concentration of the product formation. The morphological and structural characteristics of the nanofibers and nanoparticles were measured by field emission scanning electron microscopy (FESEM, Supra 55 VP from Zeiss equipped with an EDAX energy dispersive X-ray spectroscopy detector), and X-ray diffraction (XRD, PANalytical's X'Pert PRO Materials Research Diffractometer with Cu Kα radiation (λ = 1.5418 Å)), respectively. Transmission electron microscopy (TEM) images were obtained using a JEOL 2010 FETEM instrument. The TEM samples were dispersed in EtOH by sonication and the resulting solution were placed on a lacey carbon grid, which was left in air to evaporate the solvent. Fluorescence and PL measurements were done with a Lumex Ltd. Fluorat-02 spectrometer with excitation wavelength of 300 nm for TiO_2 and excitation wavelengths of 239 and 314 nm for Ag-TiO_2 nanofibers.

4.3 Results and Discussion

4.3.1 Characterization of Ag Deposited TiO_2 Nanofibers

4.3.1.1 Scanning Electron Microscopy and Transmission Electron Microscopy

Electrospun nanofibers nanofibers were investigated by SEM and TEM shown in **Figure 4-3**. SEM image of TiO_2 nanofibers (a) that had been calcined at 400 °C were shown to have an average diameter of approximately 678 nm. The fibers possess a folded and wrinkled surface morphology that was consistent with the TiO_2 nanofibers observed in Chapter 2. TEM imaging (a-1) shows the fibers are made up of small grains and there is no evidence of anything else on the surface of within the fiber. SEM images of the TiO_2 fibers that have undergone a polyol synthesis to deposit Ag on the surface are consistent with the folded and wrinkled surface morphology. However, it is clear the Ag nanoparticle deposition was successful, with evidence of agglomerates that are located on the surface of the fiber.

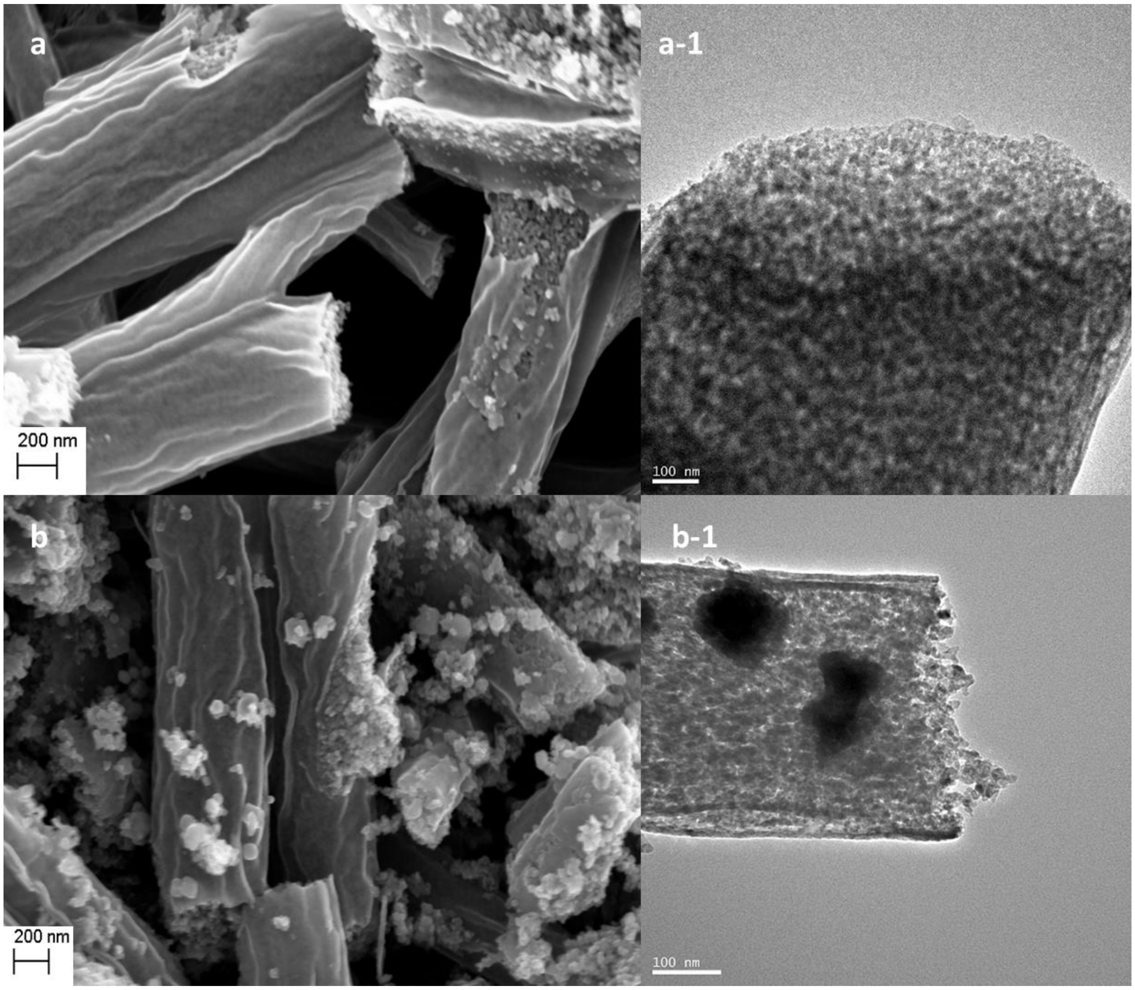

Figure 4-3. SEM image of a) TiO_2 nanofibers calcined at 400°C and b) Ag-TiO_2 nanofibers. TEM images of a-1) TiO_2 and b-1) Ag-TiO_2

TEM analysis showed the appearance of spherical nanoparticles on the surface of the fiber after polyol synthesis, with an average diameter of approximately 153 nm, **Figure 4-3**. The Ag-TiO_2 nanofibers retained an average dimeter of approximately 502 nm. There was a change in the diameter of the fibers pre and post polyol synthesis. The diameter decreases upon deposition of Ag to the nanofiber. It was possible that the long exposure at 160 °C during the polyol synthesis caused the crystal structure to change. According to the literature as the temperature is increased the rutile crystal structure is favored and the diameter of the nanofibers decrease as the rutile fraction is increased.[14]

Therefore, the smaller diameter would be consistent with an increase in rutile fraction. XRD was carried out to confirm this hypothesis, with the results detailed below. EDX was also used in conjunction with SEM to determine the percentage of Ag on the surface of the titania fibers. Results concluded there was a 15:1 ratio of Ti to Ag meaning the sample contains approximately 2% Ag.

4.3.1.2 X-Ray Diffraction

The XRD pattern of post-calcined TiO_2 nanofibers at 400 °C under a ambient atmosphere that have not been deposited with Ag nanoparticles is shown in **Figure 4-4**. Well defined diffraction peaks showed the presence of both anatase and rutile phases. For the anatase phase, the major peaks were obtained at 2θ values of 25.33, 37.93, and 48.07°, corresponding to (101), (004), and (200) planes, respectively. For the rutile phase, peaks were observed at 2θ values of 27.44, 36.12, 41.35, and 54.30°, respectively, representing the Miller indices of (110), (101), (111), and (211) planes, respectively. The fraction of rutile phase was calculated to be 28 wt% from the equation of $W_R=1/[1+0.8(I_A/I_R)]$, where I_A is the X-ray integrated intensities of the (101) reflection of anatase at 2θ of 25.33° and I_R was that of the (110) reflection of rutile at 2θ of 27.44°.

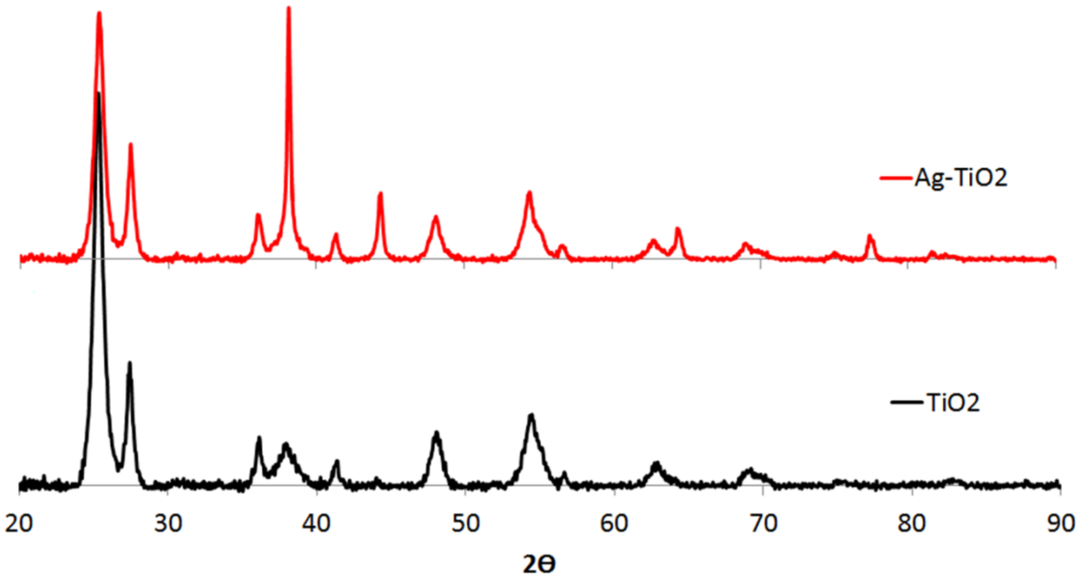

Figure 4-4. XRD diffraction pattern of TiO_2 nanofibers (black) and Ag-TiO_2 nanofibers (red)

The diffraction pattern of Ag-TiO_2 (**Figure 4-4**, red) shows four sharp and well defined diffraction lines at 2θ = 38.13°, 44.36°, 64.39° and 77.39°, which can be assigned to the (111), (200), (220) and (311) reflections of the face centered cubic (fcc) structure of metallic silver, respectively.[15] The 2θ peak seen at 38.13° is also present in the sample of TiO_2, the addition of silver enhanced the intensity of this diffraction line. The fractions of the rutile phase were calculated using of $W_R=1/[1+0.8(I_A/I_R)]$, Ag-TiO_2 nanofibers resulted in a rutile content of 37%. This increased from the rutile percent prior to the polyol synthesis. This change confirms the hypothesis of the heating process during the synthesis affecting the crystal structure of the fibers; regardless of the low temperature the long exposure clearly had an effect on the crystal structure causing the rutile percentage to increase. Evidence of this is clear in the XRD pattern and is consistent with the decrease in diameter of the fibers seen in the SEM images.

Raman spectroscopy was performed to further confirm the structure of TiO_2 was not changed in the presence of Ag nanoparticles. Literature reports clearly state that the deposition of Ag nanoparticles to the surface of TiO_2 in low weight percentages will have no effect on the Raman peaks.[16,17] Analysis of the sample fabricated for this study showed the opposite of what was expected. The TiO_2 containing Ag caused the Raman peaks to either shift or broaden slightly, or new peaks appeared and disappeared. The hypothesis drawn is potential binding of Ag to the TiO_2 structure which in turn would results in different spectra, **Figure 4-5.**

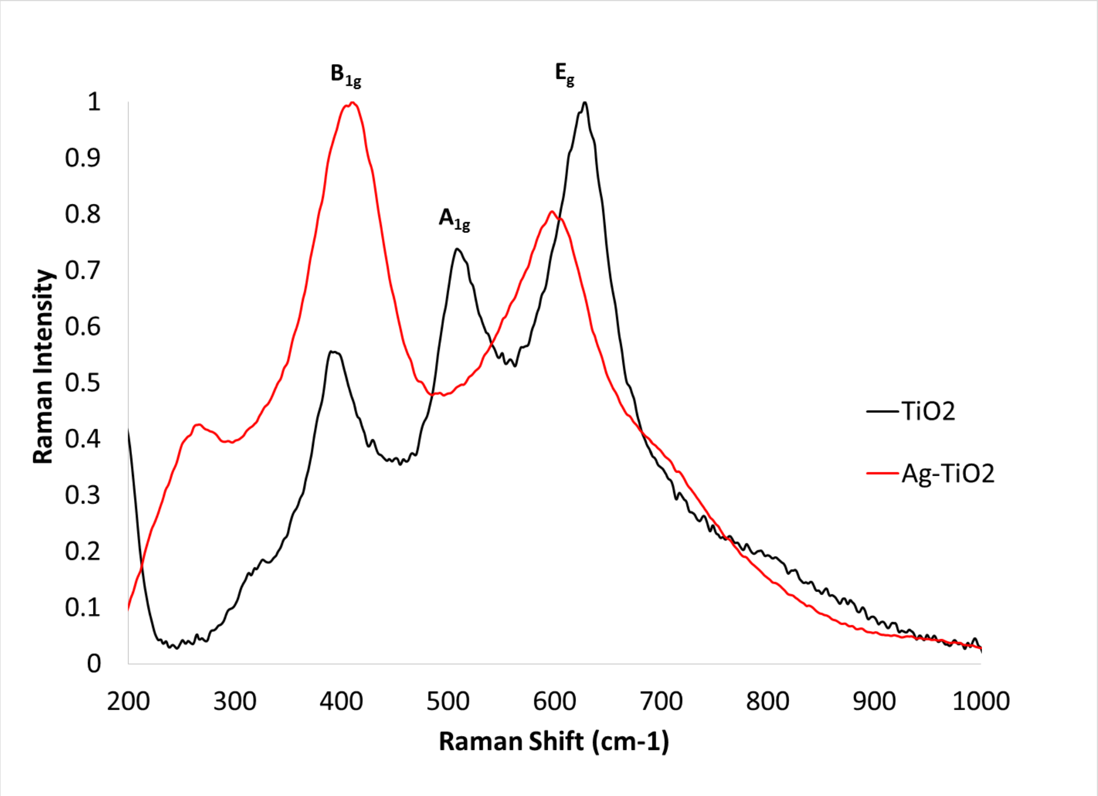

Figure 4-5. Raman spectra of TiO_2 (black) and Ag-TiO_2(red)

4.3.1.3 Spectroscopy Studies

To investigate the photocatalytic activity of Ag-$TiO_{2,}$ solid state UV-Visible, and emission fluorescence experiments were completed. It is presumed that the Ag nanoparticles will act as an electron reservoir and will drew electrons from the conduction band of the TiO_2 via the Mott-Schottky interface. In analysis of the solid state UV-Visible spectra in **Figure 4-6,** the maximum absorbance of Ag-TiO_2 red shifts in comparison to TiO_2. From this, one would conclude that the band gap of the Ag-TiO_2 decreases because of the higher wavelength and lower energy.

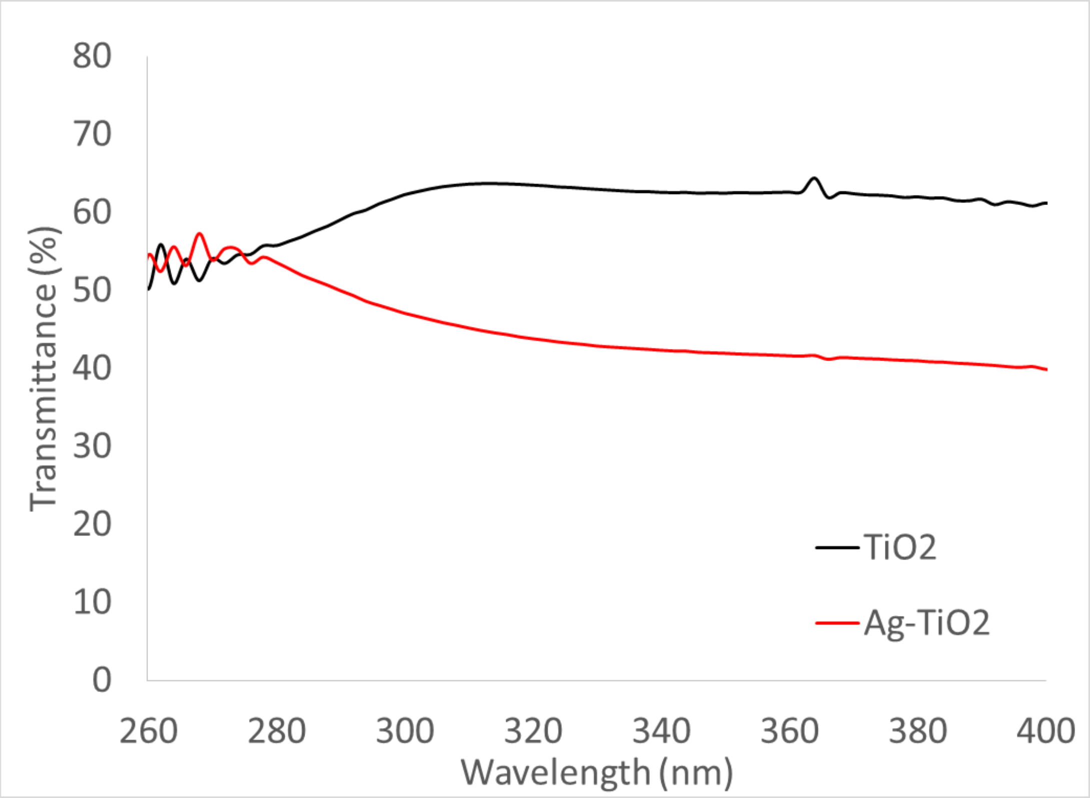

Figure 4-6. Solid state UV-Vis spectra of TiO_2 (black) and Ag-TiO_2 (red)

The fluorescence emission spectra of the nanofibers both with and without Ag were excited at the same wavelength to investigate if there is a change in emission between the samples. In the case of Ag-TiO_2, the broad emission peak seen in the TiO_2 sample (black) between 330 and 430nm disappears. This signifies that the exciting wavelength has changed, as it is no longer receiving emission from the TiO_2. The energy has become too high and it is outside the excitation range limit of the TiO_2, **Figure 4-7.**

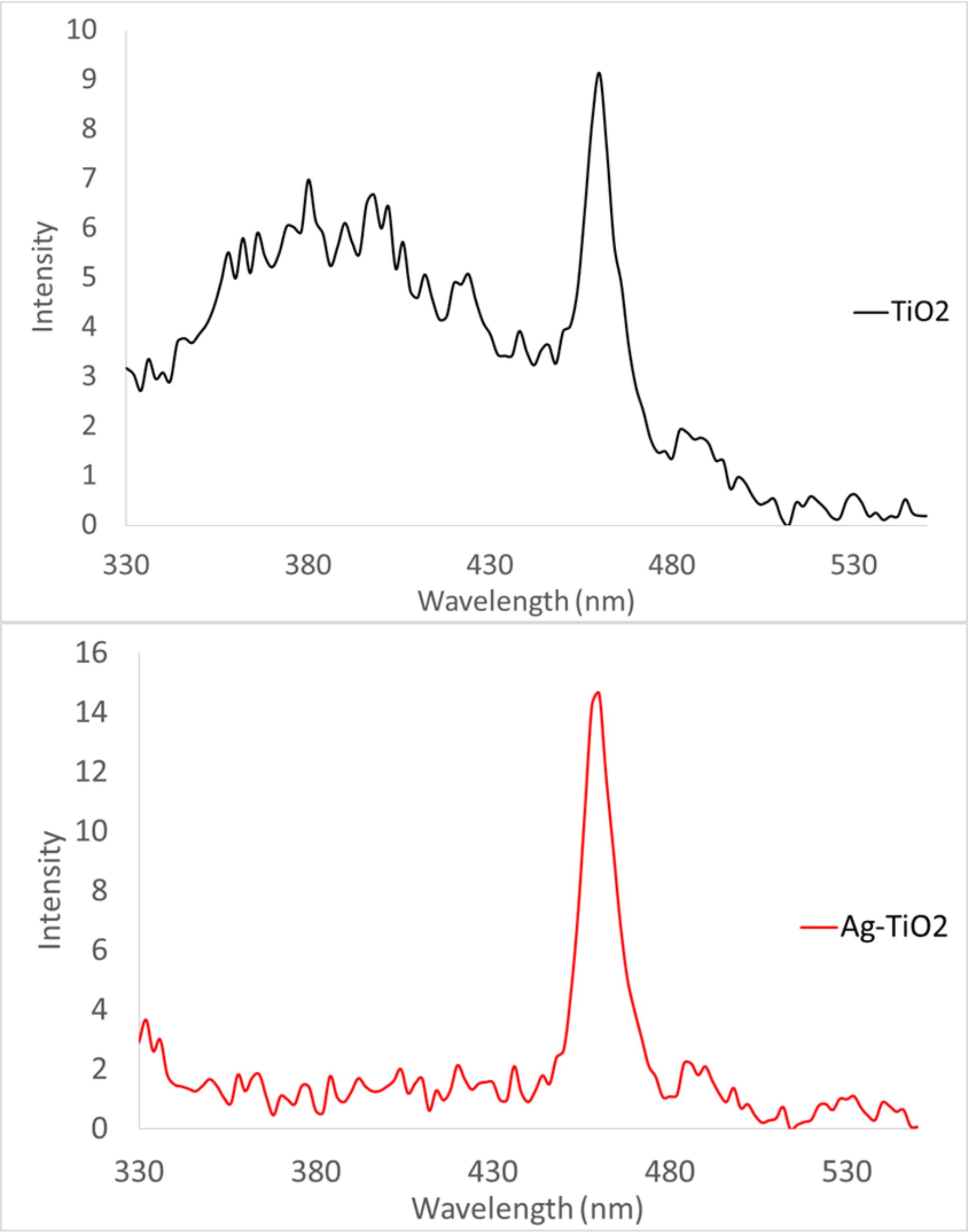

Figure 4-7. Fluorescence emission spectra of TiO_2 (black) and Ag-TiO_2 (red)

Photoluminescence experiments were attempted for both TiO_2 and Ag-TiO_2 nanofibers. The PL emission intensity is related to the recombination of the excited electron-hole pairs. Therefore the lower emission intensity is indicative of a decrease in the rate of recombination.[18,19] Unfortunately, resolved emission was unsuccessful with the streak camera that was utilized, as single-photon counting is necessary.

4.3.2 Photodegradation of Methyl Paraoxon with TiO_2 and Ag-TiO_2

4.3.2.1 Degradation of Methyl Paraoxon in the Dark and with UV Irradiation

TiO_2 and Ag-TiO_2 nanofibers were used to degrade methyl paraoxon in dark and light conditions. TiO_2 nanofibers by themselves showed only a 12-13% conversion in the course of 120 min, regardless of whether it was in the dark or irradiated with UV light. When Ag-TiO_2 was exposed to methyl paraoxon in standard Jones group degradation procedure conditions, a 34.9 % conversion was seen over the course of 120 min. The notable feature here was the minimal change in the parent peak of methyl paraoxon. After 120 min, approximately 65% of the methyl paraoxon remained in solution and the resulting UV spectrum can be seen in **Figure 4-8**.

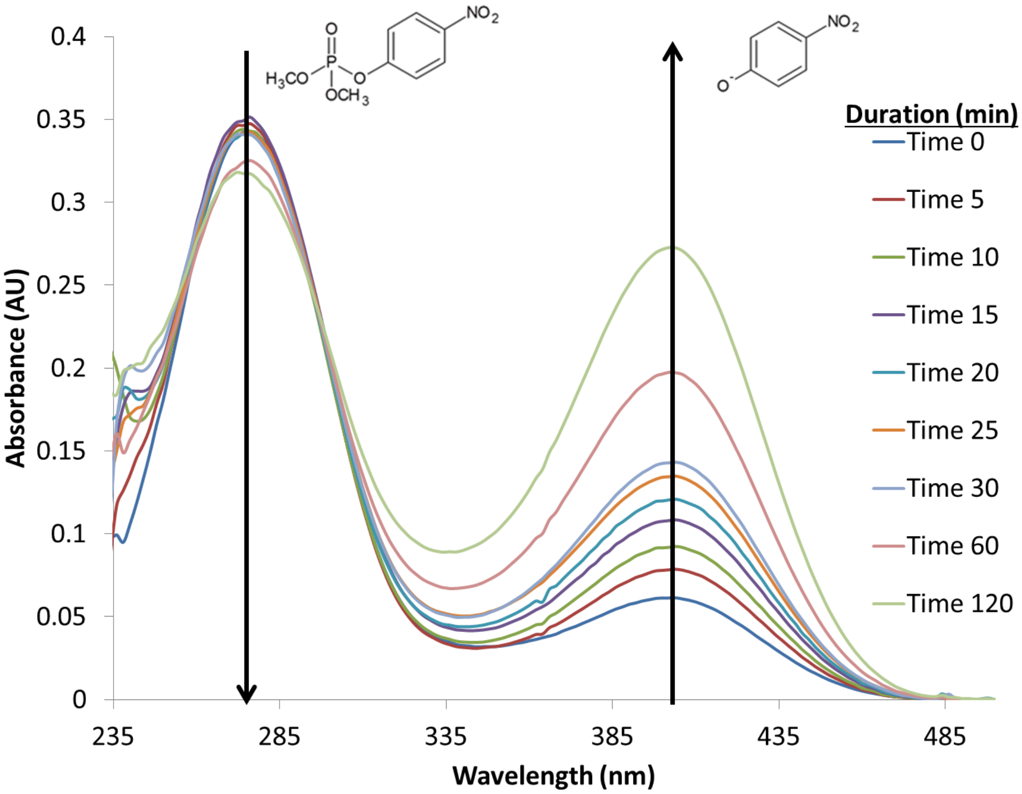

Figure 4-8. UV-Vis spectra of the degradation of methyl paraoxon with Ag-TiO_2 in the dark

When Ag-TiO_2 was exposed to light similar results were seen, with a minimal change in the parent peak and only 23.8% conversion to the nitrophenoxide product. However, in the case of Ag-TiO_2 exposed to light in the last aliquot drawn at 120 min, there is a clear broadening and red shift in the parent peak of methyl paraoxon. It is possible that this could be caused by another product absorbing in the same region as the parent peak. As discussed in pervious Chapters 2 and 3, it is again believed that there could be multiple competing mechanisms which in turn could explain the red shift and peak broadening at 120 min, or it is possible there is a new peak absorbance at 300 nm due to the formation of a new product at absorbs in the UV region,**Figure 4-9**.

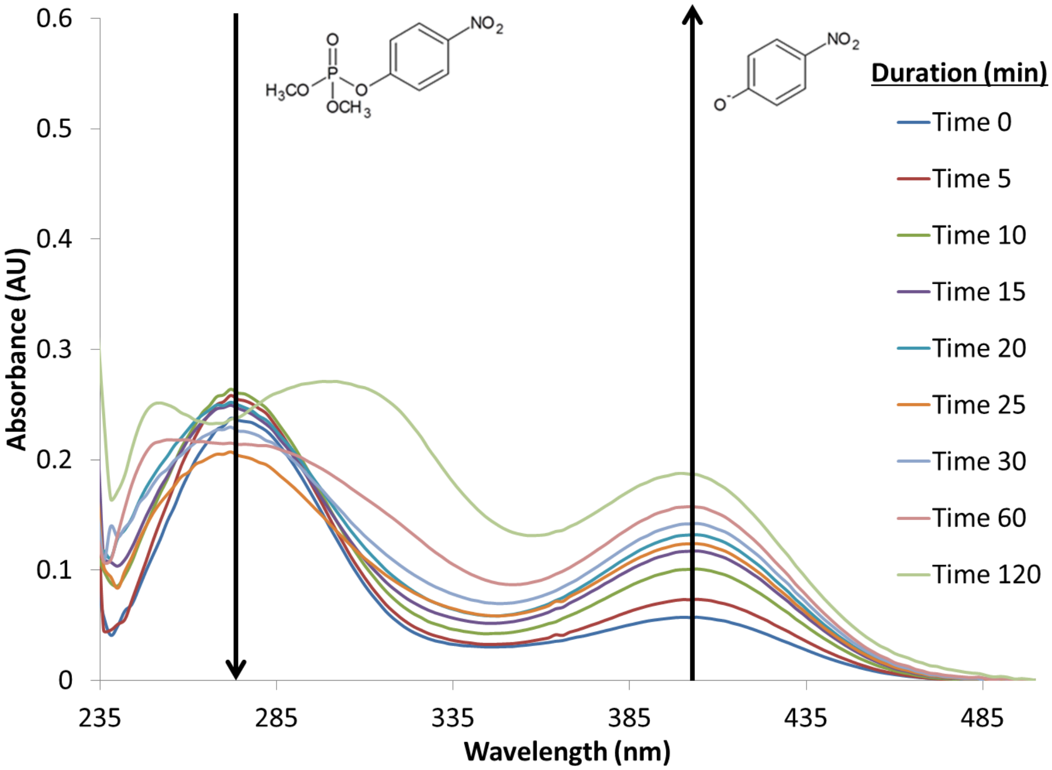

Figure 4-9. UV-Vis spectra of the degradation of methyl paraoxon with Ag-TiO_2 in UV light

Comparison of the nanofiborous samples with and without Ag present results in a fast 7 to 10 % conversion within the first 5 min of exposure to methyl paraoxon. Following the initial 5 min in trials with TiO_2 without Ag, conversion levels off and remains constant regardless of the dark or light conditions. In contrast, the sample trails containing Ag do increase the conversion as time elapses. Ag-TiO_2 without UV irradiation continues to increase in percent conversion throughout the course of the degradation, whereas trails exposed to visible light seems to increase conversion at a much slower rate, **Figure 4-10**.

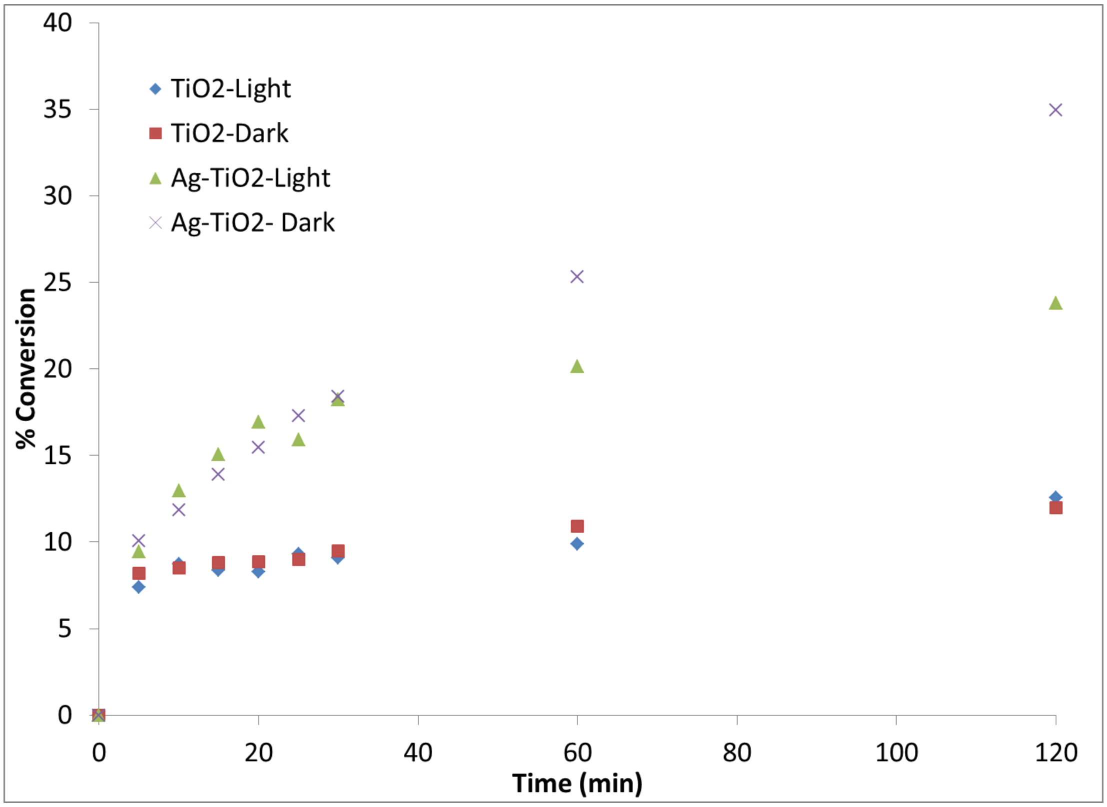

Figure 4-10. Comparison of the TiO_2 and Ag-TiO_2 in the light and dark. Percent conversions are shown as a function of time in minutes.

4.3.2.2 Kinetic Study

Due to previous observations regarding the kinetics in degradation with methyl paraoxon and the growing likelihood supporting a hypothesis of multiple mechanism reactions, the same approach was taken to calculate the rate order and initial rate constant of TiO_2 and Ag-TiO_2.

Sample	**Light**			**Dark**		
	% Conversion	**Rate Order**	**Initial Rate Constant**	**% Conversion**	**Rate Order**	**Initial Rate Constant**
TiO_2	12.5	1st or 2nd	0.0007	11.9	1stor2nd	0.0006
Ag-TiO_2	23.8	1st	0.0016	34.9	2nd	0.0039

Table 4-1. Table comparing percent conversion, rate order and, initial rate constant of methyl paraoxon degradation reactions in the light and dark with TiO_2 and Ag-TiO_2.

TiO_2 showed minimal fluctuation in conversion when comparing the light and the dark. Upon analysis of the rate order and initial rate constant, there was minimal difference and it did not favor one over the other. When Ag-TiO_2 was kept in the dark there was a clear indication it of a first-order degradation compared to the second-order fit with an initial rate constant double the standard TiO_2 in the dark. **Figure 4-11** shows the rate plot of first-order degradation with Ag-TiO_2 in the light. The trend of data points is a poor linear fit and seems more logarithmic.

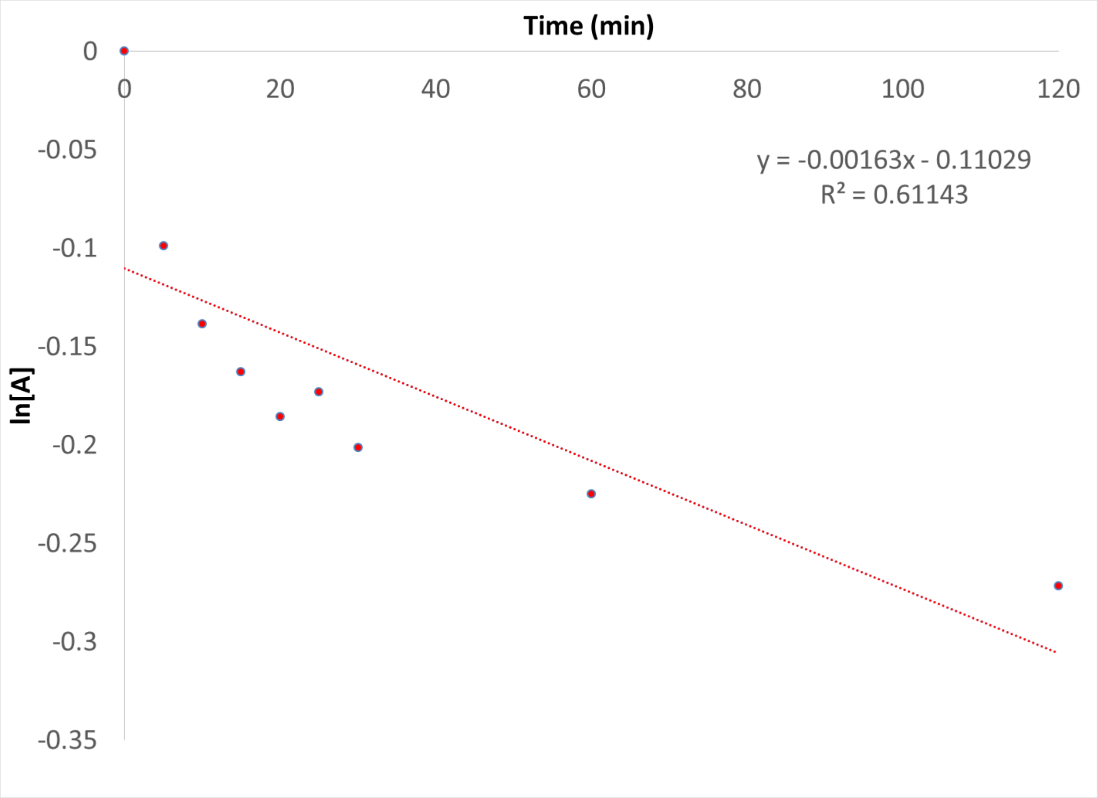

Figure 4-11. First-order rate plot for the degradation of methyl paraoxon with Ag-TiO_2 with UV Irradiation

In analysis of Ag-TiO_2 in the dark there is an almost perfect linear fit for a second-order degradation, **Figure 4-12**. The Ag-TiO_2 reaction in the dark has the fastest initial rate and produced the highest conversions and fastest kinetics of the four degradation experiments. The comparison can be seen in **Table 4-1.**

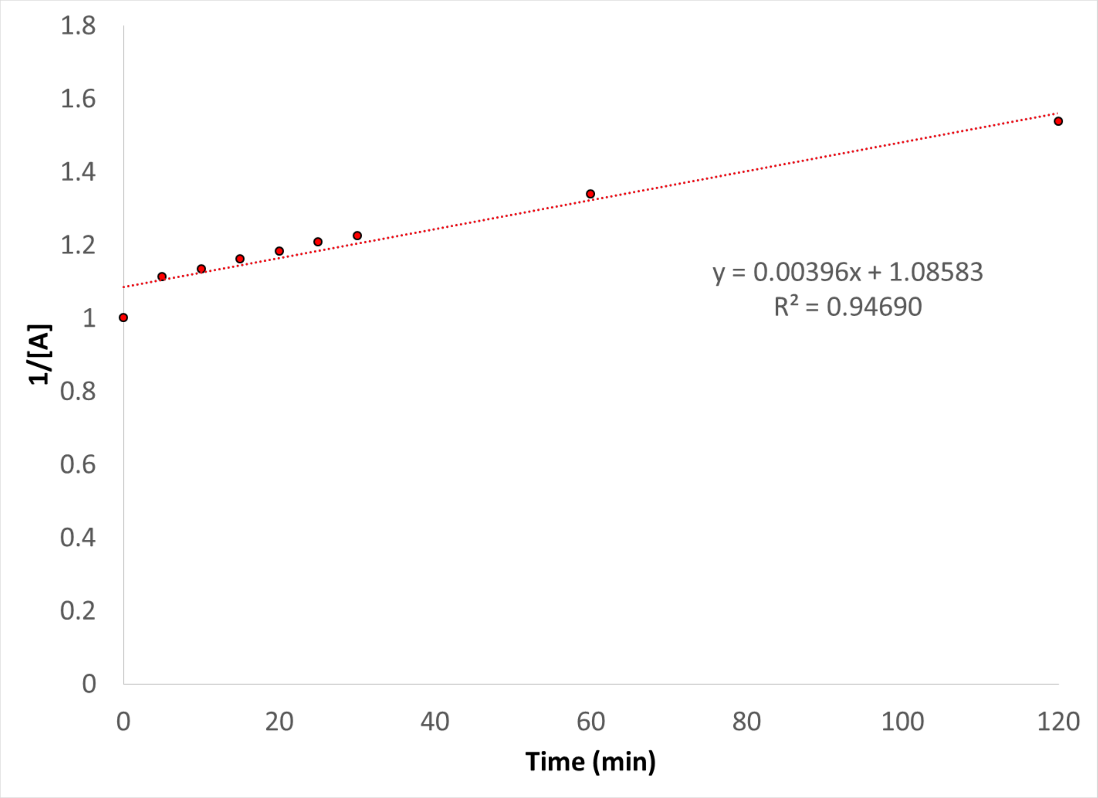

Figure 4-12. 2nd order rate plot for the degradation of methyl paraoxon with Ag-TiO_2 in the dark

There continues to be a high level of kinetic complexity within the first 5 min of the reaction that could potentially be result of heterogeneous binding, or in the case of metal deposited TiO_2, a slow charge transfer into the semiconductor. The observations are encouraging due to the enhancement seen in the degradation of methyl paraoxon when Ag is deposited on TiO_2. The complexity of the kinetics in the overall degradation reaction with methyl paraoxon requires further analysis. Degradations should also be repeated with a different simulant such as DMMP where ^{31}P NMR can be used to analyze the degradation and allow the conclusion to be drawn about multiple mechanisms, resulting in different degradation product formation.

4.4 Conclusions

TiO_2 nanofibers were fabricated using a sol-gel precursors, PMMA and TTiP, followed by electrospinning and a thermal treatment. Ag nanoparticles were deposited on the surface of the TiO_2 fiber through a polyol synthesis with silver nitrate. Metal deposited fibers were characterized by XRD, SEM, TEM and EDX demonstrating the presence of 153 nm Ag nanoparticles on the surface of the fiber.

Solid state UV-Vis and emission fluorescence spectroscopy were used to determine the potential band gap variation upon addition of Ag to the nanofibers. Results of the UV Vis showed a red shift in maximum absorbance by the wavelength increasing and energy increasing, leading to the conclusion that the band gap energy decreased. The anticipated results are that the emission lifetime of Ag-TiO_2 will have a smaller intensity then that of TiO_2; this in turn would mean the recombination rate of electron hole pair in Ag-TiO_2 is slower than that of TiO_2.

Results of the methyl paraoxon degradation with TiO_2 and Ag-TiO_2 showed that the metal deposited TiO_2 had an enhancement in the conversion to the nitrophenoxide product. However, the rate order was inconsistent between the samples allowing for no definitive conclusion of the rate of reaction. The complexity of the overall kinetics in the degradation of methyl paraoxon continues to complicate determinations of the favored degradation mechanism. The theory of competing mechanisms is still relevant and analysis is ongoing into assessing this hypothesis. This is further discussed in the subsequent Chapter, along with the introduction of a J-aggregate dye to promote the charge transfer into the semiconductor to aid in the degradation of methyl paraoxon.

4.5 References

1. Hsu, C. W.; DeLacy, B. G.; Johnson, S. G.; Joannopoulos, J. D.; Soljačić, M., Theoretical Criteria for Scattering Dark States in Nanostructured Particles. *Nano Letters* **2014,** *14* (5), 2783-2788.

2. Christopher, P.; Ingram, D. B.; Linic, S., Enhancing Photochemical Activity of Semiconductor Nanoparticles with Optically Active Ag Nanostructures: Photochemistry Mediated by Ag Surface Plasmons. *The Journal of Physical Chemistry C* **2010,** *114* (19), 9173-9177.

3. Würthner, F.; Kaiser, T. E.; Saha-Möller, C. R., J-Aggregates: From Serendipitous Discovery to Supramolecular Engineering of Functional Dye Materials. *Angewandte Chemie International Edition* **2011,** *50* (15), 3376-3410.

4. Luk'yanchuk, B.; Zheludev, N. I.; Maier, S. A.; Halas, N. J.; Nordlander, P.; Giessen, H.; Chong, C. T., The Fano resonance in plasmonic nanostructures and metamaterials. *Nat Mater* **2010,** *9* (9), 707-715.

5. DeLacy, B. G.; Miller, O. D.; Hsu, C. W.; Zander, Z.; Lacey, S.; Yagloski, R.; Fountain, A. W.; Valdes, E.; Anquillare, E.; Soljačić, M.; Johnson, S. G.; Joannopoulos, J. D., Coherent Plasmon-Exciton Coupling in Silver Platelet-J-aggregate Nanocomposites. *Nano Letters* **2015,** *15* (4), 2588-2593.

6. Ayala-Orozco, C.; Liu, J. G.; Knight, M. W.; Wang, Y.; Day, J. K.; Nordlander, P.; Halas, N. J., Fluorescence Enhancement of Molecules Inside a Gold Nanomatryoshka. *Nano Letters* **2014,** *14* (5), 2926-2933.

7. Schneider, J.; Matsuoka, M.; Takeuchi, M.; Zhang, J.; Horiuchi, Y.; Anpo, M.; Bahnemann, D. W., Understanding TiO2 Photocatalysis: Mechanisms and Materials. *Chemical Reviews* **2014,** *114* (19), 9919-9986.

8. Kato, H.; Kudo, A., Visible-Light-Response and Photocatalytic Activities of TiO2 and SrTiO3 Photocatalysts Codoped with Antimony and Chromium. *The Journal of Physical Chemistry B* **2002,** *106* (19), 5029-5034.

9. Primo, A.; Corma, A.; Garcia, H., Titania supported gold nanoparticles as photocatalyst. *Physical Chemistry Chemical Physics* **2011,** *13* (3), 886-910.

10. Obuya, E. A.; Joshi, P. C.; Gray, T. A.; Keane, T. C.; Jones, W. E., Jr., Application of Pt.TiO2 nanofibers in photosensitized degradation of rhodamine B. *International Journal of Chemistry* **2014,** *6* (1), 1-16.

11. Xu, A.-W.; Gao, Y.; Liu, H.-Q., The Preparation, Characterization, and their Photocatalytic Activities of Rare-Earth-Doped TiO2 Nanoparticles. *Journal of Catalysis* **2002,** *207* (2), 151-157.

12. Park, H.; Park, Y.; Kim, W.; Choi, W., Surface modification of TiO2 photocatalyst for environmental applications. *Journal of Photochemistry and Photobiology C: Photochemistry Reviews* **2013,** *15*, 1-20.

13. Mahshid, S.; Askari, M.; Ghamsari, M. S., Synthesis of TiO2 nanoparticles by hydrolysis and peptization of titanium isopropoxide solution. *Journal of Materials Processing Technology* **2007,** *189* (1–3), 296-300.

14. Liu, J.; McCarthy, D. L.; Cowan, M. J.; Obuya, E. A.; DeCoste, J. B.; Skorenko, K. H.; Tong, L.; Boyer, S. M.; Bernier, W. E.; Jones Jr, W. E., Photocatalytic activity of

TiO2 polycrystalline sub-micron fibers with variable rutile fraction. *Applied Catalysis B: Environmental* **2016,** *187*, 154-162.

15. Agasti, N.; Kaushik, N. K., One Pot Synthesis of Crystalline Silver Nanoparticles. *American Journal of Nanomaterials* **2014,** *2* (1), 4-7.

16. Su, C.; Liu, L.; Zhang, M.; Zhang, Y.; Shao, C., Fabrication of Ag/TiO2 nanoheterostructures with visible light photocatalytic function via a solvothermal approach. *CrystEngComm* **2012,** *14* (11), 3989-3999.

17. Santhosh, S. M.; Kandasamy, N., Antibiofilm Activity of Epoxy?Ag-TiO2 Polymer Nanocmposite Coating against Staphylococcus Aureus adn Escherichia Coli. *Coatings* **2015,** *5* (2), 95-114.

18. Yu, J.-G.; Yu, H.-G.; Cheng, B.; Zhao, X.-J.; Yu, J. C.; Ho, W.-K., The Effect of Calcination Temperature on the Surface Microstructure and Photocatalytic Activity of TiO2 Thin Films Prepared by Liquid Phase Deposition. *The Journal of Physical Chemistry B* **2003,** *107* (50), 13871-13879.

19. Choi, S. K.; Kim, S.; Lim, S. K.; Park, H., Photocatalytic Comparison of TiO2 Nanoparticles and Electrospun TiO2 Nanofibers: Effects of Mesoporosity and Interparticle Charge Transfer. *The Journal of Physical Chemistry C* **2010,** *114* (39), 16475-16480.

Chapter 5: Summary and Future Work

TiO_2-MOF/ polymer composites and, SPR deposited catalysts were investigated to enhance catalysis and the degradation of organic toxins. The toxic pollutants used were simulated chemical warfare agents and it was seen that the extent of enhancement of degradation was selective to the type of agent (blistering or nerve) being scrutinized. We have shown considerable advancements in developing an adequate methodology for the degradation of SCWAs as well as fabricating a suitable catalyst by electrospinning to assist in successful mitigation.

In Chapter 2 we showed the successful fabrication of TiO_2 nanofibers from a sol-gel solution followed by electrospinning and finishing with a thermal treatment in atmospheric conditions. Chapter 2 also shows that a nucleophilic solvent is necessary in the hydrolysis of CEES and that upon water saturation of TiO_2 the rate of degradation is increased compared to dry catalyst. The degradation of DMMP was also examined against both nanofibers and nanoparticles with similar surface areas. Results indicated that the nanofibers were more efficient in the degradation of DMMP over P25 nanoparticles, proving that the surface area of the catalyst does not play a pivotal role in efficiency of degradation.

Current challenges in examining the degradation of CEES using NMR are the fast rates of hydrolysis. The existing NMR procedure consumes valuable time from aliquot extraction to data analysis, in which hydrolysis continues to occur and therefore is not a suitable means to determine the kinetics of the reaction. To better understand the hydrolysis and rate of the CEES degradation with TiO_2, the use of MAS-NMR coupled with a UV irradiation source probe is necessary where the catalyst is in direct contact with the simulant and *in situ* measurements can be taken over the course of the experiment. *In situ* measurements will also allow for more accurate kinetic data to be acquired. Experiments using solid-state NMR should also be conducted for DMMP to better analyze the efficiency and rate of degradation. Catalysts possessing controlled varying surface areas should be used to gain a better understanding of the role surface area plays in the degradation of simulated chemical warfare agents. Varying the rutile and anatase proportions of TiO_2 should be examined to determine the influence of the crystal phase. The size of the grains that compose the nanofibers should be studied due to the potential impact on efficiency and rate of degradation

In Chapter 3, we showed the successful fabrication of polymer composite nanofibers containing 5 wt% UiO-66 and UiO-66 NH_2. The composites were characterized by several analytical techniques and it was concluded that the structural integrity of the MOF was maintained throughout the electrospinning process. Polymer composite nanofibers were introduced to methyl paraoxon in order to assess the degradation of this simulant. It was concluded that the presence of the TTiP and UiO-66 increased percent conversion and lowered the half-life of the reaction. The results acquired are the best to date according to literature with UiO-66. Degradation experiments in the presence of UV light led to the hypothesis of a slowly occurring base catalyzed reaction, as well as creating photo-induced electron-hole pairs which produced reactive radicals species, degrading the methyl paraoxon to a product lacking absorbance in the UV-Visible region of the electromagnetic spectrum.

Polymer composite fibers containing UiO-66 NH_2 underwent parallel degradation experiments. Results led to the conclusion that the addition of the amine functional group did not enhance the base catalyzed reaction of methyl paraoxon. The hypothesis of multiple mechanisms can again be applied to the degradation containing UiO-66 NH_2. Following completion of degradation experiments the kinetics were analyzed via first- and second-order rate laws. It was determined the kinetics are complicated and there is a potential heterogeneous binding event which occurred early in the reaction adding consider complexity to the kinetics.

In order to gain a better understanding into the role the MOF and polymer composite play in the degradation of simulated chemical warfare agents. Several options should be explored including varying the weight percent on the MOF in the polymer composite fibers. This would in turn help determine the critical amount of MOF necessary to efficiently enhance the degradation. This thesis focused on the use of Zr-based MOFs due to their exceptional water and thermal stability. However, it would be useful to analyze newly developed MOFs taking advantage of recent research. NU1000 has displayed extraordinary half-lives and percent conversions in the degradation of methyl paraoxon, **Figure 5-1**.

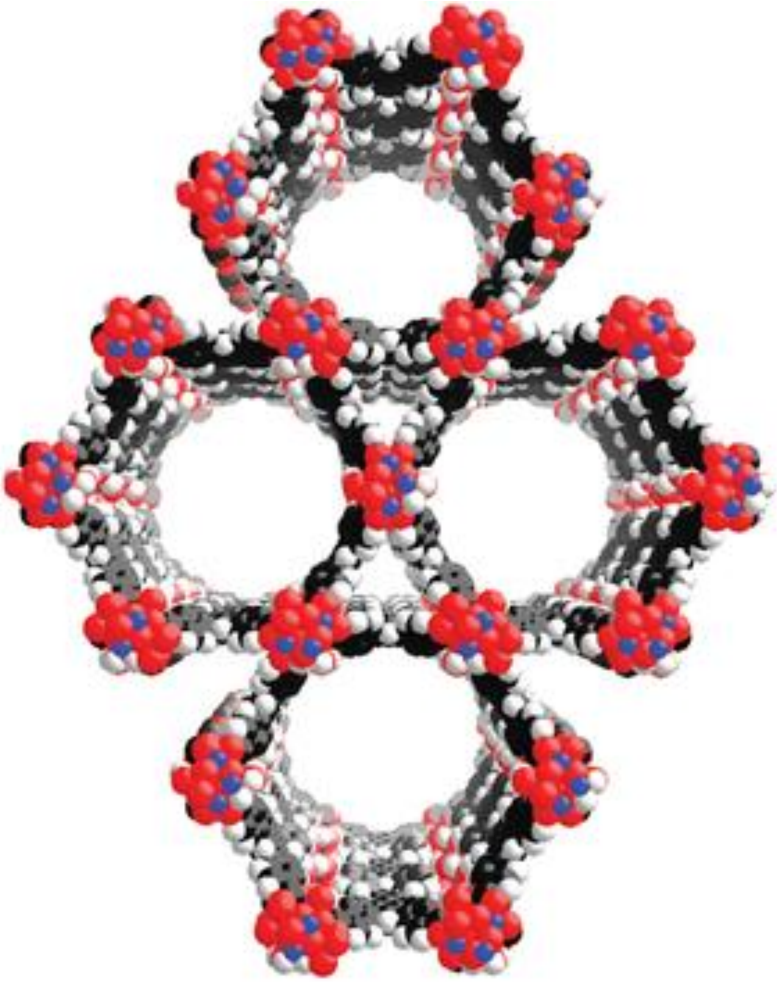

Figure 5-1. Structure of NU 1000, Courtesy of Northwestern University.

Other MOFs including Ti based MOFs could be used to exploit their photocatalytic properties and further promote visible photo-induced catalysis. Further investigation should be undertaken into the kinetics of the reactions. Reaction products can easily be determined by NMR or GCMS. Results would help prove the theory of photo-induced radical reaction occurring when the catalyst is exposed to irradiation. Base catalyzed reactions of methyl paraoxon were deemed successful, but to increase in the efficiency and rate the addition of a base to the composite polymer fiber mat via electrospinning should be explored. This is turn would aid in the transition from degradations being carried out in a pH 10 buffer to a more neutral medium. It also is extremely important that these materials be tested against actual agents. It is known that the simulant is as close to a chemical analog as can be reasonably explored in a conventional academic laboratory, however the agent itself may react differently when exposed to ultimate target materials. For these materials to be used in battlefield technology it is imperative that they have successful results demonstrated against actual CWAs.

In Chapter 4, the successful fabrication of Ag-TiO_2 nanofibers via a polyol synthesis with silver nitrate was reported. Fibers were characterized and it was concluded that the deposition of silver was successful. UV-Visible and fluorescence spectroscopy led to the determination the band gap of the TiO_2 had decreased upon addition of silver. Degradation with methyl paraoxon showed the addition of silver to the TiO_2 was successful in increasing the percent conversion of methyl paraoxon to nitrophenoxide. Yet again, the competing degradation mechanisms reoccurred as well as the awareness of the complexity into the kinetics of the overall reaction.

It is hypothesized that charge transfer will further enhance photocatalysis in plexicitonic materials. To further develop the research in visible-light photocatalysis, plexicitonic materials can theoretically be excited by visible irradiation to enhance the charge transfer process to the semiconductor, which in turn will improve the rate of catalysis. Appropriate new materials and particle structures should be fabricated for use in photocatalytic reactions. The shape and size of silver particles should be explored to determine to affect the metal SPR will play in the charge transfer process. The post synthesized silver should be deposited to the surface with different deposition procedures as well as varying amounts of SPR to ensure the maximum efficiency of charge transfer. It is propose that silver-deposited fibers should then be electrostatically coated with a J-aggregate dye to create the desired photogenerated Fano resonance that has been deemed necessary for charge transfer. Plexcitonic nanocomposites should be thoroughly characterized prior to photocatalytic degradations, including XPS to confirm energy of the Fermi levels in the nanoparticles relative to TiO_2. Plexcitonic materials could promote visible-induced photocatalysis by subsequently enhancing the number of electrons that are injected into the titania semiconductor.